JETP Letters, Vol. 73, No. 11, 2001, pp. 579–583. From Pis'ma v Zhurnal Éksperimental'noĭ i Teoreticheskoĭ Fiziki, Vol. 73, No. 11, 2001, pp. 659–663.

QED Corrections in Deep-Inelastic Scattering from Tensor-Polarized Deuteron Target[1]

G. I. Gakh and N. P. Merenkov

National Science Center Kharkov Institute of Physics and Technology, Kharkov, 61108 Ukraine

Received April 18, 2001

The leading-log model-independent radiative corrections to deep-inelastic scattering of an unpolarized electron beam from the tensor-polarized deuteron target have been considered. The calculation is based on the covariant parameterization of the deuteron quadrupole polarization tensor and the use of the Drell–Yan-like representation in electrodynamics to describe the radiation of real and virtual particles by the initial and scattered electron.

PACS numbers: 12.20.Ds; 13.40.-f; 13.60.Hb; 13.88.+e; 25.30.Dh

1. Processes with polarized particles are a rich source of new information on the structure of the nucleon and its fragmentation. Polarized deuterons and nuclei of ^{3}He are used to extract information on the neutron spin-dependent structure function $g_1(x)$ [1]. However, the polarized deuteron is interesting in its own right, because it has spin 1. Therefore, due to the deuteron electric-quadrupole structure, other spin-dependent structure functions (as compared with spin 1/2 particles) appear [2]. The 15-GeV ELFE project provides a good opportunity for the measurement of some hadron tensor structure functions, which could give clues to physics of nonnucleonic components in spin-one nuclei and to study the tensor structure on the quark–gluon level [3]. The use of the tensor polarized deuteron target at HERMES allows one to investigate the nuclear binding effects and nuclear gluon components [4].

Current experiments at modern accelerators reached a new level of precision, and this circumstance requires a new approach to data analysis and inclusion of all possible systematic uncertainties. One of the important sources of such uncertainties is the electromagnetic radiative effect caused by physical processes which take place in higher orders of perturbation theory with respect to the electromagnetic interaction. In this paper, we give the covariant description of the cross-section of the deep-inelastic scattering of unpolarized electron beam from the tensor-polarized deuteron target

$$e^-(k_1) + d_T(p_1) \longrightarrow e^-(k_2) + X(p_x), \qquad (1)$$

and we use it to calculate the QED radiative corrections (RC) by means of the electron structure function method [5].

The corresponding approach is based on the covariant parameterization of the deuteron quadrupole polarization tensor in terms of the 4-momenta of the particles in process (1) [6] and use of the Drell–Yan-like representation [7] in electrodynamics, which allows one to sum the leading-log model-independent RC in all orders. Some applications of this representation for the calculation of RC to the polarization-independent and polarization-dependent contributions to the cross section in different processes one can find in [8].

2. To begin with, we define the DIS cross section of process (1), taking into account RC, in terms of the leptonic $L_{\mu\nu}$ and hadronic $H_{\mu\nu}$ tensors contraction

$$\frac{d\sigma}{dQ^2dy} = \frac{\pi\alpha^2}{Vq^4}L_{\mu\nu}H_{\mu\nu}, \quad y = \frac{2p_1(k_1-k_2)}{V}, \qquad (2)$$
$$V = 2k_1p_1,$$

where q is the 4-momentum of the intermediate heavy photon that probes the deuteron structure. Note that only in the Born approximation (without taking into account RC) $q = k_1 - k_2$.

The model-independent RC exhibit themselves by means of the corrections to the leptonic tensor. In the framework of the leading accuracy, this tensor can be written as a convolution of two electron structure functions D and the Born form of the leptonic tensor $L^B_{\mu\nu}$ that depends on the scaled electron momenta

$$L_{\mu\nu}(k_1, k_2) = \iint\frac{dx_1dx_2}{x_1x_2^2}D(x_1, L)D(x_2, L)L^B_{\mu\nu}(\hat{k}_1, \hat{k}_2),$$

$$L = \ln\frac{Q^2}{m^2}, \qquad (3)$$

[1] This article was submitted by the authors in English.

0021-3640/01/7311-0579$21.00 © 2001 MAIK "Nauka/Interperiodica"

$$\hat{k}_1 = x_1 k_1, \quad \hat{k}_2 = \frac{k_2}{x_2},$$

$$\hat{k}_1 - \hat{k}_2 = q, \quad Q^2 = -(k_1 - k_2)^2,$$

where m is the electron mass.

The limits of integration on the right-hand side of Eq. (3) can be derived from the condition that DIS process (1) takes place. It is possible if the final undetected hadron system consists, at least, of a deuteron and a pion. In this case,

$$x_1 x_2 + y - 1 - x_1 xy \geq x_2 \delta, \quad x = \frac{Q^2}{2p_1(k_1 - k_2)}, \qquad \delta = \frac{(M + m_\pi)^2 - M^2}{V}, \tag{4}$$

where M (m_π) is the deuteron (pion) mass. This inequality defines the integration limits as follows:

$$1 \geq x_1 \geq \frac{1 + \delta - y}{1 - xy}, \quad 1 \geq x_2 \geq \frac{1 - y + x_1 xy}{x_1 - \delta}. \tag{5}$$

In fact, representation (3) for the leptonic tensor contains all mass collinear singularities arising due to the radiation of real and virtual photons and electron–positron pairs by the initial and scattered electrons. It reflects the essence of the quasi-real electron method [9] suitable to describe the real collinear particle emission by means of the contribution of the so-called Θ term to the electron structure function (for the details of the D function see, for example, [10]).

The Born leptonic tensor is

$$L^B_{\mu\nu}(k_1, k_2) = -2k_1 k_2 g_{\mu\nu} + 2(k_{1\mu} k_{2\nu} + k_{1\nu} k_{2\mu}). \tag{6}$$

To write the hadron tensor, we define first the tensor-polarized deuteron density matrix (here, we do not consider the effect caused by the vector polarization of the deuteron)

$$\rho_{\mu\nu} = -\frac{1}{3}\left(g_{\mu\nu} - \frac{p_{1\mu} p_{1\nu}}{M^2}\right) + Q_{\mu\nu}, \quad Q_{\mu\nu} = Q_{\nu\mu}, \qquad Q_{\mu\mu} = 0, \quad p_{1\mu} Q_{\mu\nu} = 0, \tag{7}$$

where $Q_{\mu\nu}$ is the deuteron quadrupole polarization tensor. The corresponding hadron tensor has polarization-independent and polarization-dependent parts

$$H_{\mu\nu} = H^{(u)}_{\mu\nu} + H^{(T)}_{\mu\nu}, \quad H^{(u)}_{\mu\nu} = -W_1 \tilde{g}_{\mu\nu} + \frac{W_2}{M^2} \tilde{p}_{1\mu} \tilde{p}_{1\nu},$$

$$\tilde{g}_{\mu\nu} = g_{\mu\nu} - \frac{q_\mu q_\nu}{q^2}, \quad \tilde{p}_{1\mu} = p_{1\mu} - \frac{p_1 q}{q^2} q_\mu,$$

$$H^{(T)}_{\mu\nu} = aB_1 \tilde{g}_{\mu\nu} + \frac{aB_2}{p_1 q} \tilde{p}_{1\mu} \tilde{p}_{1\nu} \tag{8}$$

$$+ \frac{M^2}{(p_1 q)^2} B_3 q_\alpha (\tilde{p}_{1\mu} Q_{\tilde{\nu}\alpha} + \tilde{p}_{1\nu} Q_{\tilde{\mu}\alpha}) + \frac{M^2}{p_1 q} B_4 \tilde{Q}_{\mu\nu},$$

$$a = \frac{M^2}{(p_1 q)^2} Q_{\alpha\beta} q_\alpha q_\beta.$$

In general, all the hadron structure functions W_i ($i = 1, 2$) and B_j ($j = 1, 2, 3, 4$) depend on two independent variables: q^2 and $x' = -q^2/2p_1 q$ [within the chosen accuracy $x' = \hat{x} = x_1 xy/(x_1 x_2 + y - 1)$]. We used the following notation on the right-hand side of Eq. (8):

$$Q_{\mu\tilde{\nu}} = Q_{\mu\nu} - \frac{q_\nu q_\alpha}{q^2} Q_{\mu\alpha}, \quad Q_{\mu\tilde{\nu}} q_\nu = 0,$$

$$\tilde{Q}_{\mu\nu} = Q_{\mu\nu} + \frac{q_\mu q_\nu}{q^4} Q_{\alpha\beta} q_\alpha q_\beta - \frac{q_\nu q_\alpha}{q^2} Q_{\mu\alpha} - \frac{q_\mu q_\alpha}{q^2} Q_{\nu\alpha}, \quad \tilde{Q}_{\mu\nu} q_\nu = 0. \tag{9}$$

Note also that the hadron structure functions B_j are related to the structure functions b_j, introduced in [2] (HJM), in the following way:

$$B_1 = -b_1, \quad B_2 = \frac{b_2}{3} + b_3 + b_4,$$

$$B_3 = \frac{b_2}{6} - \frac{b_4}{2}, \quad B_4 = \frac{b_2}{3} - b_3.$$

At the chosen normalization, the elastic limit ($p_x^2 = M^2$) can be reached by mere substitution in hadronic tensor

$$W_i(x', q^2) \longrightarrow -\frac{1}{q^2}\delta(1 - x') W_i^{(\mathrm{el})}, \qquad B_j(x', q^2) \longrightarrow -\frac{1}{q^2}\delta(1 - x') B_j^{(\mathrm{el})}, \tag{10}$$

where

$$W_1^{(\mathrm{el})} = -\frac{2}{3} q^2 \left(1 - \frac{\rho}{4}\right) G_2^2,$$

$$W_2^{(\mathrm{el})} = M^2 \left\{ 4\left[1 - \frac{\rho}{3}\left(1 - \frac{\rho}{4}\right)\right] G_1^2 + \rho^2 G_3^2 \right.$$

$$- \frac{2}{3}\rho\left(1 - \frac{\rho}{2}\right) G_2^2 + \frac{4}{3}\rho\left(1 + \frac{\rho}{2}\right) G_1 G_3 \tag{11}$$

$$\left. - \frac{4}{3}\rho\left(1 - \frac{\rho}{2}\right) G_1 G_2 + \frac{2}{3}\rho^2 G_2 G_3 \right\},$$

$$\rho = \frac{q^2}{M^2}, \quad G_i = G_i(q^2),$$

$$B_1^{(\mathrm{el})} = -\frac{\rho q^2}{4} G_2^2,$$

$$\begin{aligned} B_2^{(\mathrm{el})} &= -\frac{\rho^2 q^2}{8}[(2G_1 + G_2)^2 + 8G_1 G_3], \\ B_2^{(\mathrm{el})} &= -\frac{\rho^2 q^2}{8}(G_2^2 + 2G_1 G_2 + 4G_2 G_3), \end{aligned} \tag{12}$$

$$B_4^{(\mathrm{el})} = \frac{\rho q^2}{2}\left(1 - \frac{\rho}{4}\right) G_2^2.$$

The elastic deuteron electromagnetic form factors G_E (electric), G_M (magnetic), and G_Q (quadrupole) can be expressed in terms of the form factors $G_i (i = 1, 2, 3)$ [11] by means of the following relations:

$$G_E = G_1 + \frac{\rho}{2} G_3, \quad G_M = G_2,$$

$$G_Q = G_1 + 2G_2 + \left(2 - \frac{\rho}{4}\right) G_3.$$

3. Because the polarization-independent part of the hadronic tensor depends on the scaled electron momenta only (by means of $q = \hat{k}_1 - \hat{k}_2$), we can write the respective contribution to the cross section in the form of the Drell–Yan representation in the electrodynamics that takes into account the leading part of RC

$$\begin{aligned} &\frac{d\sigma^{(u)}(k_1, k_2)}{dQ^2 dy} \\ &= \iint \frac{dx_1 dx_2}{x_2^2} D(x_1, L) D(x_2, L) \frac{d\sigma_B^{(u)}(\hat{k}_1, \hat{k}_2)}{d\hat{Q}^2 d\hat{y}}, \end{aligned} \tag{13}$$

where $\hat{Q}^2 = x_1 Q^2/x_2$, $\hat{y} = (x_1 x_2 + y - 1)/x_1 x_2$, and the unpolarized Born cross section reads

$$\begin{aligned} &\frac{d\sigma_B^{(u)}(k_1, k_2)}{dQ^2 dy} \\ &= \frac{2\pi\alpha^2}{VQ^2}\left[W_1(x, Q^2) + \frac{1 - y - xy\tau}{2xy\tau} W_2(x, Q^2)\right], \end{aligned} \tag{14}$$

$$\tau = \frac{M^2}{V}.$$

As to the polarization-dependent contribution to the cross section $d\sigma^{(T)}$, the situation is somewhat different. In general, we cannot use for it representation (13) with mere substitution

$$\frac{d\sigma^{(u)}}{dQ^2 dy} \longrightarrow \frac{d\sigma^{(T)}}{dQ^2 dy} \tag{15}$$

on both sides of Eq. (13). The reason is that the axes with respect to which the components of the deuteron quadrupole polarization tensor $Q_{\alpha\beta}$ are defined can change their directions with the scale transformation of electron momenta: $k_{1,2} \longrightarrow \hat{k}_{1,2}$. For example, this occurs obviously when one of the axes is directed along the $(\mathbf{k}_1 - \mathbf{k}_2)$ direction. But substitution of Eq. (15) can be useful and applicable if all axes remain stabilized under this transformation.

Therefore, we first have to find the set of stabilized axes and write them in covariant form in terms of 4-momenta of the particles participating in the reaction. If we choose the longitudinal direction $\mathbf{l}$ along the electron beam and the transverse one $\mathbf{t}$ in the plane $(\mathbf{k}_1, \mathbf{k}_2)$ and perpendicular to $\mathbf{l}$, then

$$\begin{aligned} S_\mu^{(l)} &= \frac{2\tau k_{1\mu} - p_{1\mu}}{M}, \\ S_\mu^{(t)} &= \frac{k_{2\mu} - (1 - y - 2xy\tau)k_{1\mu} - xy p_{1\mu}}{d}, \\ S_\mu^{(n)} &= \frac{2\varepsilon_{\mu\lambda\rho\sigma} p_{1\lambda} k_{1\rho} k_{2\sigma}}{Vd}, \\ d &= \sqrt{Vxyb}, \quad b = 1 - y - xy\tau. \end{aligned} \tag{16}$$

One can verify that the set $S_\mu^{(l,t,n)}$ remains stabilized under the scale transformation and

$$S_\mu^{(\alpha)} S_\mu^{(\beta)} = -\delta_{\alpha\beta}, \quad S_\mu^{(\alpha)} p_{1\mu} = 0, \quad \alpha, \beta = l, t, n.$$

One can also make sure that in the rest frame of the deuteron

$$\begin{aligned} S_\mu^{(l)} &= (0, \mathbf{l}), \quad S_\mu^{(t)} = (0, \mathbf{t}), \quad S_\mu^{(n)} = (0, \mathbf{n}), \\ \mathbf{l} &= \mathbf{n}_1, \quad \mathbf{t} = \frac{\mathbf{n}_2 - (\mathbf{n}_1 \mathbf{n}_2)\mathbf{n}_1}{\sqrt{1 - (\mathbf{n}_1 \mathbf{n}_2)^2}}, \\ \mathbf{n} &= \frac{\mathbf{n}_1 \times \mathbf{n}_2}{\sqrt{1 - (\mathbf{n}_1 \mathbf{n}_2)^2}}, \quad \mathbf{n}_{1,2} = \frac{\mathbf{k}_{1,2}}{|\mathbf{k}_{1,2}|}. \end{aligned} \tag{17}$$

If we add one more 4-vector $S_\mu^{(0)} = p_{1\mu}/M$ to the set of Eqs. (16), we obtain the complete set of orthogonal 4-vectors with the following properties:

$$\begin{aligned} S_\mu^{(m)} S_\nu^{(m)} &= g_{\mu\nu}, \quad S_\mu^{(m)} S_\mu^{(n)} = g_{mn}, \\ m, n &= 0, l, t, n. \end{aligned} \tag{18}$$

This allows one to express the deuteron quadrupole polarization tensor in general case as

$$Q_{\mu\nu} = S_\mu^{(m)} S_\nu^{(n)} R_{mn} \equiv S_\mu^{(\alpha)} S_\nu^{(\beta)} R_{\alpha\beta}, \quad R_{\alpha\beta} = R_{\beta\alpha}, \quad R_{\alpha\alpha} = 0 \tag{19}$$

because the components R_{00}, $R_{0\alpha}$, and $R_{\alpha 0}$ are identically equal to zero due to the condition $Q_{\mu\nu} p_{1\nu} = 0$.

Within the leading accuracy, when the radiation of noncollinear particles by the initial and the scattered electrons is not considered, the components R_{nl} and R_{nt} do not contribute and expansion (19) can be recast in the following standard form:

$$Q_{\mu\nu} = \left[S_\mu^{(l)} S_\nu^{(l)} - \frac{1}{2} S_\mu^{(t)} S_\nu^{(t)} \right] R_{ll} + \frac{1}{2} S_\mu^{(t)} S_\nu^{(t)} (R_{tt} - R_{nn}) + (S_\mu^{(l)} S_\nu^{(t)} + S_\mu^{(t)} S_\nu^{(l)}) R_{lt}, \tag{20}$$

where we took into account that $R_{ll} + R_{tt} + R_{nn} = 0$.

So, if the components of the deuteron polarization tensor are defined in the coordinate system with the axes along the directions **l**, **t**, and **n**, as given by Eqs. (17), the polarization-dependent contribution to the cross section of the process (1), taking into account the leading RC, can be written in the same way as the polarization-independent one

$$\frac{d\sigma^{(T_s)}(k_1, k_2)}{dQ^2 dy} = \iint \frac{dx_1 dx_2}{x_2^2} D(x_1, L) D(x_2, L) \frac{d\sigma_B^{(T_s)}(\hat{k}_1, \hat{k}_2)}{d\hat{Q}^2 d\hat{y}}. \tag{21}$$

Symbol T_s indicates that the components of the quadrupole polarization are defined with respect to the stabilized set of Eqs. (16). The simple calculation, using Eqs. (16) and (20) and the definition of the Born leptonic (6) and hadronic (8) tensors, gives

$$\frac{d\sigma_B^{(T_s)}(k_1, k_2)}{dQ^2 dy} = \frac{2\pi\alpha^2}{yQ^4} [S_{ll} R_{ll} + S_{tt}(R_{tt} - R_{nn}) + S_{lt} R_{lt}], \tag{22}$$

where

$$S_{ll} = [2xb\tau - y(1 + 2x\tau)^2] G + 2b(1 + 3x\tau) B_3 + (b - xy\tau) B_4, \tag{23}$$

$$S_{lt} = 2\sqrt{\frac{xb\tau}{y}} [2y(1 + 2x\tau) G + (2 - y - 4b) B_3 + y B_4], \tag{24}$$

$$S_{tt} = 2xb\tau(-G - B_3), \quad G = xyB_1 - \frac{b}{y} B_2. \tag{25}$$

4. Consider now the case when the components of the deuteron polarization tensor are defined in the coordinate system with the axes along directions **L**, **T**, and **N** in the rest frame of the deuteron, where

$$\mathbf{L} = \frac{\mathbf{k}_1 - \mathbf{k}_2}{|\mathbf{k}_1 - \mathbf{k}_2|}, \quad \mathbf{T} = \frac{\mathbf{n}_1 - (\mathbf{n}_1 \mathbf{L})\mathbf{L}}{\sqrt{1 - (\mathbf{n}_1 \mathbf{L})^2}}, \quad \mathbf{N} = \mathbf{n}. \tag{26}$$

As one can see, directions **L** and **T** became unstable under the scale transformation. The respective covariant form of the set of Eqs. (26) reads

$$S_\mu^{(L)} = \frac{2\tau(k_1 - k_2)_\mu - y p_{1\mu}}{M\sqrt{yh}}, \quad S_\mu^{(t)} = \frac{(1 + 2x\tau) k_{2\mu} - (1 - y - 2x\tau) k_{1\mu} - x(2 - y) p_{1\mu}}{\sqrt{Vxbh}}, \quad S_\mu^{(N)} = S_\mu^{(n)}, \quad h = y + 4x\tau, \tag{27}$$

and the expansion of the deuteron polarization tensor is defined in full analogy with Eq. (20)

$$Q_{\mu\nu} = \left[S_\mu^{(L)} S_\nu^{(L)} - \frac{1}{2} S_\mu^{(T)} S_\nu^{(T)} \right] R_{LL} + \frac{1}{2} S_\mu^{(T)} S_\nu^{(T)} (R_{TT} - R_{NN}) + (S_\mu^{(L)} S_\nu^{(T)} + S_\mu^{(T)} S_\nu^{(L)}) R_{LT}. \tag{28}$$

To use the Drell–Yan-like representation in this case, we have to express the unstable 4-vectors $S_\mu^{(A)}$ ($A = L, T$) through the stabilized 4-vectors $S_\mu^{(\alpha)}$ ($\alpha = l, t$). These sets are connected by means of an orthogonal matrix which describes the rotation in the plane perpendicular to direction $\mathbf{n} = \mathbf{N}$:

$$S_\mu^{(L)} = \cos\theta S_\mu^{(l)} + \sin\theta S_\mu^{(t)}, \quad S_\mu^{(T)} = -\sin\theta S_\mu^{(l)} + \cos\theta S_\mu^{(t)}, \quad \cos\theta = \frac{y(1 + 2x\tau)}{\sqrt{yh}}, \quad \sin\theta = -2\sqrt{\frac{xb\tau}{h}}. \tag{29}$$

We now must substitute Eqs. (29) into expansion (28) and perform the contraction of the leptonic and hadronic tensors. This procedure leads to the following formula for the polarization-dependent part of the cross section in the considered case of unstable axes:

$$\frac{d\sigma^{(T_u)}(k_1, k_2)}{dQ^2 dy} = X_{ij} \iint \frac{dx_1 dx_2}{x_2^2} D(x_1, L) D(x_2, L) \frac{d\sigma^{(ij)}(\hat{k}_1, \hat{k}_2)}{d\hat{Q}^2 d\hat{y}}, \tag{30}$$

where we bear in mind the summation over i and j ($i, j = l, t$). Symbol T_u indicates that the components of the deuteron polarization tensor are defined with respect to unstable axes (27).

The principal point of representation (30) resides in that matrix X_{ij} depends on nonscaled electron momenta through the angle θ defined in Eq. (29). Its elements read

$$X_{ll} = \frac{1}{4}(1 + 3\cos 2\theta)R_{LL} + \frac{1}{4}(1 - \cos 2\theta)(R_{TT} - R_{NN}) - \sin 2\theta R_{LT},$$

$$X_{lt} = \frac{1}{4}\sin 2\theta[3R_{LL} - (R_{TT} - R_{NN})] + \cos 2\theta R_{LT}, \quad (31)$$

$$X_{tt} = \frac{3}{4}(1 - \cos 2\theta)R_{LL} + \frac{1}{4}(3 + \cos 2\theta)(R_{TT} - R_{NN}) + \sin 2\theta R_{LT},$$

where

$$\cos 2\theta = \frac{y + 4x\tau(-1 + 2y + 2xy\tau)}{h},$$

$$\sin 2\theta = -\frac{4(1 + 2x\tau)}{h}\sqrt{xyb\tau}.$$

The partial cross sections under the integral sign on the right-hand side of Eq. (30) depend just on the scaled electron momenta. These are

$$\frac{d\sigma^{(ij)}(k_1, k_2)}{dQ^2 dy} = \frac{2\pi\alpha^2}{yQ^4}S_{ij}, \quad (32)$$

where elements of S_{ij} are defined by Eqs. (23)–(25).

To derive the cross section on the left-hand side of Eq. (30) in the Born approximation, one can use the ordinary δ functions instead of D functions on the right-hand side of this equation. This leads to the result very similar to Eq. (22)

$$\frac{d\sigma_B^{(T_u)}}{dQ^2 dy} = X_{ij}\frac{d\sigma^{(ij)}}{dQ^2 dy} = \frac{2\pi\alpha^2}{yQ^4}[S_{LL}R_{LL} + S_{TT}(R_{TT} - R_{NN}) + S_{LT}R_{LT}], \quad (33)$$

$$S_{LL} = -hG + 2bB_3 + \frac{B_4}{h}[(1 - y)(y - 2x\tau) - 2xy\tau(y + x\tau)],$$

$$S_{TT} = \frac{2xb\tau}{h}B_4, \quad S_{LT} = 2\sqrt{\frac{xb\tau}{y}}(2 - y)\left(B_3 + \frac{y}{h}B_4\right). \quad (34)$$

Note that relations (34) can be checked independently by the straightforward calculation using the expansion of the deuteron polarization tensor as given by Eq. (28) and covariant expressions $S_\mu^{(L)}$ and $S_\mu^{(T)}$ for the axes defined by Eq. (27).

We thank the Ukrainian DFFD for the support.

REFERENCES

1. D. Adams, B. Adeva, E. Arik, *et al.*, Phys. Lett. B **357**, 248 (1995); P. L. Anthony, R. G. Arnold, H. R. Band, *et al.*, Phys. Rev. D **54**, 6620 (1996).
2. P. Hoodbhoy, R. L. Jaffe, and A. Manohar, Nucl. Phys. B **312**, 571 (1989); R. L. Jaffe and A. Manohar, Nucl. Phys. B **321**, 343 (1989); P. Hoodbhoy, R. L. Jaffe, and E. Sather, Phys. Rev. D **43**, 3071 (1991).
3. R. G. Milner, in *Electronuclear Physics with Internal Targets*, Ed. by R. G. Arnold (World Scientific, Singapore, 1989).
4. C. Amsler, T. Bressani, F. E. Close, *et al.*, Nucl. Phys. A **622**, 315c (1997).
5. V. N. Gribov and L. N. Lipatov, Yad. Fiz. **15**, 808 (1972) [Sov. J. Nucl. Phys. **15**, 451 (1972)]; Yad. Fiz. **15**, 1218 (1972) [Sov. J. Nucl. Phys. **15**, 675 (1972)]; L. N. Lipatov, Yad. Fiz. **20**, 94 (1974) [Sov. J. Nucl. Phys. **20**, 48 (1974)]; G. Altarelli and G. Parisi, Nucl. Phys. B **126**, 298 (1977).
6. I. V. Akushevich and N. M. Shumeiko, J. Phys. G **20**, 513 (1994); A. V. Afanas'ev, I. V. Akushevich, and N. P. Merenkov, hep-ph/0102086.
7. S. D. Drell and T. M. Yan, Phys. Rev. Lett. **25**, 316 (1970).
8. E. A. Kuraev and V. S. Fadin, Yad. Fiz. **41**, 733 (1985) [Sov. J. Nucl. Phys. **41**, 466 (1985)]; E. A. Kuraev, N. P. Merenkov, and V. S. Fadin, Yad. Fiz. **47**, 1593 (1998) [Nucl. Phys. **47**, 1009 (1998)]; F. A. Berends, W. L. van Neervan, and G. J. H. Burgers, Nucl. Phys. B **297**, 429 (1988); A. V. Afanas'ev, I. V. Akushevich, and N. P. Merenkov, hep-ph/0009273.
9. V. N. Baier, V. S. Fadin, and V. A. Khoze, Nucl. Phys. B **65**, 381 (1973).
10. S. Jadach, M. Skrzypek, and B. F. L. Ward, Phys. Rev. D **47**, 3733 (1993); M. Skrzypek, Acta Phys. Pol. B **23**, 135 (1992).
11. A. I. Akhiezer and M. P. Rekalo, in *Electrodynamics of Hadrons* (Naukova Dumka, Kiev, 1977), p. 218.

JETP Letters, Vol. 73, No. 11, 2001, pp. 584–586. Translated from Pis'ma v Zhurnal Éksperimental'noĭ i Teoreticheskoĭ Fiziki, Vol. 73, No. 11, 2001, pp. 664–666.

A Mechanism of Unexpected Temperature Dependence of Muonic Catalysis in Solid Deuterium

S. S. Gershteĭn

Institute for High Energy Physics, Protvino, Moscow region, 142284 Russia

e-mail: gershtein@mx.ihep.su

Received May 4, 2001

It is shown that, at sufficiently low temperatures, the elastic scattering of $d\mu$ mesic atoms (as well as slow neutrons) in solid deuterium proceeds on the whole crystal lattice without energy loss, whereas inelastic scattering with excitation of phonons is weak. For this reason, the resonant formation of $dd\mu$ mesic molecules in solid deuterium occurs before the thermalization of $d\mu$ mesic atoms, which explains the observed temperature independence of the $dd\mu$-molecule formation rate and muonic catalysis. *© 2001 MAIK "Nauka/Interperiodica".*

PACS numbers: 36.10.Gv; 25.45.-z

Because a $dd\mu$ mesic molecule has a loosely bound vibrational–rotational level with the quantum numbers $\nu = 1$ and $K = 1$ [1–3], these molecules can be formed in gaseous and liquid deuterium through a very effective resonant mechanism [4] followed by the nuclear fusion reactions $dd \longrightarrow {}^3\mathrm{He} + n$ or $dd \longrightarrow T + p$. The point is that the binding energy $\epsilon \approx 2$ eV of the $dd\mu$ mesic molecule in this state is so low that only a little energy is required for exciting the $n = 7$ vibrational level of the $[d\mu d, d]2e$ molecular complex, which arises when one of the nuclei of a D_2 molecule is replaced by a $dd\mu$ mesic molecule. The storage of energy is filled by the thermal-motion energy of a $d\mu$ mesic atom, which is thermalized in a medium, via colliding with one of the constituent deuterons of the D_2 molecule; this process ensures the resonant-formation condition [4].

Because a $d\mu$ mesic atom has two hyperfine levels with the total spins $F = 3/2$ and 1/2 and energy difference $\Delta E = 0.0485$ eV, the resonant mechanism should be examined in more detail.

Analyzing the time dependence of the muonic catalysis at various temperatures, one can experimentally determine the mesic-molecule formation rate from various hyperfine states of a $d\mu$ mesic atom and the rate of the transition proceeding from the upper 3/2 state to the lower 1/2 state in exchange collisions of the $d\mu$ mesic atom with deuterons [5]. In agreement with the theoretical calculations [6, 7], the rate of the resonant $dd\mu$ formation from the lower hyperfine 1/2 state of the $d\mu$ mesic atom decreases with decreasing temperature of the gaseous or liquid medium because the thermal energy of thermalized $d\mu$ mesic atoms is insufficient to ensure the resonant condition. The resonant mechanism of the $dd\mu$ formation from the state $d\mu(F = 1/2)$ almost completely ceases to contribute at $T \approx 70$ K, and the $dd\mu$ formation from the 1/2 state proceeds through the nonresonant mechanism with the transfer of the mesic-molecule binding energy to an atomic electron [6–15] (see Fig. 1). The latter mechanism occurs with a probability that is almost two orders of magnitude lower than that of the resonant mechanism and leads to the mesic molecule formation predominantly in states with the even rotational numbers and even total nuclear spin [2]. In addition, this is experimentally corroborated by the observation [13] that the ratio $R = \Gamma(dd \longrightarrow {}^3\mathrm{He} + n)/\Gamma(dd \longrightarrow T + p)$ changes after transition to the nonresonant $dd\mu$ formation because this ratio is different for reactions proceeding from the rotational $K = 1$ state and from the S-wave state with even rotational numbers and spins. The rate of $dd\mu$ formation from the $d\mu(F = 3/2)$ state depends only slightly on the temperature and begins to decrease only at $T \simeq 26$ K. The temperature dependence of the mesic molecule formation rate, which was measured in dense gaseous and liquid deuterium [7–15], agrees well with the theoretical calculations [6, 7] (see Fig. 1). However, the $dd\mu$ formation rate measured in 3-K solid deuterium [16] is higher than the theoretical predictions by more than an order of magnitude. Careful measurements [17], which were carried out in solid and liquid deuterium at the same setup in the temperature range 5–50 K, corroborated this result (see Fig. 2). It was found that the rate of the resonant $dd\mu$ formation from the $d\mu(F = 3/2)$ state is virtually unchanged at $T \simeq 20$ K and below. In agreement with the theory, the rate of the nonresonant formation from the $d\mu(F = 1/2)$ state is also unchanged. The rate of the transition $d\mu(F = 3/2) \longrightarrow d\mu(F = 1/2)$ ($\lambda_d \approx 3.1 \times 10^7$ s^{-1}) between the hyperfine levels of mesic atoms is virtually unchanged as well. Thus, the behavior is paradoxical; the process occurs as if the $d\mu$ mesic atoms in the hyperfine 3/2 state conserve their energy and are not thermalized when the temperature decreases below 20 K. In this paper, I will demonstrate that this phenomenon is naturally explained by the

character of the energy loss of slow $d\mu$ atoms in a crystal lattice and is independent of the lattice structure.

Because $d\mu$ atoms are electrically neutral and have small sizes, their scattering in a crystal is similar to slow-neutron scattering. Even in 1937, Pomeranchuk [18] demonstrated that the neutron elastic scattering at sufficiently low temperatures proceeds from the whole crystal lattice and is not accompanied by energy loss. (We can only regret that, obtaining this result, Pomeranchuk did not predict the Mössbauer effect in 1937.) Inelastic collisions are predominantly related to the one-phonon lattice excitation, and the mean free path l_{in} with respect to these collisions is longer than the mean free path l_{el} with respect to elastic collisions. According to [18], one has for identical nuclei, when the neutron wavelength is shorter than the lattice constant,

$$l_{in} = \frac{7}{8} l_{el} \left(\frac{k_B \Theta}{E} \right)^3, \quad (1)$$

where k_B is the Boltzmann constant, $E = k_B T$ is the neutron energy, and Θ is the Debye temperature. It is obvious that $l_{in} > l_{el}$ for $E < k_B \Theta$. In this case, if the neutron-capture mean free path $l_c = 1/N\sigma_c$, where σ_c is the capture cross section and N is the density of nuclei, is considerably shorter than l_{in}, deceleration of neutrons will stop and capture of neutrons by nuclei will occur before neutron thermalization. Similar consideration applies to the behavior of $d\mu$ mesic atoms in a crystal lattice.

Calculations [19] demonstrated that the cross section for the elastic scattering of slow $d\mu$ atoms in the upper hyperfine 3/2 state on deuterons at energies below 0.1 eV is virtually constant and has the value

$$\sigma_{el} \simeq 2 \times 10^{-19} \text{ cm}^2, \quad (2)$$

and the mean free path related to the resonant $dd\mu$ formation is

$$l_{dd\mu} = \frac{1}{N\sigma_{dd\mu}} = \frac{v}{\lambda_{dd\mu}}, \quad (3)$$

where $\lambda_{dd_\mu} = 2.27 \times 10^6 \text{ s}^{-1}$ is the mesic-molecule formation rate and v is the $d\mu$ velocity, which is $v = (3k_B T/M_d)^{1/2}$ under the thermalization conditions. From the condition $l_{dd\mu} < l_{in}$ and Eqs. (1)–(3), we can estimate the temperature at which the inelastic-scattering mean free path is equal to the mean free path of $dd\mu$ formation:

$$T \le 0.82 \left(\frac{M_d}{k_B} \right)^{1/7} \left(\frac{\lambda_{dd\mu}}{N\sigma_{el}} \right)^{2/7} \Theta^{6/7}, \quad (4)$$

which, at the deuteron Debye temperature $\Theta = 74$ K and the density of nuclei $N = 4.25 \times 10^{22} \text{ cm}^{-3}$, yields

$$T \le 13 \text{ K}. \quad (5)$$

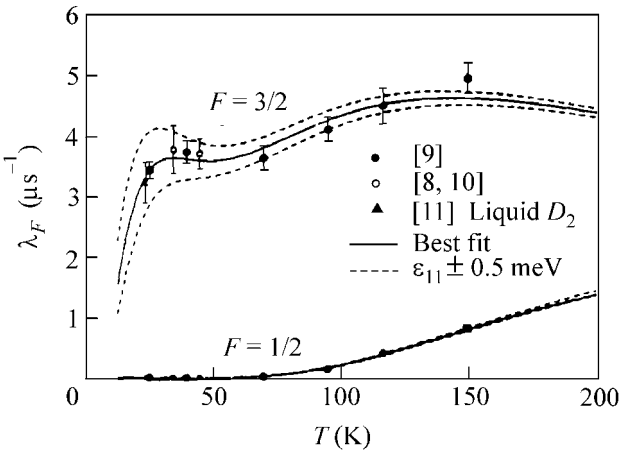

Fig. 1. The mesic molecule formation rates $\bar{\lambda}_{1/2}$ and $\bar{\lambda}_{3/2}$ from all experiments carried out at the Paul Scherrer Institute (Switzerland) and fits presented in [7].

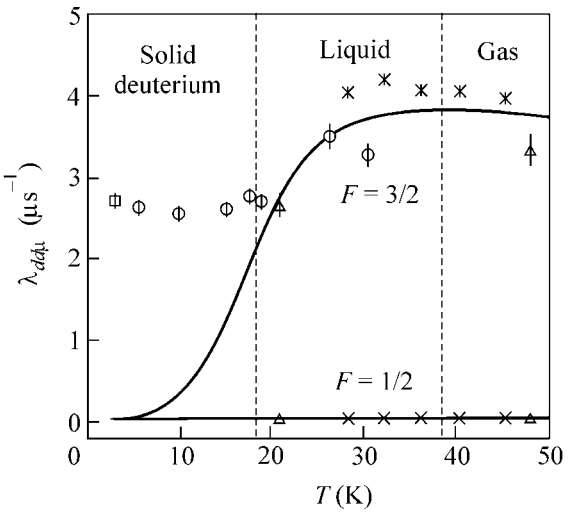

Fig. 2. The temperature dependence of the mesic molecule formation rate in deuterium for various spin states of deuterium mesic atoms. The circles, square, triangle, and crosses are experimental data taken from [17], [16], [15], and [13], respectively. The solid lines are theoretical predictions taken from [6, 7].

Taking into account that the $d\mu$ atoms, which are formed in the ground state with a mean energy of 1–2 eV, are thermalized at a distance of several inelastic mean free paths, we conclude that the resonant mesic molecule formation in solid deuterium occurs before the thermalization of $d\mu$ mesic atoms.

This explains the observed temperature independence of the muonic catalysis in solid deuterium.

It should be mentioned that the epithermal formation of the $dd\mu$ mesic molecules was previously observed in a substance consisting of HD molecules [20]. This was attributed to the fact that the effective

cross section for the scattering of $d\mu$ mesic atoms by protons is small due to the Ramsauer effect [21] and, therefore, the energies of decelerating $d\mu$ mesic atoms fall with certain probability within the range of the resonant formation of higher vibrational states of the $[dd\mu, d]2e$ complex. According to estimations [22], a solid deuterium crystal lattice only slightly affect the resonant $dt\mu$ formation rate because of the difference in the position and width of the resonance level for formation of the mesic molecules $dt\mu$ and $dd\mu$ [22]. However, this statement should be experimentally verified.

After this paper had been written, I heard that the hypothesis of epithermal $dd\mu$ formation in solid deuterium was suggested by L.I. Ponomarev on the basis of an analysis of experimental data. A qualitative idea that the energy loss of $d\mu$ mesic atoms decreases in solid deuterium was also proposed in [16, 23]. This paper was discussed at the International Conference on Muonic Catalysis MuCF01 in Japan, April 22–26, 2001, where A. Adamchak and M. Faĭfman presented work containing similar ideas.

I am grateful to L.I. Ponomarev and G.G. Semenchuk for stimulating discussion and valuable remarks. This work was supported by the Russian Foundation for Basic Research, project nos. 99-02-16558 and 00-15-96645.

REFERENCES

1. S. S. Gershteĭn, Candidate's Dissertation (Inst. Fiz. Probl., Moscow, 1958).
2. Ya. B. Zel'dovich and S. S. Gershteĭn, Usp. Fiz. Nauk **71**, 581 (1960) [Sov. Phys. Usp. **3**, 593 (1961)].
3. S. I. Vinitskiĭ, L. I. Ponomarev, I. V. Puzynin, *et al.*, Zh. Éksp. Teor. Fiz. **74**, 849 (1978) [Sov. Phys. JETP **47**, 444 (1978)].
4. É. A. Vesman, Pis'ma Zh. Éksp. Teor. Fiz. **5**, 113 (1967) [JETP Lett. **5**, 91 (1967)].
5. S. S. Gershteĭn, Zh. Éksp. Teor. Fiz. **40**, 695 (1961) [Sov. Phys. JETP **13**, 488 (1961)].
6. L. I. Men'shikov, L. I. Ponomarev, T. A. Strizh, and M. P. Faĭfman, Zh. Éksp. Teor. Fiz. **92**, 1173 (1987) [Sov. Phys. JETP **65**, 656 (1987)]; M. P. Faĭfman, L. I. Men'shikov, and T. A. Strizh, Muon Catal. Fusion **4**, 1 (1980).
7. A. Scrinzi, P. Kammel, J. Zmeskal, *et al.*, Phys. Rev. A **47**, 4691 (1993).
8. P. Kammel, W. H. Breunlich, M. Cargnelli, *et al.*, Phys. Lett. B **112**, 319 (1982); Phys. Rev. A **28**, 2611 (1983).
9. J. Zmeskal, P. Kammel, A. Scrinzi, *et al.*, Phys. Rev. A **42**, 1165 (1990).
10. M. Cargnelli *et al.*, in *Proceedings of the Twenty-Third Yamada Conference on Nuclear Weak Processes and Nuclear Structure, Osaka, 1989*, Ed. by M. Morita *et al.* (World Scientific, Singapore, 1989), p. 115.
11. N. Nagel *et al.*, Nucl. Phys. A **439**, 397 (1989).
12. W. H. Breunlich, P. Kammel, J. S. Cohen, *et al.*, Annu. Rev. Nucl. Sci. **39**, 311 (1989).
13. C. Petitjean, D. V. Balin, W. H. Breunlich, *et al.*, Hyperfine Interact. **118**, 127 (1999).
14. C. Petitjean, P. Ackerbauer, D. V. Balin, *et al.*, Hyperfine Interact. **101/102**, 1 (1996); C. Petitjean, D. V. Balin, W. H. Breunlich, *et al.*, Hyperfine Interact. **118**, 127 (1999).
15. V. P. Dzhelepov, V. G. Zinov, S. A. Ivanovskiĭ, *et al.*, Zh. Éksp. Teor. Fiz. **101**, 1105 (1992) [Sov. Phys. JETP **74**, 589 (1992)].
16. P. E. Knowles, G. A. Beer, G. R. Masson, *et al.*, Phys. Rev. A **56**, 1970 (1997); Hyperfine Interact. **101/102**, 21 (1996).
17. D. L. Demin, V. P. Dzhelepov, V. V. Fil'chenkov, *et al.*, Zh. Éksp. Teor. Fiz. **111**, 1163 (1997) [JETP **84**, 641 (1997)].
18. I. Ya. Pomeranchuk, Zh. Éksp. Teor. Fiz. **8**, 394 (1937) [Phys. Z. Sowjetunion **13**, 65 (1938)].
19. L. Bracci, C. Chiccoli, G. Fiorentini, *et al.*, *The Atlas of the Cross Sections of Mesic Atomic Processes* (Universita degli studi di Pisa, Pisa, 1990), IFUP-TH 21/90.
20. G. G. Semenchuk, D. V. Balin, T. Case, *et al.*, Hyperfine Interact. **118**, 141 (1999).
21. S. Cohen, D. L. Judd, R. J. Riddel, *et al.*, Phys. Rev. **110**, 1471 (1958); **119**, 384 (1960).
22. K. Fukushima, Hyperfine Interact. **82**, 161 (1993).
23. A. Adamchak, Hyperfine Interact. **101/102**, 113 (1996); C. L. Gurin and L. I. Menshikov, Hyperfine Interact. **118**, 147 (1999).

Translated by R. Tyapaev

JETP Letters, Vol. 73, No. 11, 2001, pp. 587–591. From Pis'ma v Zhurnal Éksperimental'noĭ i Teoreticheskoĭ Fiziki, Vol. 73, No. 11, 2001, pp. 667–671.

The Bubbles of Matter from Multiskyrmions[1]

V. B. Kopeliovich

Institute for Nuclear Research, Russian Academy of Sciences, Moscow, 117312 Russia
e-mail: kopelio@al20.inr.troitsk.ru

Received May 7, 2001

Approximate analytical solutions describing the skyrmions given by rational-map ansatz are obtained. At large baryon numbers, these solutions are similar to the domain wall or to spherical bubbles with energy and baryon number density concentrated at their boundary. A rigorous upper bound is obtained for the masses of rational map multiskyrmions, which is close to known masses, especially at large B. The main properties of bubbles of matter are obtained for an arbitrary number of flavors. © *2001 MAIK "Nauka/Interperiodica".*

PACS numbers: 12.39.Dc

1. Among many known soliton models used in different fields of physics, the chiral soliton approach starting with a few basic concepts and ingredients incorporated in the model lagrangian [1, 2] provides, probably, the most realistic description of baryons and baryonic systems. The latter appear within this approach as quantized solitonic solutions of equations of motion characterized by the so-called winding number or topological charge which is identified with baryon number B. Numerical studies have shown that the chiral field configurations of lowest energy possess different topological properties—the shape of the mass and B-number distribution—for different values of B. It is a sphere for $B = 1$ hedgehog [1], a torus for $B = 2$, a tetrahedron for $B = 3$, a cube for $B = 4$, and higher polyhedrons for greater baryon numbers. The symmetries of various configurations for B up to 22 and their masses have been determined in [3] (the references to earlier original papers can be found in [3, 4]). These configurations have a one-shell structure, and for $B > 6$ all of them, except for two cases, are formed from 12 pentagons and $2B$-14 hexagons; in carbon chemistry, similar structures are known as fullerenes [3c].

A remarkable feature of the whole approach is that the baryons/nucleons individuality is absent in the lowest energy static configurations, and the conventional picture of nuclei should appear when nonzero modes motion—vibration, breathing, etc.—are taken into account (see, e.g., discussion in [4]). The so-called rational-map (RM) ansatz, proposed for skyrmions in [5] and widely used now, allows one to simplify the problem of finding the configurations of lowest energy. As will be shown here, many important properties of RM multiskyrmions can be studied analytically, and this allows one to make some conclusions for arbitrary large B and any number of flavors N_F independently of the presence of numerical calculations.

So far, the chiral soliton models have been considered as a special class of models. Their connection with other soliton models would be of interest, and this is also an issue of the present paper.

2. Here, we consider large B multiskyrmions described by the RM ansatz mainly in the $SU(2)$ model and also in the $SU(3)$ variant using the projector ansatz in this case [6]. In the $SU(2)$ model, the chiral fields are functions of profile f and unit vector $\mathbf{n}$, according to the definition of the unitary matrix $U \in SU(2)$ $U = c_f + is_f\mathbf{n}\boldsymbol{\tau}$. For the ansatz based on rational maps, the profile f depends only on the variable r, and the components of vector $\mathbf{n}$, on the angular variables θ, ϕ. $n_1 = (2\mathrm{Re}R)/(1 + |R|^2)$, $n_2 = (2\mathrm{Im}R)/(1 + |R|^2)$, $n_3 = (1 - |R|^2)/(1 + |R|^2)$, where R is a rational function of variable $z = \tan(\theta/2)\exp(i\phi)$ defining the map of degree $\mathcal{N}$ from $S^2 \longrightarrow S^2$.

The following notation is used [5]:

$$\mathcal{N} = \frac{1}{8\pi}\int r^2(\partial_i\mathbf{n})^2 d\Omega = \frac{1}{4\pi}\int\frac{2idRd\bar{R}}{(1+|R|^2)^2},$$

$$\mathcal{J} = \frac{1}{4\pi}\int r^4\frac{[\boldsymbol{\partial}n_1\boldsymbol{\partial}n_2]^2}{n_3^2}d\Omega \qquad (1)$$

$$= \frac{1}{4\pi}\int\left(\frac{(1+|z|^2)}{(1+|R|^2)}\frac{|dR|}{|dz|}\right)^4\frac{2idzd\bar{z}}{(1+|z|^2)^2},$$

where Ω is a solid angle. For $B = 1$ hedgehog, $\mathcal{N} = \mathcal{J} = 1$. $\mathcal{N} = B$ for the configurations of lowest energy.

[1] This article was submitted by the author in English.

The classical mass of the skyrmion for the RM ansatz in universal units $3\pi^2 F_\pi/e$ is [5, 6]

$$M = \frac{1}{3\pi}\int\left\{A_N r^2 f'^2 + 2Bs_f^2(f'^2+1) + \mathcal{J}\frac{s_f^4}{r^2}\right\}dr; \quad (2)$$

r is measured in units $2/F_\pi e$, where we inserted the coefficient $A_N = 2(N-1)/N$ for symmetry group $SU(N)$ [6] to make it possible to consider models with arbitrary number of flavors $N = N_F$, essentially nonembeddings of $SU(2)$ in $SU(N)$. To find the minimal energy configuration at fixed $\mathcal{N} = B$, one minimizes $\mathcal{J}$, and then finds the profile $f(r)$ by minimizing energy (2). The $\mathcal{J} \geq B^2$ inequality takes place [5, 6]. Direct numerical calculations have shown, and the analytical treatment here supports, that, at large B and, hence, large $\mathcal{J}$, a multiskyrmion looks like a spherical bubble with profile $f = \pi$ inside and $f = 0$ outside. The energy and B-number density of this configuration is concentrated at its boundary, similar to the domain wall system considered in [7] in connection with cosmological problems.

Denote $\phi = \cos f$; then, energy (2) can be represented as

$$M = \frac{1}{3\pi}\int\left\{\frac{1}{(1-\phi^2)}[A_N r^2\phi'^2 + 2B(1-\phi^2)^2] + 2B\phi'^2 + \mathcal{J}(1-\phi^2)^2/r^2\right\}dr, \quad (3)$$

with ϕ changing from –1 at $r = 0$ to 1 at $r \longrightarrow \infty$. The first half of Eq. (3) is the second-order term contribution to the mass, and the second is the Skyrme term contribution. At fixed $r = r_0$, the latter coincides exactly with one-dimensional domain wall energy. It is possible to write the second-order contribution in Eq. (2) in the form

$$M^{(2)} = \frac{1}{3\pi}\int\left\{\frac{A_N r^2}{(1-\phi^2)}\left[\phi' - \sqrt{\frac{2B}{A_N}}(1-\phi^2)/r\right]^2 + 2r\sqrt{2A_N B}\phi'\right\}dr, \quad (4)$$

and similarly for the fourth-order Skyrme term. The equality $\phi' = \sqrt{2B/A_N}(1-\phi^2)/r$ eliminates a considerable part of the integrand in Eq. (4). Therefore, it is natural to consider function ϕ satisfying the following differential equation:

$$\phi' = \frac{b}{2r}(1-\phi^2), \quad (5)$$

which has a solution satisfying boundary conditions $\phi(0) = -1$ and $\phi(\infty) = 1$:

$$\phi = \frac{(r/r_0)^b - 1}{(r/r_0)^b + 1} \quad (6)$$

with arbitrary r_0, the distance from the origin of the point where $\phi = 0$ and profile $f = \pi/2$. r_0 can be considered as a radius of multiskyrmion.

After substitution of this ansatz, one obtains the soliton mass in the form

$$M(B, b) = \frac{1}{3\pi}\int\{(A_N b^2/4 + 2B)(1-\phi^2) + (Bb^2/2 + \mathcal{J})(1-\phi^2)^2/r^2\}dr. \quad (7)$$

Integrating over dr using known expressions for the Euler type integrals, e.g.,

$$\int_0^\infty \frac{dr}{1+(r/r_0)^b} = \frac{r_0\pi}{b\sin(\pi/b)}, \quad b > 1,$$

allows one to obtain the mass of the multiskyrmion in simple analytical form as a function of parameters b and r_0

$$M(B, r_0, b) = \frac{4}{3b^2\sin(\pi/b)}\left[(A_N b^2/4 + 2B)r_0 + \frac{1}{3r_0}(Bb^2 + 2\mathcal{J})(1-1/b^2)\right], \quad (8)$$

which gives after simple minimization in r_0

$$r_0^{\min} = 2\left[\frac{(Bb^2 + 2\mathcal{J})(1-1/b^2)}{3(A_N b^2 + 8B)}\right]^{1/2} \quad (9)$$

and

$$M(B, b)/B = \frac{4}{3b\sin(\pi/b)} \times [(b^2 + 2\mathcal{J}/B)(A_N b^2 + 8B)(1-1/b^2)/(3b^2 B)]^{1/2}. \quad (10)$$

For any value of the power b, Eq. (10) provides an upper bound for the mass of *RM* skyrmion. To get a better bound, we should minimize Eq. (10) with respect to b. At large enough B, when it is possible to neglect the influence of slowly varying factors $(1 - 1/b^2)$ and $b\sin(\pi/b)$, we easily obtain that

$$b_{\min} = b_0 = 2(\mathcal{J}/A_N)^{1/4}, \quad r_0^{\min} \simeq \left[\frac{2}{3}\left(\sqrt{\frac{\mathcal{J}}{A_N}} - \frac{1}{4}\right)\right]^{1/2} \quad (11)$$

and, therefore,

$$\frac{1}{3}(2+\sqrt{\mathcal{I}A_N}/B) < \frac{M}{B} \le \frac{1}{3}(2+\sqrt{\mathcal{I}A_N}/B) \times \frac{4}{b_0\sin(\pi/b_0)}\left[\frac{2}{3}\left(1-\frac{1}{4}\sqrt{A_N/\mathcal{I}}\right)\right]^{1/2}. \quad (12)$$

The lower bound in Eq. (12) was known previously [5, 6]. The correction to the value b_0 can be found including in the minimization procedure the factor $(1 - 1/b^2)$ and variation of $b\sin(\pi/b) \approx \pi[1 - \pi^2/6b^2]$. It gives

$$\delta b = \frac{B(\pi^2/3-1)(2+\sqrt{A_N\mathcal{I}}/B)^2}{16\mathcal{I}^{3/4}A_N^{1/4}}, \quad (13)$$

and the value $b = b_0 + \delta b$ should be inserted into Eq. (10). This improves the values of M/B for $B = 1, 2, 3 \ldots$ but provides a negligible effect for $b \sim 17$ and greater, since $\delta b \sim 1/\sqrt{B}$. The comparison of the numerical result and analytical upper bound (12) is given in the table.

Numerically, Eqs. (10)–(13) provide an upper bound which differs from the masses of all known *RM* skyrmions within ~2%, beginning with $B = 4$ (see table). Even for $B = 1$, where the method evidently should not work well, we obtain $M = 1.289$ instead of the precise value $M = 1.232$. For maximal values of B between 17 and 22, where the value of $\mathcal{I}$ is calculated, the upper bound exceeds the RM value of mass by 0.5% only. We took here the ratio $R_{I/B} = \mathcal{I}/B^2$ in the cases where this ratio is not determined yet, the same as for highest B, where it is known; i.e., 1.28 for $SU(2)$ case [3] and $B = 32$, 64, and 1.037 for $B > 6$ in $SU(3)$ [6]. For $R_{I/B} = 1$, the numbers in the table decrease by ~0.1% only in the latter case. Note also that asymptotically at large B the ratio of upper and lower bounds

$$\frac{M_{\max}}{M_{\min}} = \frac{4}{\pi}\left(\frac{2}{3}\right)^{1/2} \simeq 1.0396; \quad (14)$$

i.e., the gap between upper and lower bounds is less than 4%, independently of B, the particular value of $\mathcal{I}$, and the number of flavors N. With decreasing $\mathcal{I}$, the upper bound decreases proportionally to the lower bound. In view of such a good quantitative agreement of analytical and numerical results, the studies of basic properties of bubbles of matter made in the present paper are quite reliable.

The width (or thickness) W of the bubble shell can be estimated easily. We can define the half-width as a distance between the points where $\phi = \pm 1/2$; then,

$$W = \left[\frac{2}{3}\left(1-\frac{1}{b_0^2}\right)\right]^{1/2}\ln 3. \quad (15)$$

It is clear that, at large B, W is constant and does not depend on the number of flavors N either. The radius of bubble (11) grows with increasing B like $[\mathcal{I}/A_N]^{1/4}$.

Previously, we considered large B skyrmion within the "inclined step" approximation [4]. Let W be the width of the step, and r_0 the radius of the skyrmion where the profile $f = \pi/2$. $f = \pi/2 - (r - r_0)\pi/W$ for $r_0 - W/2 \le r \le r_0 + W/2$. This approximation describes the usual domain-wall energy [7] with an accuracy of ~9.5%.

We wrote the energy in terms of W, r_0, then minimized it with respect to both of these parameters, and found the minimal value of energy:

$$M(W, r_0) = \frac{\Lambda}{3\pi}\left[\frac{\pi^2}{W}(B + A_N r_0^2) + W\left(B + \frac{3\mathcal{I}}{8r_0^2}\right)\right]. \quad (16)$$

This gave

$$W_{\min} = \pi\left[\frac{B + A_N r_0^2}{B + 3\mathcal{I}/8r_0^2}\right]^{1/2} \quad (17)$$

and, after minimization, $r_{0\min}^2 = \sqrt{3\mathcal{I}/8A_N} \simeq 0.612\sqrt{\mathcal{I}/A_N}$, close to the above result $r_{0\min}^2 \simeq$

The skyrmion mass unit B-number in universal units $3\pi^2 F_\pi/e$ for *RM* configurations, approximate and exact solutions. The approximate values are calculated using Eq. (10) with the power $b = b_0 + \delta b$. The numerical values for $SU(2)$ model are from [3] and earlier papers. The last three lines show the result for $SU(3)$ projector ansatz [6] and approximation to this case, $A_N = 4/3$

B	2	3	4	5	6	7	13	17	22	32	64
$M/B\|_{\mathrm{RM}}$	1.208	1.184	1.137	1.147	1.137	1.107	1.098	1.092	1.092	–	–
$b(B)$	3.89	4.47	4.85	5.39	5.80	6.03	8.00	9.02	10.23	12.24	17.2
$M/B\|_{appr}$	1.229	1.198	1.151	1.158	1.147	1.117	1.106	1.0976	1.098	1.094	1.089
$M/B\|_{num}$	1.1791	1.1462	1.1201	1.1172	1.1079	1.0947	1.0834	1.0774	1.0766	–	–
$M/B\|_{\mathrm{RM}}^{SU_3}$	1.222	1.215	1.184	1.164	1.146	–	–	–	–	–	–
$b(B)^{SU_3}$	3.57	4.08	4.47	4.83	5.13	5.46	7.13	8.06	9.09	10.86	15.19
$M/B\|_{appr}^{SU_3}$	1.259	1.231	1.198	1.176	1.156	1.149	1.127	1.121	1.116	1.111	1.106

$0.667\sqrt{\mathcal{I}/A_N}$. In the dimensional units, $r_0 = (6\mathcal{I}/A_N)^{1/4}/F_\pi e$. Since $\mathcal{I} \geq B^2$, the radius of minimized configuration grows as $\sqrt{B}$ at least. $W_{\min} = \pi$; i.e., it does not depend on B for any $SU(N)$, similar to previous result (15), which gives $W \simeq 1.8$ for large B, all in units $2/F_\pi e$. The energy

$$M_{\min} \simeq (2B + \sqrt{3A_N\mathcal{I}/2})/3. \qquad (18)$$

For the $SU(2)$ model, $A_N = 1$ and the energy $M_{\min} = (2B + \sqrt{3\mathcal{I}/2})/3$. The formula gives the numbers for $B = 3, \ldots, 22$, in 2–3% agreement with calculation within the RM approximation [3, 5].

A more detailed analytical calculation made here confirms the results of such "toy model" approximation, and both reproduce the picture of RM skyrmions as a two-phase object, a spherical bubble with profile $f = \pi$ inside and $f = 0$ outside, and a fixed-thickness shell with fixed surface energy density, $\rho_M^{\text{surf}} \simeq (2B + \sqrt{3\mathcal{I}A_N/2})/12\pi r_0^2$. The average volume density of mass in the shell is

$$\rho_M^{\text{vol}} = \frac{3\pi}{64W}(2B + \sqrt{\mathcal{I}A_N})\sqrt{A_N/\mathcal{I}}F_\pi^4 e^2, \qquad (19)$$

and for $SU(2)$ model at large B it is approximately equal to ~0.6 GeV/Fm^3 for a reasonable choice of model parameters $F_\pi = 0.186$ GeV, $e = 4.12$ [4]; i.e., it is few times greater than the normal density of nuclei.

3. Consider also the influence of the chiral symmetry breaking mass term (M.t.) which is described by the Lagrangian

$$\text{M.t.} = \tilde{m}\int r^2(1 - \cos f)dr, \quad \cos f = \phi, \qquad (20)$$

$\tilde{m} = 8\mu^2/3\pi F_\pi^2 e^2$, $\mu = m_\pi$. For strangeness, charm, or bottom, the masses m_K, m_D, or m_B can be inserted instead of m_π.

Instead of the above Eq. (8), we now obtain

$$M(B, r_0, b) = \alpha(B, b)r_0 + \beta(B, b)/r_0 + mr_0^3 \qquad (21)$$

with α, β given in Eq. (8) and $m = 2\pi\tilde{m}/b\sin(3\pi/b)$. It is possible to obtain a precise minimal value of the mass

$$M(B, b) = \frac{2r_0^{\min}}{3}(\sqrt{\alpha^2 + 12m\beta} + 2\alpha) \qquad (22)$$

for the value of r_0

$$r_0^{\min}(B, b) = \left[\frac{\sqrt{\alpha^2 + 12m\beta} - \alpha}{6m}\right]^{1/2}. \qquad (23)$$

When the mass m is small enough, the expansion in $12m\beta/\alpha^2$ can be made, and one obtains the following reduction of dimension r_0,

$$r_0 \longrightarrow r_0 - \frac{3m}{2\alpha}\left(\frac{\beta}{\alpha}\right)^{3/2}$$
$$\simeq \sqrt{\frac{2}{3}}\left(\frac{\mathcal{I}}{A_N}\right)^{1/4}\left[1 - \frac{3\pi m}{2(2B + \sqrt{\mathcal{I}A_N})}\left(\frac{\mathcal{I}}{A_N}\right)^{3/4}\right], \qquad (24)$$

and increase of the soliton mass

$$\delta M = M\frac{m\beta}{2\alpha^2}\left[1 - \frac{9m\beta}{8\alpha^2}\right] \simeq Mm\frac{\pi(\mathcal{I}A_N)^{3/4}}{2(2B + \sqrt{\mathcal{I}A_N})}. \qquad (25)$$

We used that at large B

$$\alpha \simeq \frac{1}{3\pi}\left(A_N b + \frac{8B}{b}\right), \quad \beta \simeq \frac{4}{9\pi}\left(Bb + \frac{2\mathcal{I}}{b}\right). \qquad (26)$$

As was expected from general grounds, dimensions of the soliton decrease with increasing m. However, even for a large value of m, the structure of the multiskyrmion at large B remains the same: the chiral symmetry broken phase inside the spherical wall where the main contribution to the mass and topological charge is concentrated. The value of the mass density inside the bubble is defined completely by the mass term with $1 - \phi = 2$. The baryon number density distribution is quite similar, with the only difference that inside the bag it equals zero. It follows from these results that RM-approximated multiskyrmions cannot model real nuclei at large B, probably $B > 12$–20, and configurations like skyrmion crystals [8] may be more valid for this purpose.

It is of interest to study what happens at very large values of the mass, when $12m\beta \gg \alpha^2$. Making an expansion in $\alpha^2/12m\beta$, we obtain

$$r_0^{\min} \simeq [\beta/3m]^{1/4}, \quad M_{m\to\infty}(B, b) \simeq \frac{4}{3}(3m\beta^3)^{1/4}. \qquad (27)$$

Minimization of $M(B, b)$ with respect to b gives $b_0^{\min} = \sqrt{2\mathcal{I}/B}$, $\beta^{\min} = 8\sqrt{2\mathcal{I}B}/9\pi$ and

$$M_{m\to\infty}(B) \simeq \frac{16}{9}[4\sqrt{2}m/3\pi^3]^{1/4}[B\mathcal{I}]^{3/8}. \qquad (28)$$

So, in this extreme case $b \sim \sqrt{B}$, $r_0 \sim (\mu)^{-1/2}B^{3/8}$, the mass of the soliton increases as $M \sim \sqrt{\mu}\,B^{9/8}$, and the binding should become weaker with increasing m and baryon number of the skyrmion.

It is possible also to calculate analytically the tensors of inertia of multiskyrmion configurations within this approximation; see [4] for definitions and formulas.

4. By means of consideration of a special class of functions (6), we established the link between topological soliton models in the rational-map approximation

and the soliton models of "domain-wall" or "spherical-bubble" type. Of course, it is a domain wall of a special kind, similar to a honeycomb. The upper bound for the energy of multiskyrmions is obtained which is very close to the known energies of RM multiskyrmions, especially at largest B, and is higher than the known lower bound by ~4% only.

The following properties of bubbles of matter from RM multiskyrmions are established analytically, mostly independent of particular values of the quantity $\mathcal{J}$.

The dimensions of the bubble grow with B as $\sqrt{B}$, or as $\mathcal{J}^{1/4}$, whereas the mass is proportional to ~B at large B. Dimensions of the bubble decrease slightly with increasing N—the number of flavors, $r_0 \sim [N/(2(N-1))]^{1/4}$; see Eqs. (11) and (12).

The thickness of the bubble envelope (15) is constant at large B and does not depend on the number of flavors; therefore, the average surface mass density is constant at large B, as well as the average volume density of the shell. Both densities increase slightly with increasing N. At the same time, the mass and B-number densities of the whole bubble $\longrightarrow 0$ when $B \longrightarrow \infty$, and this contradicts the nuclear physics data.

It follows from the above consideration that the spherical bubble or bag configuration can be obtained from the Lagrangian written in terms of chiral degrees of freedom only; i.e., the Skyrme model Lagrangian leads at large baryon numbers to the formation of spherical bubbles of matter. This picture of mass distribution in RM multiskyrmions contradicts, at first sight, what is known about nuclei; however, it emphasizes the role of the periphery of the nucleus and could be an argument in favor of shell-type models. The skyrmion crystals [8] are believed to be more adequate for modeling nuclear matter.

It would be of interest to perform the investigation of the dynamics of bubbles in chiral soliton models similar to that performed recently for the simplified two-component sigma model, or sine-Gordon model in (3 + 1) dimensions [9]. Observations concerning the structure of large B multiskyrmions made here can be useful in view of possible cosmological applications of Skyrme-type models; see, e.g., [10]. The large-scale structure of the mass distribution in the Universe [11] is similar to that in topological soliton models, and it can be the consequence of the similarity of the laws in the micro- and macroworld.

I am indebted to P.M. Sutcliffe for informing me about the results of [3b, c] before publication and to W.J. Zakrzewski for interest in the questions discussed in this paper. This work was supported by the Russian Foundation for Basic Research, project no. 01-02-16615.

REFERENCES

1. T. H. R. Skyrme, Proc. R. Soc. London, Ser. A **260**, 127 (1961); Nucl. Phys. **31**, 556 (1962).
2. E. Witten, Nucl. Phys. B **223**, 433 (1983).
3. R. A. Battye and P. M. Sutcliffe, a) Phys. Rev. Lett. **79**, 363 (1997); b) hep-th/0012215 (2000); c) hep-th/0103026.
4. V. B. Kopeliovich, hep-ph/0103336; Zh. Éksp. Teor. Fiz. (2001) (in press).
5. C. Houghton, N. Manton, and P. Suttcliffe, Nucl. Phys. B **510**, 507 (1998).
6. T. Ioannidou, B. Piette, and W. J. Zakrzewski, J. Math. Phys. **40**, 6353 (1999); hep-th/9811071; J. Math. Phys. **40**, 6223 (1999).
7. Ya. B. Zeldovich, I. Yu. Kobzarev, and L. B. Okun, Zh. Éksp. Teor. Fiz. **67**, 3 (1974) [Sov. Phys. JETP **40**, 1 (1974)].
8. I. Klebanov, Nucl. Phys. B **262**, 133 (1985); E. Wust, G. E. Brown, and A. D. Jackson, Nucl. Phys. A **468**, 450 (1987).
9. T. I. Belova, V. A. Gani, and A. E. Kudryavtsev, Yad. Fiz. **64**, 143 (2001) [Phys. At. Nucl. **64**, 140 (2001)]; Yad. Fiz. **62**, 956 (1999) [Phys. At. Nucl. **62**, 895 (1999)].
10. B. Kleihaus and J. Kunz, Phys. Rev. D **57**, 834 (1998).
11. S. F. Shandarin, A. G. Doroshkevich, and Ya. B. Zeldovich, Usp. Fiz. Nauk **139**, 83 (1983) [Sov. Phys. Usp. **26**, 46 (1983)].

JETP Letters, Vol. 73, No. 11, 2001, pp. 592–596. Translated from Pis'ma v Zhurnal Éksperimental'noĭ i Teoreticheskoĭ Fiziki, Vol. 73, No. 11, 2001, pp. 672–676.

Noise Suppression by External Noise and Periodic Signal in a Dynamical System

S. L. Ginzburg, M. A. Pustovoĭt, and O. V. Gerashchenko*

St. Petersburg Nuclear Physics Institute, Russian Academy of Sciences, Gatchina, Leningrad region, 188350 Russia

** e-mail: gerashch@pnpi.spb.ru*

Received April 12, 2001; in final form, May 3, 2001

In a simple stochastic system, an overdamped Kramers oscillator with two—internal white and external colored—noise sources, the suppression of the noise component of the output signal spectrum with increasing intensity of the external noise or periodic signal is discovered and analyzed. © *2001 MAIK "Nauka/Interperiodica".*

PACS numbers: 05.40.Ca; 05.45.Gg; 02.50.Ey

1. Considerable recent attention has been focused on the constructive role of noise in nature. A large number of experimental facts in various fields of science corroborate the viewpoint that the influence of noise, which always accompanies all actual systems, is not restricted to destructive and thermodynamic effects. In particular, thermal or external noise of optimal nonzero intensity can improve the signal transfer when legitimate signals pass through nonlinear systems. The results on this phenomenon, which is referred to as stochastic resonance, were summarized in reviews [1, 2].

Most theoretical investigations on stochastic resonance were devoted to studying the signal passage through systems with one, usually white, noise source; the phenomenon is identified through the appearance of a maximum in the signal-to-noise ratio as a function of the noise intensity. However, the authors of [3, 4] examined systems with two noise sources, first without and then with a periodic signal. This problem formulation is physically natural and fruitful because each actual system involves internal thermal noise whose intensity is determined by the temperature. Controlling noise, as well as the signal, is fed to the system from outside. However, only the dependence of the signal passage on the internal-noise intensity has been examined in these problems until now. At the same time, in many cases, especially in biological systems, the temperature and, therefore, internal-noise power vary only within a narrow interval. On the other hand, the amplitudes of external noise and signal can vary within a wide range. This is the problem formulation that we consider in this study: varying parameters are the ratios of the amplitudes of controlling noise and signal to the internal noise intensity.

We explore a two-well dynamical system with a periodic rectangular signal and two noise sources, white (internal) and colored (external). The choice of a rectangular signal makes it possible to solve the problem for high signal amplitudes beyond the scope of perturbation theory.

We analyze the noise background, which is defined as the spectral density $S(0)$ of the output system signal at zero frequency.

We will report below the following new results: suppression of the noise background by a signal and suppression of the noise background by the external noise. It follows from these results that the signal-to-noise ratio (SNR) increases with increasing the external noise and signal. Note that the suppression of the noise background in a stochastic nondynamical system by external noise was recently found in [5].

We consider the following equation for the overdamped Kramers oscillator with two noise sources:

$$dx/dt = ax - bx^3 + F + z(t) + \sigma\xi(t) + AR(t),$$

$$z(t) = \frac{\Delta}{\sqrt{n}}\sum_{k=1}^{n} s_k(t), \quad s_k(t) = \pm 1,$$

$$\langle s_k(t)s_l(t')\rangle = \delta_{kl}\exp(-\gamma|t-t'|),$$

$$\langle z(t)z(t')\rangle = \Delta^2\exp(-\gamma|t-t'|),$$

$$\langle \xi(t)\xi(t')\rangle = \delta(t-t'),$$

$$R(t+T) = R(t) = \begin{cases} 1, & 0 < t \le T/2 \\ -1, & T/2 < t \le T. \end{cases} \qquad (1)$$

Here, $\xi(t)$ is the white noise; $z(t)$ is the colored noise, which is the sum of n dichotomic noises ($n = 1$ and ∞ correspond to ordinary dichotomic, or telegraph, noise and Gaussian noise, respectively); and a, b, F, σ, Δ, and A are constants.

The hierarchy of the characteristic times in Eq. (1) is very important. Denoting the correlation time of the

white (actual) noise as τ and assuming that $a \sim b$, we take the following hierarchy of times:

$$T \gg \gamma^{-1}, \quad w_0^{-1} \gg a^{-1} \gg \tau \longrightarrow 0, \tag{2}$$

where w_0 is the characteristic switching frequency induced by the white noise [see Eq. (6)].

We go over from Eq. (1) to the two-state model. It is convenient to define the energy $U_0(x)$ as

$$U_0(x) = -\frac{a}{2}x^2 + \frac{b}{4}x^4,$$
$$\delta U_0 = U_0(0) - U_0(\pm x_0) = \frac{a^2}{4b}, \quad x_0 = \sqrt{\frac{a}{b}}, \tag{3}$$

where $\pm x_0$ are the stable fixed points of Eq. (1) at $F = \Delta = A = \sigma = 0$.

If the conditions

$$\delta U_0 \gg \sigma^2, \quad \delta U_0 \gg \Delta x_0, \quad \delta U_0 \gg F x_0,$$
$$\frac{(\Delta x_0)^2}{\sigma^2 \delta U_0}, \quad \frac{(\Delta x_0)^2}{\sigma^2 \delta U_0} \ll 1 \tag{4}$$

are satisfied, $x(t)$ can be approximated by the dichotomic signal

$$x(t) = x_0 d(t), \quad d(t) = \pm 1. \tag{5}$$

Thus, we arrive at the two-state model. The time-dependent probabilities of transition between these two states are determined in the Kramers approximation as

$$\alpha(t) = w_{-1 \to 1} = w_0 \exp[p + q n^{-1/2} Q(t) + \nu R(t)],$$
$$\beta(t) = w_{1 \to -1} = w_0 \exp[-p - q n^{-1/2} Q(t) - \nu R(t)],$$
$$Q(t) = \sum_{k=1}^{n} s_k(t),$$
$$p = \frac{2x_0 F}{\sigma^2}, \quad q = \frac{2x_0 \Delta}{\sigma^2}, \tag{6}$$
$$\nu = \frac{2x_0 A}{\sigma^2}, \quad w_0 = \frac{a}{\pi\sqrt{2}} \exp\left(-\frac{a^2}{2b\sigma^2}\right).$$

Under conditions (2), we can write the following master equation for the distribution density of the nonstationary process $d(t)$:

$$\frac{dP(1,t)}{dt} = \alpha(t)P(-1,t) - \beta(t)P(1,t),$$
$$\frac{dP(-1,t)}{dt} = \beta(t)P(1,t) - \alpha(t)P(-1,t). \tag{7}$$

If the external noise $z(t)$ is fast, i.e., $\gamma \gg w_0$, the probabilities $\alpha(t)$ and $\beta(t)$ can be averaged over this fast noise. In this case, we arrive at a nonstationary stochastic process whose master equation has the form

$$\frac{dP(1,t)}{dt} = \alpha_1(t)P(-1,t) - \beta_1(t)P(1,t),$$
$$\frac{dP(-1,t)}{dt} = \beta_1(t)P(1,t) - \alpha_1(t)P(-1,t),$$
$$\alpha_1(t) = \langle \alpha(t) \rangle_z = w_0 e^{p + \nu R(t)} \cosh^n(q n^{-1/2}), \tag{8}$$
$$\beta_1(t) = \langle \beta(t) \rangle_z = w_0 e^{-p - \nu R(t)} \cosh^n(q n^{-1/2}).$$

It is easy to show that the solutions to Eqs. (7) and (8) for the fast noise ($\gamma \longrightarrow \infty$) coincide with each other. Indeed, let us consider some random variable $a(t)$ with the expectation value $\langle a(t) \rangle = a_1$ and correlation function $K_a(t) = \langle (a(t) - a_1)(a(0) - a_1) \rangle = a_2^2 \exp(-\gamma|t|)$. In the limit $\gamma \longrightarrow \infty$, we have $K_a(t) \longrightarrow 2a_2^2 \delta(t)/\gamma \longrightarrow 0$; i.e., $a(t)$ behaves as the nonrandom variable a_1. We recall that the white noise $\xi(t)$ makes a nonzero contribution because its correlation function is $\langle \xi(t)\xi(0) \rangle = \frac{\gamma}{2} \exp(-\gamma|t|) \longrightarrow \delta(t)$ in the limit $\gamma \longrightarrow \infty$. The difference between $a(t)$ and $\xi(t)$ is that $a_2^2 = \text{const}$, while $\langle \xi^2 \rangle = \gamma/2 \longrightarrow \infty$ in the limit $\gamma \longrightarrow \infty$.

Returning to $\alpha(t)$ and $\beta(t)$, we see that, e.g., at $n = 1$ and $\nu = 0$, the dispersion is $\langle (\alpha(t) - \alpha_1)^2 \rangle = w_0^2 \exp(2p) \sinh^2 q$ and does not increase in the limit $\gamma \longrightarrow \infty$; i.e., for the fast noise, $\alpha(t)$ can be replaced by $\alpha_1(t)$. This problem was analyzed in detail in, e.g., Section 3.2 of [6].

Taking into account time hierarchy (2), we can solve Eq. (8) in the adiabatic approximation. As a result, the irreducible correlation function averaged over the phase of the periodic signal R at large times $t \sim T$ has the form

$$K(t) = \langle x(t)x(0) \rangle_{z,R} - \langle x(t) \rangle_{z,R} \langle x(0) \rangle_{z,R}$$
$$= B\varphi_0(t) + C\delta(t),$$
$$\varphi_0(t) = \langle R(t)R(0) \rangle_R$$
$$= \frac{4}{\pi^2} \sum_{k=0}^{\infty} \frac{1}{(2k+1)^2} \exp(-i(2k+1)\Omega t), \tag{9}$$
$$B = \frac{x_0^2}{4} \{\tanh(p + \nu) - \tanh(p - \nu)\}^2,$$
$$C = \frac{x_0^2}{2w_0 \cosh^n(q n^{-1/2})}$$
$$\times \{\cosh^{-3}(p + \nu) + \cosh^{-3}(p - \nu)\}.$$

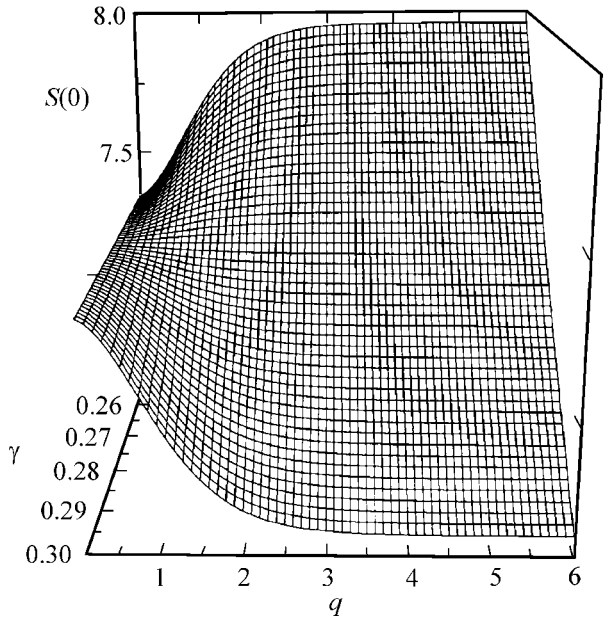

Fig. 1. The noise background as a function of the amplitude and switching frequency of external noise according to Eq. (14) for $\sigma^2 = 1$, $a = b = 1$, $w_0 \approx 0.13$. As γ increases, the amplification of the noise background is replaced by its suppression by the external noise [crossover occurs at $\gamma \approx 2w_0$ according to Eq. (14)].

The spectral density $S(\omega)$ is obtained by the Fourier transform of $K(t)$:

$$S(\omega) = \frac{8}{\pi} B \sum_{k=0}^{\infty} \frac{\delta[\omega - (2k+1)\Omega]}{(2k+1)^2} + C, \qquad (10)$$

which indicates that the noise background is $S(0) = C$. The signal-to-noise ratio, which is determined as the ratio of the intensity of the first harmonic to the background, is $SNR = 8B/\pi C$.

At $p = 0$, the expressions for the telegraph and Gaussian noises are, respectively,

$$S(0) = \begin{cases} \dfrac{x_0^2}{w_0 \cosh^3 \nu \cosh q}, & n = 1 \\ \dfrac{x_0^2}{w_0 \cosh^3 \nu} \exp\left(-\dfrac{q^2}{2}\right), & n = \infty, \end{cases} \qquad (11)$$

$$SNR = \begin{cases} \dfrac{8w_0}{\pi} \sinh^2 \nu \cosh \nu \cosh q, & n = 1 \\ \dfrac{8w_0}{\pi} \sinh^2 \nu \cosh \nu \exp\left(\dfrac{q^2}{2}\right), & n = \infty, \end{cases}$$

which demonstrates that, as the external noise q and/or signal ν increase, the noise background decreases and, for this reason, the SNR increases because the periodic component of the output signal is saturated.

Equations (9)–(11) were derived for the fast noise ($\gamma \gg w_0$). It is of interest to look into the behavior of the noise background $S(0)$ at arbitrary ratios of γ to w_0. Here, we consider a simple example of an exactly integrable problem. For $p = \nu = 0$, $n = 1$, the problem reduces to the four-state model [3, 4]. In this model, we deal with the stationary two-dimensional Markovian process $\{d(t), s(t)\}$ whose master equation has the form [4]

$$\frac{dP(d,s,t)}{dt} = w(-d,s)P(-d,s,t) - w(d,s)P(d,s,t) + \frac{\gamma}{2}[P(d,-s,t) - P(d,s,t)], \qquad (12)$$

$$w(d,s) = w_0 e^{-qsd}.$$

By solving this equation and calculating irreducible correlation functions, we obtain

$$K(t) = \frac{x_0^2}{(\alpha_0+\beta_0)^2 - \gamma^2}\{(4\alpha_0\beta_0 - \gamma^2) \times \exp[-(\alpha_0+\beta_0)|t|] + (\alpha_0-\beta_0)^2 \exp(-\gamma|t|)\},$$

$$S(\omega) = \frac{x_0^2}{(\alpha_0+\beta_0)^2 - \gamma^2}\left\{(4\alpha_0\beta_0 - \gamma^2) \times \frac{2(\alpha_0+\beta_0)}{\omega^2 + (\alpha_0+\beta_0)^2} + (\alpha_0-\beta_0)^2 \frac{2\gamma}{\omega^2+\gamma^2}\right\}, \qquad (13)$$

$$\alpha_0 = w_0 e^q, \quad \beta_0 = w_0 e^{-q}.$$

From this expression, it is easy to derive the expression for $S(0)$ at an arbitrary ratio of γ to w_0:

$$S(0) = \frac{x_0^2}{w_0 \cosh q}\left\{1 + \frac{2w_0}{\gamma}\frac{\sinh^2 q}{\cosh q + \dfrac{\gamma}{2w_0}}\right\},$$

$$S(0) = \begin{cases} \dfrac{2x_0^2}{\gamma}\tanh^2 q + \dfrac{x_0^2}{w_0}\cosh^{-3} q, & \gamma \ll w_0 \\ \dfrac{x_0^2}{w_0 \cosh q}, & \gamma \gg w_0. \end{cases} \qquad (14)$$

The latter formula in Eq. (14) coincides with the first formula in Eqs. (11) at $\nu = 0$. Thus, the background $S(0)$ increases with q in the limit $\gamma \ll w_0$ and decreases in the opposite limiting case. Figure 1 shows the background $S(0)$ as a function of q and γ and exhibits the clear-cut transition from amplification to suppression of the background $S(0)$ by the external noise when the switching frequency of the latter noise increases.

2. We carried out analog simulation of the effect of noise suppression by the electronic model of a two-

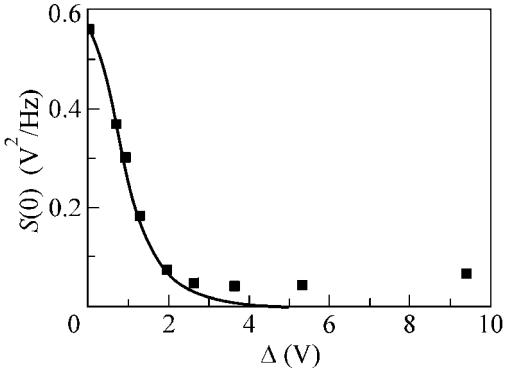

Fig. 2. The noise background $S(0)$ vs. the dichotomic-noise amplitude for $\gamma/2\pi \approx 350$ Hz. The frequency of switching induced exclusively by the white noise is $w_0/2\pi \approx 10$ Hz. The solid line is Eq. (14) for $\gamma \gg w_0$.

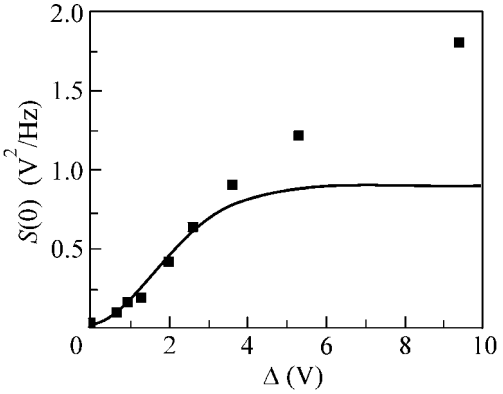

Fig. 3. The noise background $S(0)$ against the dichotomic-noise amplitude at $\gamma/2\pi \approx 10$ Hz. The switching frequency at $\Delta = 0$ is $w_0/2\pi \approx 180$ Hz. The solid line is Eq. (14) for $\gamma \ll w_0$.

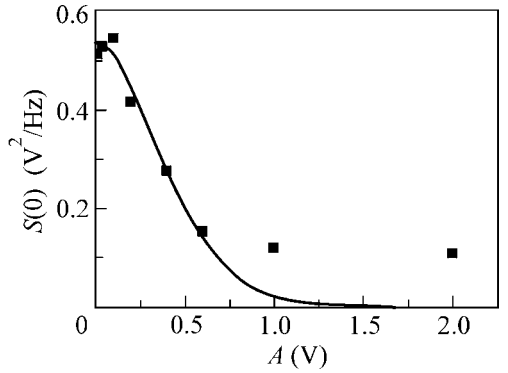

Fig. 4. The noise background $S(0)$ as a function of the amplitude of a rectangular signal with the frequency $\Omega/2\pi = 1$ Hz at $\Delta = 0$. The switching frequency at $A = 0$ is $w_0/2\pi \approx 10$ Hz. The solid line is Eq. (11) for $n = 1$ and $q = 0$.

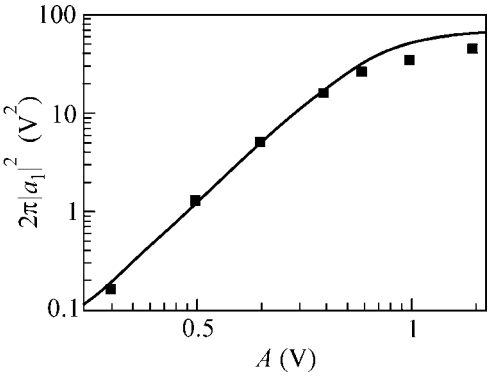

Fig. 5. The intensity of the output-signal first harmonic vs. the amplitude of a rectangular signal with the frequency $\Omega/2\pi = 1$ Hz at $\Delta = 0$. The solid line is $(8x_0^2/\pi)\tanh^2(v)$ [see Eqs. (9), (10) at $p = 0$].

level nonlinear system (an overdamped oscillator, which has a piecewise linear current–voltage characteristic and is similar to that used in [7, 8]). The fed voltage was a sum of the physical white Gaussian noise with a cutoff frequency of about 30 kHz, the dichotomic noise with the amplitude $0 \le \Delta \le 10$ V and cutoff frequency $0 \le \gamma/2\pi \le 2000$ Hz, and the rectangular ac signal with a frequency of $\Omega/2\pi = 1$ Hz and amplitude A. The characteristic frequency of the nonlinear system is $1/2\pi RC \approx 1400$ Hz. Varying the Gaussian noise intensity, we could change the characteristic switching frequency between two states in the system.

Figures 2 and 3 show the noise background, which is the spectral density $S(0)$ of fluctuations at zero frequency, as a function of the dichotomic-noise amplitude for two limiting cases, $w_0 \gg \gamma$ and $w_0 \ll \gamma$, respectively. It is seen that the noise suppression by noise is observed in the latter case.

Figures 4–6 show, respectively, the noise background $S(0)$, the intensity of the first harmonic of the output signal, and the signal-to-noise ratio, which is determined as the ratio of the intensities of the first harmonic and the noise background, as functions of the input signal amplitude A in the adiabatic limit, i.e., when the signal period is much longer than all characteristic times in the nonlinear system, at $\Delta = 0$. It is seen that the total noise is suppressed by the applied signal.

In conclusion, we note that the deviation from the theoretical dependences becomes substantial at high intensities $\Delta > 3$ V of the dichotomic noise and input signal amplitudes $A > 1$ V, when the applicability conditions for the Kramers approximation are violated. Different threshold values of Δ and A are related to dif-

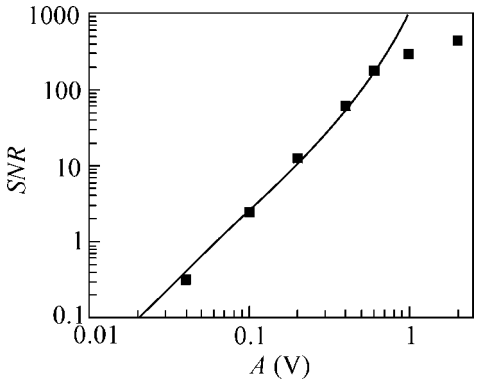

Fig. 6. The signal-to-noise ratio against the amplitude of a rectangular signal with the frequency $\Omega/2\pi = 1$ Hz at $\Delta = 0$. The solid line is Eq. (11) for $n = 1$ and $q = 0$.

ferent asymptotic behaviors with respect to the variables q and v in the first of Eqs. (11).

This work was supported by the Russian Foundation for Basic Research (project no. 99-02-17545), the Russian State Program "Physics of Quantum and Wave Processes" (Subprogram "Statistical Physics," project no. VIII-3), and the Russian State Program "Neutron Investigations of Condensed States."

REFERENCES

1. L. Gammaitoni, P. Hanggi, P. Jung, and F. Marchesoni, Rev. Mod. Phys. **70**, 223 (1998).
2. V. S. Anishchenko, A. V. Neĭman, F. Moss, and L. Shimansky-Geier, Usp. Fiz. Nauk **169**, 7 (1999) [Phys. Usp. **42**, 7 (1999)].
3. A. Neiman, L. Schimansky-Geier, F. Moss, *et al.*, Phys. Rev. E **60**, 284 (1999).
4. R. Rosenfeld, A. Neiman, and L. Schimansky-Geier, Phys. Rev. E **62**, R3031 (2000).
5. J. M. G. Vilar and J. M. Rubi, Phys. Rev. Lett. **86**, 950 (2001).
6. W. Horsthemke and R. Lefever, *Noise-Induced Transitions. Theory and Applications in Physics, Chemistry, and Biology* (Springer-Verlag, Berlin, 1984; Nauka, Moscow, 1987).
7. O. V. Gerashchenko, Zh. Éksp. Teor. Fiz. **116**, 1477 (1999) [JETP **89**, 797 (1999)].
8. O. V. Gerashchenko, S. L. Ginzburg, and M. A. Pustovoit, Eur. Phys. J. B **19**, 101 (2001).

Translated by R. Tyapaev

JETP Letters, Vol. 73, No. 11, 2001, pp. 597–599. Translated from Pis'ma v Zhurnal Éksperimental'noĭ i Teoreticheskoĭ Fiziki, Vol. 73, No. 11, 2001, pp. 677–679.

A Change in the Conductivity of Sodium–Helium Plasma Interacting with Polarization-Modulated Laser Radiation Tuned to Sodium D_1 Line

S. P. Dmitriev, N. A. Dovator*, R. A. Zhitnikov, and V. A. Kartoshkin

Ioffe Physicotechnical Institute, Russian Academy of Sciences, Politekhnicheskaya ul. 26, St. Petersburg, 194021 Russia

** e-mail: nicolai.dovator.@pop.ioffe.rssi.ru*

Received April 13, 2001

A change in the conductivity of a sodium–helium plasma interacting with laser radiation tuned to the sodium $3^2S_{1/2}$– $3^2P_{1/2}$ transition and having sign-changing polarization is experimentally observed. It is shown that this effect is caused by the processes of Penning ionization, spin exchange, and optical orientation of atoms in a gas-discharge plasma. © *2001 MAIK "Nauka/Interperiodica".*

PACS numbers: 52.38.-r; 52.20.Hv

Investigation of the effect of optical orientation of atoms on the electrical conductivity of a gas-discharge plasma is one of the important directions of optovoltaic spectroscopy [1]. Alkali–helium plasma is among the most interesting subjects of investigation in this field. For instance, it was found in [2, 3] that simultaneous optical orientation of alkali-metal atoms (Rb, Na) and metastable triplet helium atoms by two (helium and alkaline) resonance lamps changes the conductivity of alkaline– helium plasma. It was shown that the polarization optovoltaic (POV) effect is due to the fact that the probability of Penning ionization depends on the mutual spin orientation of interacting alkali-metal and helium atoms. It was emphasized in these studies that, when carrying out control experiments, the POV effect disappeared after switching off the helium lamp that provided optical orientation of the He 2^3S_1 atoms.

This work reports the observation of the POV effect caused by laser optical orientation of only alkali-metal atoms in alkali–helium (Na–He) plasma. The POV effect is explained in terms of the multistep action of optical orientation of sodium atoms and a number of simultaneous elastic and inelastic spin-dependent processes on the conductivity of alkali–helium plasma.

The experimental setup is schematically depicted in Fig. 1. A working chamber containing sodium vapor (T = 418 K) and helium gas at a pressure of 0.5–1 torr was placed in the center of Helmholtz coils creating a static magnetic field H_0 = 5 Oe. A high-frequency discharge was initiated in the chamber by a high-frequency generator operating at a frequency of 45 MHz. The gas-discharge chamber was illuminated by the light of a rhodamine-6G tunable dye laser (P_{max} ~ 50 mW) pumped by an argon laser with an output of 4 W. The light beam of the tunable laser was directed along the static magnetic field H_0. Before entering the working chamber, the linearly polarized laser radiation was passed through a quarter-wave plate rotating with frequency $\Omega/2\pi$ = 10 Hz by a mechanical drive. Due to this rotation, the circular polarization of laser radiation changed four times during one revolution of the plate ($\sigma^+ \longrightarrow \sigma^- \longrightarrow \sigma^+ \longrightarrow \sigma^-$). It was established experimentally that, when the laser was tuned to λ = 589.6 nm (sodium D_1 line), the conductivity of alkali–helium

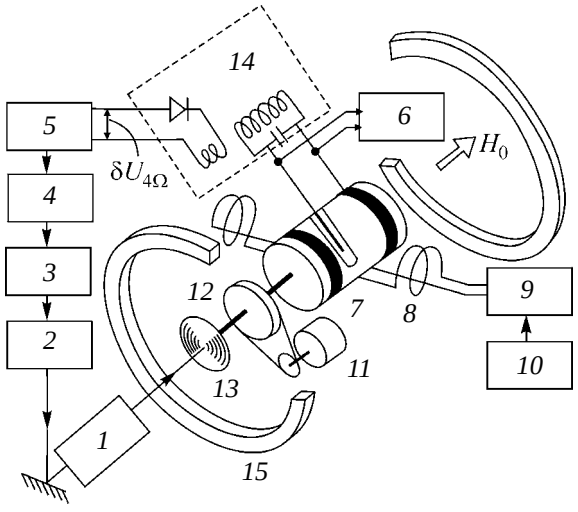

Fig. 1. Block diagram of experimental setup: (*1*) tunable dye laser, (*2*) pumping argon laser, (*3*) recorder, (*4*) amplitude detector, (*5*) narrowband amplifier, (*6*) high-frequency discharge generator, (*7*) working chamber, (*8*) rf coil, (*9*) rf oscillator, (*10*) frequency meter, (*11*) electric motor, (*12*) quarter-wave plate, (*13*) beam expander to a diameter of 6 mm, (*14*) block for recording the high-frequency discharge voltage variations caused by a change in plasma conductivity, and (*15*) Helmholtz coils.

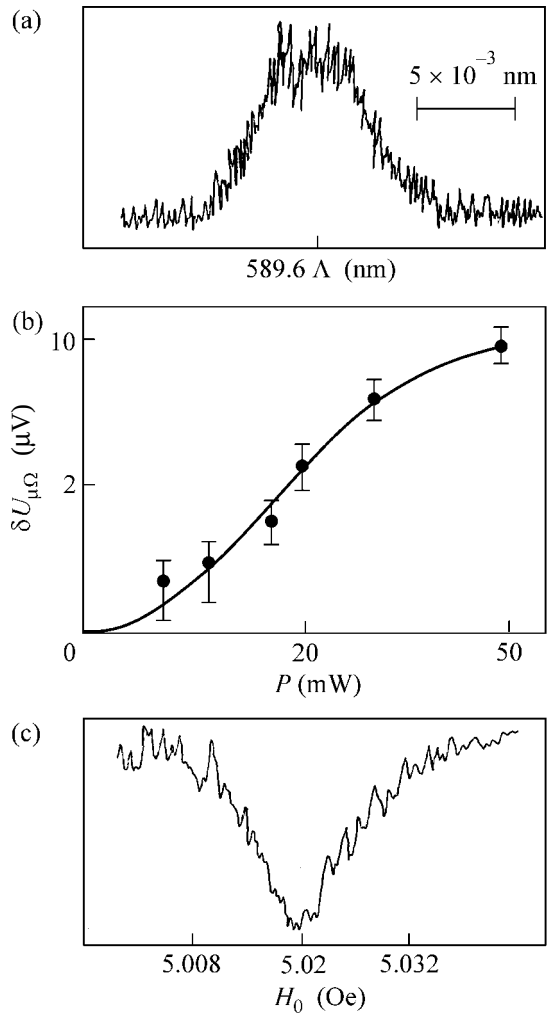

Fig. 2. Experimental results. (a) POV signal amplitude as a function of laser wavelength; (b) POV signal amplitude as a function of laser intensity (tuning to the sodium D_1 line); (c) POV signal amplitude as a function of static magnetic field at a fixed frequency of the rf magnetic field (tuning to the sodium D_1 line).

plasma periodically changed with a frequency of 4Ω ($\delta U_{4\Omega} \sim 10$ μV at the output of block *14*). The $\delta U_{4\Omega}$ signal was amplified by a narrowband amplifier and recorded on an *X*–*Y* recorder after amplitude detection. An example of the POV signal recorded upon scanning the laser wavelength in the range of the D_1 line of the sodium resonance doublet is shown in Fig. 2a. The POV effect was not observed upon scanning the laser wavelength in the vicinity of the sodium D_2 line (λ = 589 nm).

The appearance of a conductivity change signal ($\delta U_{4\Omega}$) caused by the action of a polarization-modulated radiation on the alkali–helium plasma can be explained as follows. The circularly polarized laser radiation (four times during one revolution of the quarter-wave plate) induces sign-changing orientation of sodium atoms which collide with the metastable helium atoms in the discharge and polarize them. The following reactions are responsible for the orientation transfer from the sodium atoms to the helium atoms:[1]

Penning ionization

$$\begin{aligned} &\mathrm{He}(2^3S_1) + \mathrm{Na}(3^2S_{1/2}) \\ &- \mathrm{He}(1^1S_0) + \mathrm{Na}^+(2^1S_0) + e^- \end{aligned} \tag{1}$$

and spin-exchange (see [2–5])

$$\begin{aligned} &\mathrm{He}(2^3S_1)\uparrow + \mathrm{Na}(3^2S_{1/2})\downarrow \\ &- \mathrm{He}(2^3S_1)\downarrow + \mathrm{Na}(3^2S_{1/2})\uparrow \end{aligned} \tag{2}$$

processes.

These processes induce sign-changing orientation of the helium 2^3S_1 atoms in synchronism with the orientation of sodium atoms. Next, after the polarization of the He 2^3S_1 atoms, the Penning ionization of the metastable He atoms in the collisions with each other

$$\begin{aligned} &\mathrm{He}(2^3S_1) + \mathrm{He}(2^3S_1) \\ &- \mathrm{He}(1^1S_0) + \mathrm{He}^+(1^2S_{1/2}) + e^- \end{aligned} \tag{3}$$

and with the Na atoms [again in reaction (1)] results in the periodic variation of the rate constants for reactions (1) and (3). This occurs because, due to the conservation of the total spin of reactants and reaction products, free electrons cannot be produced in reactions (3) and (1) if the colliding atoms are spin-aligned (their spins may be oriented both along and in opposition to the H_0 field; in our experiments, this was dictated by the position of the mica plate determining the sign of circular polarization), and, quite the reverse, reactions (3) and (1) are allowed and the electron population in plasma increases if the atoms are not oriented (this corresponds to the situation when the quarter-wave plate does not change linear polarization of laser radiation in the chamber). Macroscopically, this is manifested by an increase in the plasma conductivity. As a result of these processes, the plasma conductivity must change with a frequency of 4Ω, as was observed in the experiment.

To verify this hypothesis for the origin of the POV signal, it is sufficient to destroy the polarization of helium 2^3S_1 atoms and make sure that the signal disappears. In our experiments, the destruction mechanism was provided by a resonant rf magnetic field saturating the transitions between the components of the helium 2^3S_1 level. Figure 2c shows the experimental dependence of the amplitude of the POV signal (laser was tuned to the sodium D_1 line) for a static magnetic field H_0 scanned in the range of 5 Oe at a fixed frequency

[1] It should be noted that electrons in gas-discharge plasma are spin-polarized due to the spin-exchange collisions with sodium atoms and to reaction (1); they collide with the metastable helium atoms to orient them; i.e., they play the part of an additional mechanism of polarization transfer from the Na atoms to the He atoms.

(14.6 MHz) of the rf field created by an rf oscillator connected to a coil with its axis perpendicular to the axis of Helmholtz coils. One can see from this figure that the POV signal decreases (practically to the noise level in the signal path) at the exact resonance, directly confirming our assumptions about the origin of the observed signal. The fact that at low output P of the dye laser the amplitude of the POV signal depends nonlinearly on laser intensity (see Fig. 2b) is an additional corroboration of this assumption. The point is that the POV signal in our experiments is formed in two steps; helium is first oriented due to the collisions with sodium atoms, after which the oriented helium atoms collide with each other and with the sodium atoms. As a result, the amplitude of the electron-density signal should depend quadratically on the laser intensity at small P values (far from saturation [7]). This also explains why the POV signal is absent when the laser is tuned to the sodium D_2 line. As was shown in [8], the signal due to helium orientation in the collisions with sodium atoms excited at the D_2 line is approximately three times weaker than the signal obtained upon tuning to the D_1 line. Considering the above-mentioned quadratic dependence, the $\delta U_{4\Omega}(D_2)$ signal should be approximately an order of magnitude weaker than the $\delta U_{4\Omega}(D_1)$ signal; i.e., it should be weaker than the noise level ~1.5 μV, which is what is observed in our experiment.

In summary, the conductivity of alkali–helium plasma was found to change upon exposing it to a polarized laser radiation orienting the sodium $3^2S_{1/2}$ atoms. It is shown that this effect is caused by a multistep mechanism including the optical orientation of sodium atoms by laser radiation, the polarization of metastable helium atoms in the collisions with optically oriented sodium atoms, and the spin-dependent Penning ionization due to the interaction of sodium atoms with the metastable triplet helium atoms. The latter process eventually gives rise to the POV effect observed in this work.

REFERENCES

1. V. N. Ochkin, N. G. Preobrazhenskiĭ, and N. Ya. Sharov, *Optogalvanic Effect in Ionized Gas* (Nauka, Moscow, 1991).
2. S. P. Dmitriev, R. A. Zhitnikov, and A. I. Okunevich, Zh. Éksp. Teor. Fiz. **70**, 69 (1976) [Sov. Phys. JETP **43**, 35 (1976)].
3. S. P. Dmitriev, Opt. Spektrosk. **88**, 737 (2000) [Opt. Spectrosc. **88**, 664 (2000)].
4. G. M. Keiser, H. G. Robinson, and C. E. Jonson, Phys. Lett. **51**, 5 (1975).
5. E. V. Blinov, B. I. Ginzburg, V. A. Zhitnikov, *et al.*, Zh. Tekh. Fiz. **54**, 2315 (1984) [Sov. Phys. Tech. Phys. **29**, 1362 (1984)].
6. S. P. Dmitriev and D. É. Denisov, Zh. Tekh. Fiz. **67** (6), 131 (1997) [Tech. Phys. **42**, 704 (1997)].
7. R. J. Knize, Z. Wu, and W. Happer, Adv. At. Mol. Phys. **24**, 223 (1988).
8. S. P. Dmitriev, N. A. Dovator, R. A. Zhitnikov, *et al.*, Zh. Tekh. Fiz. **70** (1), 16 (2000) [Tech. Phys. **45**, 14 (2000)].

Translated by V. Sakun

JETP Letters, Vol. 73, No. 11, 2001, pp. 600–603. Translated from Pis'ma v Zhurnal Éksperimental'noĭ i Teoreticheskoĭ Fiziki, Vol. 73, No. 11, 2001, pp. 680–683.

Density of Quasilocalized States Along the Resonance Curves in Continuum

A. M. Kosevich[1], D. V. Matsokin[2,*], and S. E. Savotchenko[3]

[1] *Verkin Physicotechnical Institute of Low Temperatures, National Academy of Sciences of Ukraine, Kharkov, 61103 Ukraine*

[2] *Kharkov National University, Kharkov, 61077 Ukraine*

* *e-mail: matsokin@univer.kharkov.ua*

[3] *Belgorod State University, Belgorod, 308007 Russia*

Received April 23, 2001

Densities of quasilocalized states are calculated and analyzed for a one-dimensional system with a point defect and an FCC crystal with a planar defect. The density of states displays a pronounced peak that is positioned near the energy (frequency) of resonant transmission of a particle (wave) through the defect but slightly shifted from this energy. The peak nears the resonance frequency and sharpens, tending to a δ function, as the continuum edge is approached. © *2001 MAIK "Nauka/Interperiodica".*

PACS numbers: 63.20.Mt; 61.72.Ji

In recent years, considerable interest has been expressed in the phenomena associated with the interaction of free propagating waves or particles with single-type states localized near the defects. In this respect, the specific features of a multichannel resonance scattering prove to be the subject of discussion [1– 3]. These features are closely related to the properties of quasilocalized states in a continuum [4]. The purpose of this work is to analyze the interconnection between the scattering amplitudes and the spectral density of states in the system of interest. Two examples are taken for the analysis: the interaction of two particles with different dispersion laws in a one-dimensional quantum system and the resonance phonon scattering in an FCC crystal containing a planar defect.

In Section 1, the amplitudes for particle scattering from a point defect are analyzed for a one-dimensional system with two types of elementary excitations that differ in the parameters of quadratic dispersion laws. At certain values of these parameters, the so-called Fano resonances appear in this system (an analogous situation was observed for the electron scattering from an impurity in a 2D quantum channel [2]). The density of quasilocalized states is calculated. It is shown that its maximum is fixed to the resonant transmission energy but slightly shifted from it.

In Section 2, the density of quasilocalized states is analyzed using the model of a planar discrete defect in an FCC crystal with the central nearest-neighbor interactions. The spectra of resonance modes and the in-gap localized states were calculated for this model in [5]. The density of quasilocalized states has a pronounced peak that is slightly shifted from the frequency of resonant transmission of elastic wave through the planar defect. It is shown that, on approaching the continuum edge, the peak comes closer to the resonant frequency and sharpens, tending to a δ function. Beyond the continuum, the resonance curve is continued as a dispersion curve for the in-gap state localized near the defect.

1. Density of states in a 1D system with two dispersion branches. A 1D quantum system with two groups of quasiparticles having quadratic dispersion laws are considered:

$$E = E_1 + \frac{k^2}{2m_1}, \quad E = E_2 + \frac{k^2}{2m_2}, \quad E_1 < E_2, \qquad (1)$$

where Planck's constant $\hbar$ is taken to be unity. If a passive point defect is located at $x = 0$ in this system, the interaction with this defect, according to [3], can be written in the form of the following local potential:

$$H_{\text{int}}(x, x') = U_0\{\alpha_1|\psi_1(0)|^2 + \alpha_2|\psi_2(0)|^2 + \beta[\psi_1^*(0)\psi_2(0) + \psi_2^*(0)\psi_1(0)]\}\delta(x)\delta(x'), \qquad (2)$$

where $\psi_1(x)$ and $\psi_2(x)$ are the wave functions of the particles of the first and second type, respectively.

Let the particle of the first type with energy E ($E_1 < E < E_2$) be incident on the defect from the left. The sec-

ond particle with this energy can only be in the localized state with wave function

$$\psi_2 = Be^{-\kappa|x|}, \quad \kappa = \sqrt{2m_2(E_2 - E)}. \tag{3}$$

It was shown in [3] that the scattered particle can resonantly transmit through the defect at a certain ratio between its energy and interaction parameters. The interaction of a freely propagating particle of the first type with the localized state of the second type is the physical reason for the appearance of a resonance in the transmission through the passive defect. The total transmission occurs at $\alpha_1\kappa = m_2U_0(\beta^2 - \alpha_1\alpha_2)$.

We now intend to show that the energy corresponding to the total defect transparency correlates with the density of stationary quasilocalized states. The point is that in the system of interest quasilocalized states occur in the energy interval $E_1 < E < E_2$ for which the wave function ψ_1 has the form of a standing wave

$$\psi_1(z) = \begin{cases} A\cos(kx - \varphi), & x < 0 \\ A\cos(kx + \varphi), & x > 0, \end{cases} \tag{4}$$

while ψ_2 is localized near the defect, according to Eq. (3).

The spectrum of quasilocalized states is continuous and characterized by a single parameter—phase φ. Making use of the boundary conditions following from the presence of the potential H_{int}, one can easily obtain the relation for the phase φ

$$\tan\varphi = \Delta_r(E)/\Delta_t(E), \tag{5}$$

where

$$\Delta_r(E) = m_1U_0\{m_2U_0(\beta^2 - \alpha_1\alpha_2) - \alpha_1\kappa\},$$

$$\Delta_t(E) = k(\kappa + \alpha_2m_2U_0), \quad k = \sqrt{2m_1(E - E_1)}.$$

The addition to the bulk density of states is given by the formula

$$\delta g(E) = \frac{1}{\pi}\frac{d\varphi(E)}{dE} = \frac{1}{\pi}\frac{\Delta_r'(E)\Delta_t(E) - \Delta_r(E)\Delta_t'(E)}{\Delta_r^2(E) + \Delta_t^2(E)}. \tag{6}$$

Assume that the total transmission occurs in the system [$\Delta_r(E_t) = 0$]. Assume also that the functions $\Delta_r(E)$ and $\Delta_t(E)$ vary smoothly near E_t; i.e., the point $E = E_t$ is positioned far from any spectral singularities (edges of spectral branches, etc.). Then, expanding in powers of $\delta E = E - E_t$ in Eq. (6), one obtains in the leading approximation

$$\delta g(E) = \frac{1}{\pi}\frac{\Gamma}{(\delta E + \Delta_t\Delta_t'/(\Delta_t'^2 + \Delta_r'^2))^2 + \Gamma^2}, \tag{7}$$

where $\Gamma = \Delta_r'\Delta_t/(\Delta_r'^2 + \Delta_t'^2)$, $\Delta_{t,r} \equiv \Delta_{t,r}(E = E_t)$, and $\Delta_{t,r}' \equiv \Delta_{t,r}'(E = E_t)$. This expansion is valid if Δ_t' does not tend to zero; i.e., it is valid except for the cases

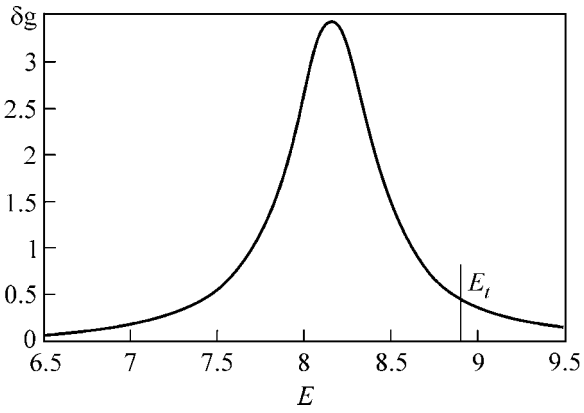

Fig. 1. The addition to the density of states as a function of energy; $U_0 = -0.7$, $m_1 = 1$, $m_2 = 2$, $\alpha_1 = 2$, $\alpha_2 = 2$, $\beta = 1$, $E_1 = 0$, and $E_2 = 10$. E_t is the total transmission energy.

when

$$E^* - E_t \ll E_t - E_1, E_2 - E_t,$$

where

$$E^* = \frac{1}{8}(8E_1 + 8E_2 - \alpha_2^2U_0^2m_2 + [32E_1^2 + 32E_2^2 + 192E_1E_2 + \alpha_2^4U_0^4m_2^2 - 16E_1\alpha_2^2U_0^2m_2)]^{1/2}.$$

One can see that the density of states near the point $E = E_t$ has the form of a Lorentzian peak with width Γ and center shifted from the E_t point by $\Delta_t\Delta_t'/(\Delta_t'^2 + \Delta_r'^2)$ (Fig. 1).

2. Density of states in an FCC crystal with planar defect. Let us consider the dynamics of an FCC crystal with a planar defect coinciding with the (001) plane. The coordinate axes are directed along the cube edges, and the z axis is perpendicular to the defect plane. Only the interactions between the nearest neighbors are considered. Following [5], we assume that the defect is characterized by a change in the force constant between the atoms belonging to the layers $z = 0$ and $z = -1$ (the edge of the unit-cell cube is taken to be 2). The ratio of force constant in the defect layer to the force constant in the pure crystal is denoted by ε.

It was shown in [5] that eigenmodes (including quasilocalized) in this crystal may be of two types, symmetric and antisymmetric. We are interested in the symmetric modes, for which

$$u_x^+(n_z - 1) = -u_x^-(-n_z), \quad u_z^+(n_z - 1) = u_z^-(-n_z),$$

where u_i^+ is the displacement in the upper half-space ($n_z \geq 0$), u_i^- is the displacement in the lower half-space ($n_z < 0$), and n_z numbers the atomic layers along the z axis.

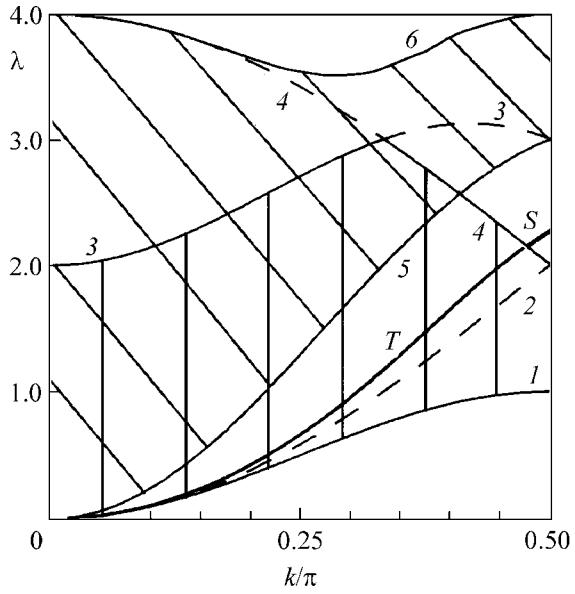

Fig. 2. Dispersion curves for the total transmission frequency T and symmetric vibration S for $\varepsilon = 3$. The vertical dashes correspond to the pseudotransverse branch, and the inclined dashes correspond to the pseudolongitudinal branch. Curve *2*: $\lambda = 2(1 - \cos k)$, $q = 0$; curve *3*: $\lambda = 2 - \cos 2k - \cos k$, $q = \pi$; curve *4*: $\lambda = 2(1 + \cos k)$, $q = \pi$; curve *5*: $\lambda = 2 - \cos 2k + \cos k$, $q = 0$; curves *1* and *6* are the lower and upper spectrum edges, respectively.

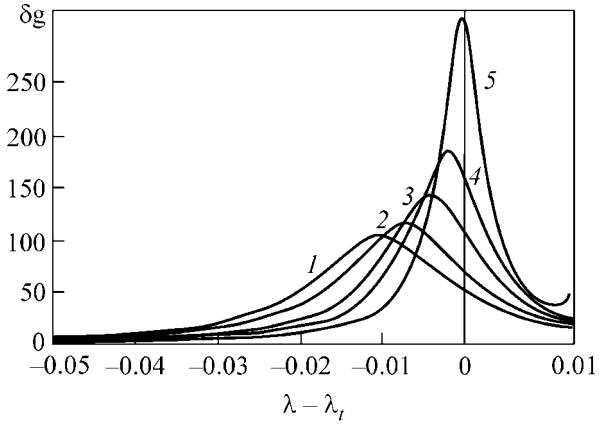

Fig. 3. Density of states as a function of $\lambda - \lambda_t$ for different k along curve T; λ_t corresponds to the total transmission frequency. Curves: (*1*) $k = 84\frac{\pi}{180}$; (*2*) $k = 85\frac{\pi}{180}$; (*3*) $k = 86\frac{\pi}{180}$; (*4*) $k = 86.5\frac{\pi}{180}$; and (*5*) $k = 86.9\frac{\pi}{180}$. $\varepsilon = 3$.

The resonant transmission and reflection take place for the phonons whose frequencies lie within one of the bulk crystal vibration branches but outside of the other branch. In these spectral regions, the quasilocalized eigenmodes may exist; i.e., two-partial modes, one component of which is localized near the defect while the other freely propagates in the crystal.

Let us consider a wave propagating in the [110] direction. This wave has two independent components: lower frequency (pseudotransverse) component, whose spectrum is vertically dashed in Fig. 2, and higher frequency (pseudolongitudinal) component, whose spectrum is shown by the inclined dashes in Fig. 2. In this case, there are three spectral regions where the quasilocalized states may exist (Fig. 2): the first one is bounded by curves *2*, *5*, and *4*; the second one is bounded by the solid section of curve *3* and dashed section of curve *4*; and the third region is bounded by curve *5*, solid section of curve *4*, and dashed section of curve *3*. Curve *T* in the low-frequency region of quasilocalized states corresponds to the total transmission conditions for the pseudotransverse wave through the defect. In the right part of Fig. 2, this curve meets the edge of the gap between the pseudotransverse and pseudolongitudinal frequency branches. Then, it is continued as curve *S* for the in-gap wave localized near the defect.

Let us consider the low-frequency region of quasilocalized modes. The wave displacement vector has the following form at $z \geq 0$:

$$\begin{aligned} u_x^+(x, z) &= (u_t \cos(qz + \varphi) + u_l e^{-\kappa z}) e^{ik(x+y)}, \\ u_z^+(x, z) &= (iu_t \Gamma_t \sin(qz + \varphi) + u_l \Gamma_l e^{-\kappa z}) e^{ik(x+y)}, \end{aligned} \tag{8}$$

where

$$\Gamma_t = -\frac{2 - \cos 2k - \cos k \cos q - \lambda}{\sin k \sin q},$$

$$\Gamma_l = i\frac{2 - \cos 2k - \cos k \cosh \kappa - \lambda}{\sin k \sinh \kappa},$$

$\lambda = m\omega^2/4\gamma$, and γ is the force constant in the crystal volume.

The addition to the unperturbed density of states in this spectral region is

$$\delta g = \frac{1}{\pi}\frac{\partial \varphi}{\partial \lambda}. \tag{9}$$

We will calculate it for the symmetric quasilocalized modes. The explicit formulas for φ and $\delta g(\omega)$ are rather cumbersome, so we only present the results of calculations.

The curve for the density of states at a fixed k shows a peak that is slightly shifted from the resonant transmission frequency to lower frequencies. If we are interested in a change in the density of states with changing wave number k along the total transmission curve T (Fig. 2), then we can see that the peak in the density of states near the point at the bulk spectrum edge, where T matches the curve for the dispersion law S of the in-gap localized modes, approaches the total transmission frequency, sharpens with increasing k, and tends to a δ-like shape at the continuum edge (Fig. 3). It is this state that transforms outside the continuum into the

symmetric mode localized near the defect (Fig. 2, curve *S*).

Thus, it is shown by the examples of a 1D quantum system with two groups of excitations and an FCC crystal with a planar defect that the resonant transmission curves in a continuum show peaks of the density of states. The presence of a sharp peak on the curve for the density of vibrational states indicates that the respective vibrations are sharply set off and have resonant character in the continuum. For an FCC crystal, this means that these vibrations may play the role of so-called "leaky waves."

This work was supported in part by the INTAS-1999, grant no. 167.

REFERENCES

1. A. N. Darynskii and G. A. Maugin, Wave Motion **23**, 363 (1996).
2. Ch. S. Kim and A. M. Satanin, Zh. Éksp. Teor. Fiz. **115**, 211 (1999) [JETP **88**, 118 (1999)].
3. A. M. Kosevich, Zh. Éksp. Teor. Fiz. **115**, 306 (1999) [JETP **88**, 168 (1999)].
4. A. M. Kosevich and S. E. Savotchenko, Fiz. Nizk. Temp. **25**, 737 (1999) [Low Temp. Phys. **25**, 550 (1999)].
5. A. M. Kosevich, D. V. Matsokin, and S. E. Savotchenko, Fiz. Nizk. Temp. **25**, 63 (1999) [Low Temp. Phys. **25**, 48 (1999)].

Translated by V. Sakun

JETP Letters, Vol. 73, No. 11, 2001, pp. 604–608. Translated from Pis'ma v Zhurnal Éksperimental'noĭ i Teoreticheskoĭ Fiziki, Vol. 73, No. 11, 2001, pp. 684–688.

Observation of Fractal Nanoclusters on the Pulsed Laser Deposition of Gold

V. D. Borman, A. V. Zenkevich, M. A. Pushkin, V. N. Tronin, and V. I. Troyan

Moscow State Engineering Physics Institute (Technical University), Moscow, 115409 Russia

Received April 25, 2001

The results of studying the fractal structure of Au clusters arising in pulsed laser deposition under conditions of strong deviations from thermodynamic equilibrium are presented. A mechanism is suggested in which the formation of fractal nanoclusters is considered as a result of the decay of a strongly correlated initial state in a nonequilibrium system of adatoms. The geometrical shape of the fractal structures observed experimentally can be described within the given mechanism, and their dimensionality can be estimated. © *2001 MAIK "Nauka/Interperiodica".*

PACS numbers: 81.16.Mk; 61.43.Hv; 64.60.Ak

At the present time, the ideas of fractal geometry actively penetrate into various fields of modern physics [1, 2]. The fractal nature of the objects under study is revealed in nonequilibrium processes such as the formation of new-phase nuclei. In particular, it has been found that clusters of a metal deposited on a substrate may have a fractal structure even at small deviations from an equilibrium [2].

The growth of fractal micron-size clusters is described by the diffusion-controlled aggregation model [3], cluster–cluster aggregation model, and Eden's ballistic model [2]. Common to these models is the suggestion of the occurrence of a spherical growth nucleus followed by the development of micron-size dendrite structures [2] observed only at a subsequent stage. The existence of such a spherical "seed" is naturally expected at a small deviation from equilibrium within the Zel'dovich–Volmer–Weber model [4]. The idea of the existence of fractal nanometer-size clusters on pulsed laser deposition (PLD) was proposed in [5] in connection with the explanation of the ordering of Au clusters at the NaCl(100) surface.

This work presents the results of an experimental study of the geometrical structure of Au nanoclusters that are formed on the NaCl(100) and HOPG surface under conditions of a strong deviation from thermodynamic equilibrium, which occur during PLD. It was found that nanometer-size clusters (~20 Å) possess a fractal structure. Here, an important distinction from micron-size clusters observed experimentally [2] is the fact that the fractal nature of the nanoclusters obtained in this work disappears as their size increases.

An analysis of characteristic times showed that the formation of fractal nanoclusters is a consequence of the evolution of the nonequilibrium initial state of the system of deposited atoms in a time during which information on the initial states of the system is not completely lost. In such a time, the discrete character of the motion of interacting Brownian particles over the surface becomes principal [6]. The coordinates of these particles at certain values of system parameters (the rate of atom transportation to the surface, the temperature of the substrate, and its symmetry) form sets that possess the properties of the known Julia sets [7]. The boundaries of these sets, which correspond to the perimeters of clusters, have a fractal structure [8]. Hence, the fractal shape of the resulting clusters can be explained, and their dimensionality can be estimated.

Nanometer-scale metal clusters were formed by Au PLD onto NaCl(100) and highly oriented pyrolytic graphite (HOPG) crystals at room temperature under an ultrahigh vacuum ($p \approx 5 \times 10^{-10}$ torr) in the preparation chamber of an XSAM-800 electronic spectrometer. The surface was controlled *in situ* using Auger electron spectroscopy. Radiation from a YAG:Nd^{3+} laser (λ = 1.06 μm) with the energy E = 80–200 mJ in the Q-switched regime (τ = 15 ns) and a pulse repetition frequency of 25 Hz was focused on the Au target. The amount of Au atoms deposited in one pulse was varied within the range 10^{13}–10^{15} atom/cm^2 with the deposition pulse duration $\tau_p \sim 10^{-6}$ s. The total amount of the deposited substance was measured *ex situ* by Rutherford backscattering with He^+ ions. For comparison, experiments were performed on the thermal evaporation (TE) of an equivalent amount of Au onto NaCl(100) and HOPG crystals. The rate of TE deposition was ~10^{14} atom cm^{-2} s^{-1}.

The structure of Au clusters was analyzed by transmission electron microscopy (TEM). The NaCl surface coverage Θ with visible Au clusters ($\Theta = S/S_0$, where S_0 is the total surface area of the substrate and S is the area occupied by gold clusters) for laser deposition was $\Theta_{PLD} \approx 0.1$ at the total amount of the deposited substance $n_{PLD} \approx 1.1 \times 10^{15}$ atom/cm^2. The size distribution of clusters $f(r)$ is shown in Fig. 1, curve *a*. Here, the

0021-3640/01/7311-0604$21.00

average cluster size $\langle r \rangle$ = 15 Å. For TE deposition, the total amount of deposited atoms was $n_{TE} \approx 1.25 \times 10^{15}$ atom/cm^2. The coverage in this case was $\Theta_{TE} \approx 0.06$, and $\langle r \rangle \approx 46$ Å (see Fig. 1, curve *b*). Because TEM is insensitive to 2D objects, the value of *r* should be thought of as the size of the 3D part of islands.

The shape of Au clusters was analyzed based on TEM images. A standard procedure was used for determining the ratio between the area and perimeter of the object under study [9]. TEM images were divided into square cells (pixels), and the area *S* and perimeter *p* were determined in pixels for each cluster within the ranges *r* = 6–60 Å for PLD and *r* = 20–120 Å for TE. The size of one pixel *b* was *b* = 3 Å for PLD and *b* = 10 Å for TE.

In the general case, the ratio between the area and perimeter of a 2D object is represented in the form [9]

$$S = \mu(\nu) p^{\nu}, \quad (1)$$

where ν is the dimensionality of the object, and $\mu(\nu)$ is a coefficient independent of *p*. The dimensionality of the clusters under study can be obtained by constructing the dependence of log(*S*) on log(*p*). In the case of a smooth boundary of the objects under study, $\nu = 2$ ($S \sim p^2$). A noninteger value of parameter ν (fractional dimensionality) may point to the existence of a fractal structure. When using this method of determining the dimensionality, we gave special attention to taking into account spurious effects of treatment associated with the finite pixel size.

Curves of log(*S*) versus log(*p*) for cluster perimeters *p* = 30–75 Å for PLD and *p* = 100–250 Å for TE are given in Fig. 2. Here, $\nu_{PLD} = 1.7 \pm 0.1$ for PLD and $\nu_{TE} = 2.0 \pm 0.1$ for TE. Note that clusters with perimeters $p < 100$ Å ($r < 25$ Å) were not observed in the case of TE. For clusters of a larger size, an increase was observed in index ν, which reached $\nu = 2.0$ at $r \approx 35$ Å for PLD and $r \approx 70$ Å for TE.

Thus, in the case of PLD, the structure of Au clusters with the size $r \approx \langle r \rangle$ observed by TEM has the fractal dimensionality [9] $D_{PLD} = 2/\nu_{PLD} \approx 1.21 \pm 0.07$. In the case of TE, the structure of clusters in the same range of *r* has the dimensionality $D_{TE} = 2/\nu_{TO} \approx 1.05 \pm 0.05$. Hence, it may be suggested that the structure of clusters that are formed in the laser deposition of the metal is close to fractal, in contrast to TE, in which clusters are not fractal. The difference observed in the shape of the Au clusters formed may point to a significant difference between the condensate growth mechanisms for laser and thermal depositions. The fractal structure of the clusters that are formed on the PLD of the metal is revealed only at the initial stages of growth (*r* = 10–20 Å). Clusters of a larger size ($r \geq 35$ Å) have a smooth shape, that is, are not fractal.

The Koch snowflake may serve as a simplest model of a 2D fractal cluster. Figure 3 shows a comparison of TEM images of real Au clusters that are formed in the case of PLD ($r \approx \langle r \rangle$) and a modified Koch snowflake [10] ($D_K \approx 1.21$). The similarity observed between the real and model clusters may serve as an argument in favor of the fact that we deal with physical fractals.

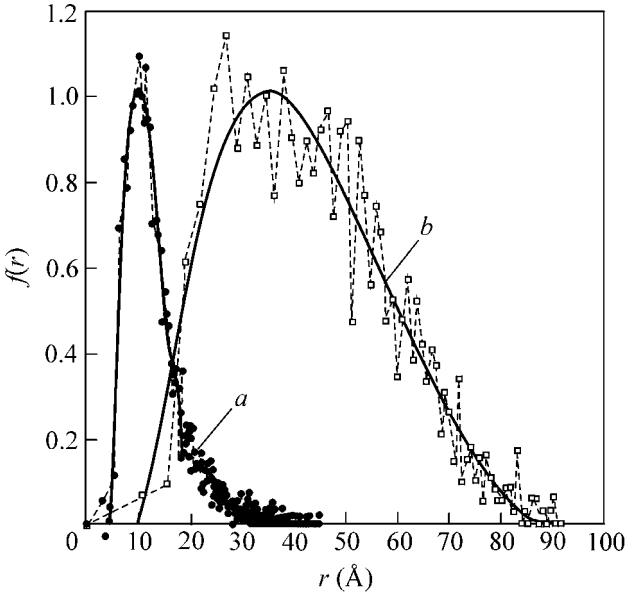

Fig. 1. Size distributions of Au clusters obtained from an analysis of TEM images: (*a*) laser deposition ($\langle r \rangle \approx 15$ Å) and (*b*) thermal evaporation ($\langle r \rangle \approx 46$ Å).

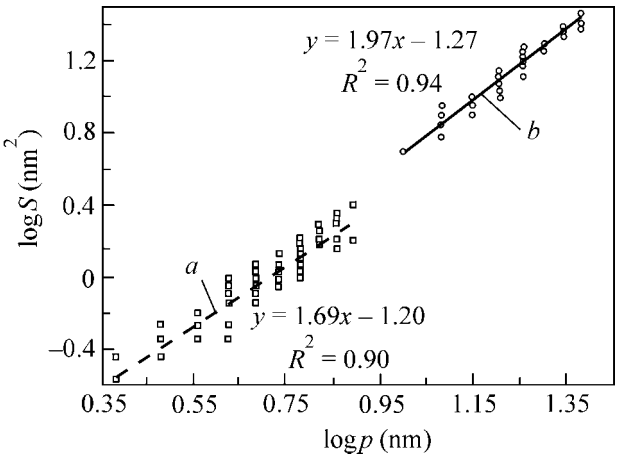

Fig. 2. Ratio between the perimeter *p* and the area *S* of Au clusters on NaCl in (*a*) PLD and (*b*) TE obtained by treatment of TEM images.

In the case of PLD, part of the deposited substance may be accumulated in 2D structures [11]. These structures were studied using scanning tunneling microscopy (STM). An image of the Au clusters obtained by PLD in one laser pulse on the HOPG surface (the total amount of the deposited substance $n_{PLD} \approx 1.3 \times 10^{14}$ atom/cm^2) is shown in Fig. 4. The coverage of the surface with Au clusters was $\Theta_{PLD} \approx 0.1$. The shape of clusters was analyzed by making a cut of the

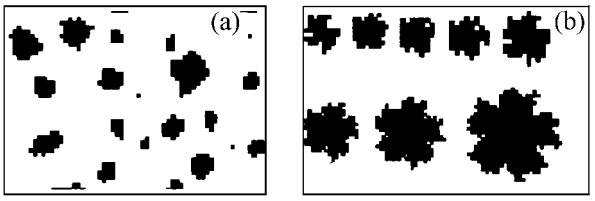

Fig. 3. Comparison of (a) TEM images of real Au clusters on NaCl and (b) model Koch fractals with the dimensionality $D_K \approx 1.21$.

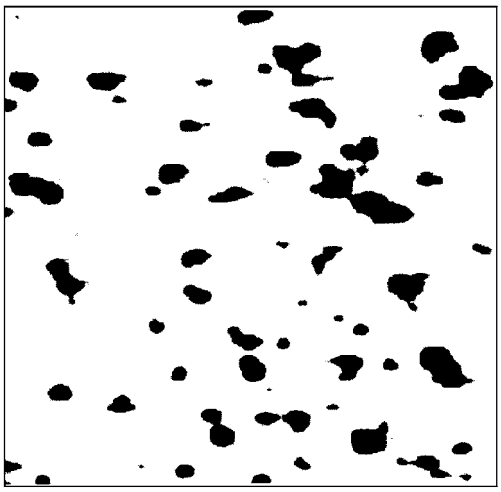

Fig. 4. STM image of Au clusters on HOPG in laser deposition ($N = 1$ pulse, $n_{PLD} \approx 1.3 \times 10^{14}$ atom/cm^2). The image size is 100×100 nm.

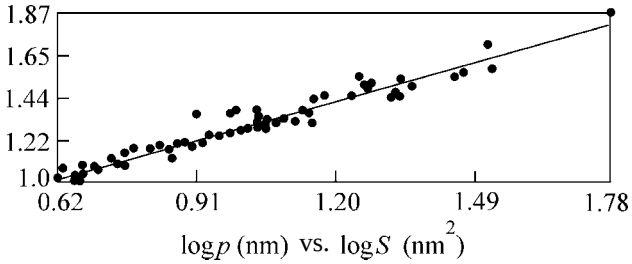

Fig. 5. Ratio between the perimeter p and the area S of Au clusters on HOPG in PLD obtained by treatment of an STM image. The slope of the straight line $\nu \approx 1.50$.

given STM image at a level of one monolayer with respect to the graphite surface. The result of fractal treatment is presented in Fig. 5. The experimental points are approximated by a linear function with the slope $\nu = 1.5 \pm 0.1$, which corresponds to the fractal dimensionality of the clusters under study $D = 1.33 \pm 0.5$. The difference of this value from the value $D = 1.21$ obtained from an analysis of the TEM image of Au clusters in the case of PLD can be explained by the difference in the character of cluster formation: 2D on HOPG [11] and 3D on NaCl [12].

Consider processes proceeding on the surface during atom deposition. Under conditions corresponding to TE with the rate of deposition $j \approx 10^{14}$ cm^{-2} s^{-1}, an adatom has an opportunity to perform $m = \tau_T/\tau_1 \approx 10^4$ elementary jumps during the time of its life at the surface $\tau_T \approx 10^{-4}$ s ($\tau_T = \tau_0 \exp(\varepsilon/T)$, $\tau_0 \approx 10^{-13}$ s, $\varepsilon \approx 0.6$ eV, $T = 300$ K, $\tau_1 \approx a^2/\mathcal{D} \approx 10^{-8}$ s is the time of an elementary jump, $a = 4$ Å is the lattice parameter, and $\mathcal{D} \approx 5 \times 10^{-6}$ cm^2 s^{-1} is the surface diffusion coefficient of Au atoms [12]). When the concentration of adatoms $n_a = j\tau_a$ reaches the value $n_a \geq n_{sat}$ (n_{sat} is the surface density of adatoms in the saturated 2D gas), a condensate forms. The situation described above corresponds to the formation of a new phase by the Zel'dovich–Volmer–Weber mechanism [4].

A special feature of PLD is the high rate of deposition ($j_{PLD}/j_{TE} \approx 10^7$). In this case, the coverage of the surface with atoms $\theta_c \approx 0.2$ that corresponds to the onset of the formation of a fractal cluster (see below) is achieved in the time $\tau_f = n_c/j_{PLD} \approx 10^{-7}$ s $\approx 0.1\tau_p$ ($n_c \approx \theta_c n_0$, $n_0 \approx 7 \times 10^{14}$ cm^{-2} [12]). It is evident that an atom makes $m = \tau_f/\tau_1 \approx 10$ elementary jumps in the time τ_f. In this time, an essentially nonequilibrium system of adatoms interacting both with each other and with an underlayer of adatoms is formed on the surface because of the high rate of its occupation with adatoms. The relaxation of this system is determined by the initial conditions and is performed by the motion of each particle to the state determined by the minimum of its energy (motion to the attractor). The zone of attractor influence is "macroscopic" at $\theta > \theta_c$. Actually, estimates show that the size of a fractal formation at $\theta \approx \theta_c$ is $d_f \approx 10a \approx 4 \times 10^{-7}$ cm, and a cluster containing $N_a \approx d_f^2 n_c \approx 20$ atoms is formed in a time $\tau \approx d_f^2/\mathcal{D} \approx 3 \times 10^{-8}$ s.

Clusters containing $N_a \approx 60$ atoms are formed in the pulse duration time $\tau_p \approx 10^{-6}$ s at the coverage $\theta \approx 0.5$. As θ further increases, the number of particles in a cluster increases when retaining the size and symmetry of clusters (spherization; see Fig. 7 below).

To describe the mechanism of cluster formation, consider the equation of motion of each individual particle at the surface in the self-consistent field approximation

$$\dot{\mathbf{r}} = -\Gamma(\partial U/\partial \mathbf{r}), \qquad (2)$$

where $\mathbf{r}$ is the radius vector of the particle, $\Gamma \sim \mathcal{D}/T$ is the mobility, and $U = U_1 + U_2$ is the potential energy of the particle. The potential energy U is summed up of the self-consistent field energy of all the deposited particles $U_1(n, |\mathbf{r}|)$, which is defined by the number of the nearest neighbors, and the field of the substrate crystal

lattice U_2, which reflects the substrate surface symmetry.

For times $\tau \geq \tau_1$, the motion of a particle over the surface is essentially discrete; therefore, it is necessary to pass to a discrete representation in Eq. (2). Then, Eq. (2) takes the form

$$\mathbf{r}_{k+1} = \mathbf{r}_k - \tau_1 \Gamma \frac{\partial U(\mathbf{r}_k)}{\partial \mathbf{r}_k}. \quad (3)$$

We will represent the self-consistent field of the deposited particles U_1 acting on a given particle as $U_1 \approx Zf(\mathbf{r}_k - \bar{\mathbf{r}})$, where Z is the number of nearest neighbors for the given particle, f is the pair interaction energy of adatoms, and $\bar{\mathbf{r}}$ is the average distance between adatoms.

Equation (3) in the complex representation with allowance for the surface symmetry with respect to the rotation by an angle of $2\pi/q$ [13] takes the form

$$z_{k+1} = Az_k + B(z_k^*)^{q-1}, \quad (4)$$

where $A = 1 - \tau_1 \Gamma (\theta n_0)^{1/2} \left.\frac{\partial U_1}{\partial |z|}\right|_{[\theta n_0]^{-1/2}}$, and B is a constant having the meaning of the bonding energy between the particle and the substrate. It is evident from Eqs. (3) and (4) that the coefficient A can be represented in the form

$$A = 1 - \left(\frac{a}{d_f}\right)^2 \xi, \quad \xi = \frac{\partial U_1/\partial z}{T/d_f}. \quad (5)$$

Here, $\partial U_1/\partial z$ is the force corresponding to the attraction of particles to the attractor, and T/d_f is the amplitude of temperature fluctuations within the size of the fractal cluster.

Equation (4) represents a one-dimensional mapping of the complex plane into itself. It is known [7] that the images of mappings of such kind are fractals in the most general case. The boundary of such domains represents a Julia set [7, 8]. Under certain conditions at the surface ($\theta(j)$, T, q), the atoms located in the domain bounded by a Julia set will move toward the attractor, forming a cluster. The atoms located outside this region will move away from the attractor. Thus, energy domains arise on the surface that are described by Julia sets, and the behavior of each adatom depends on its initial conditions, which corresponds to the initial stages of the evolution of strongly correlated states of the nonequilibrium system. If parameter A in Eq. (4) lies in a certain range of values, connected Julia sets are formed in the system at hand. It is clear from Eq. (5) that the formation of such sets is possible in the case of significant deviations from equilibrium of the system $\frac{\partial U_1}{\partial z} > \frac{T}{d_f}\left(\frac{d_f}{a}\right)^2$. Taking into account a random force in Eq. (2) does not change qualitatively the formation pattern of fractal clusters [14].

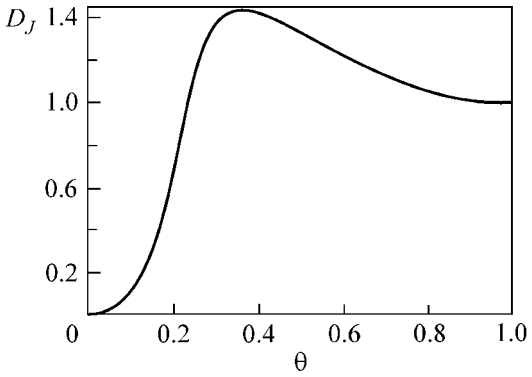

Fig. 6. Dependence of the dimensionality of Julia sets D_J on the coverage θ for one pulse.

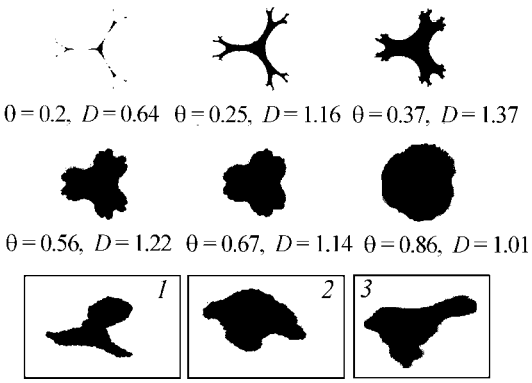

Fig. 7. Sequence of Julia sets for the mapping given by Eq. (4) at some values of θ and (*1*, *2*, *3*) for STM images of individual Au clusters on HOPG.

It is important to note that such energy domains represent true (mathematical) fractals retaining self-similarity in any scale. The structure of a real cluster must repeat to a certain degree the fractal structure of a Julia set. However, because of the finite size of an atom, such an object cannot be a true mathematical fractal.

Suppose that the dimensionality of a physical nanocluster coincides with the dimensionality of the Julia set D_J that has given rise to this cluster. The calculation of the fractal dimensionality of the Julia set for a mapping of the type given by Eq. (4) was carried out numerically with the use of the Schröder renormalization equation [7, 8]. The dependence of D_J on the surface coverage by atoms θ is presented in Fig. 6. The dependence is calculated for the interaction energies of adatoms with each other $\varepsilon_{Au-Au} \approx 0.5$ eV and with the substrate $\varepsilon_{Au-C} \approx 0.4$ eV, $T = 300$ K, and $q = 3$, which corresponds to a system of Au clusters on HOPG.

At small coverage values, $D_J < 1$; that is, the Julia set is disconnected. This means that the clusterization of adatoms does not proceed at such θ on the surface under conditions of fast deposition. With increasing coverage, the dimensionality D_J increases, reaching the

value $D = 1.3$ at $\theta \approx 0.5$, and the structure of the resulting clusters is determined by the structure of the arising energy domains of the corresponding dimensionality. A sequence of Julia sets for a number of values of θ and STM images of individual physical Au clusters on HOPG is given in Fig. 7.

Thus, nanoclusters with a fractal structure, which disappears as the size of nanoclusters increases, were found experimentally under conditions of high deposition rates in gold PLD onto NaCl and HOPG surfaces. A mechanism was proposed that describes the formation of fractal nanoclusters as a result of the evolution of the initial states of a strongly nonequilibrium system of interacting adatoms. It was found that the geometrical structure of the arising nanoclusters essentially depends on the rate of atom transportation to the surface and is determined by the symmetry of the crystal lattice of the substrate surface. The experimental results obtained suggest the existence of a new mechanism of condensed phase formation under conditions of strong deviations from thermodynamic equilibrium. This mechanism is not reduced to the known mechanism of spinodal decay.

The authors are grateful to D.O. Filatov and E. Lægsgaard for help in performing STM measurements.

REFERENCES

1. O. Malcali, D. A. Lidar, and O. Biham, Phys. Rev. E **56**, 2817 (1997).
2. *Fractals in Physics*, Ed. by L. Pietronero and E. Tosatti (North Holland, Amsterdam, 1986; Mir, Moscow, 1988).
3. T. A. Witten and L. M. Sander, Phys. Rev. B **27**, 5863 (1983).
4. E. M. Lifshitz and L. P. Pitaevskiĭ, *Physical Kinetics* (Nauka, Moscow, 1979; Pergamon, Oxford, 1981).
5. V. D. Borman, A. V. Zenkevich, S. Ch. Lai, *et al.*, Pis'ma Zh. Éksp. Teor. Fiz. **72**, 216 (2000) [JETP Lett. **72**, 148 (2000)].
6. A. A. Migdal, Usp. Fiz. Nauk **149**, 1 (1986).
7. J. Milnor, *Dynamics in One Complex Variable* (Friedr. Vieweg & Sohn, Wiesbaden, 1999).
8. H.-O. Peitgen and P. H. Richter, *The Beauty of Fractals: Images of Complex Dynamical Systems* (Springer-Verlag, Berlin, 1986; Mir, Moscow, 1993).
9. J. Feder, *Fractals* (Plenum Press, New York, 1988; Mir, Moscow, 1991).
10. R. M. Crownover, *Introduction to Fractals and Chaos* (Jones and Bartlett, Boston, 1995; Postmarket, Moscow, 2000).
11. T. Endo, T. Sumomogi, H. Maeta, *et al.*, Mater. Trans., JIM **40**, 903 (1999).
12. J. A. Venables and G. D. T. Spiller, in *Surface Mobilities on Solid Materials: Fundamental Concepts and Applications*, Ed. by Vu Thien Binh (Plenum, New York, 1983); NATO ASI Ser., Ser. B **86** (1981).
13. V. I. Arnol'd, *Geometrical Methods in Theory of Ordinary Differential Equations* (Udmurt. Gos. Univ., Izhevsk, 2000).
14. J.-P. Eckmann, Rev. Mod. Phys. **53**, 643 (1981).

Translated by A. Bagatur'yants

JETP Letters, Vol. 73, No. 11, 2001, pp. 609–613. Translated from Pis'ma v Zhurnal Éksperimental'noĭ i Teoreticheskoĭ Fiziki, Vol. 73, No. 11, 2001, pp. 689–693.

Thermal Conductivity of $(La_{0.25}Pr_{0.75})_{0.7}Ca_{0.3}MnO_3$ under Giant Isotope Effect Conditions

A. V. Inyushkin*, A. N. Taldenkov*, O. Yu. Gorbenko, and A. R. Kaul'****

** Institute of Molecular Physics, Russian Research Centre Kurchatov Institute, pl. Akademika Kurchatova 1, Moscow, 123182 Russia*

e-mail: taldenkov@imp.kiae.ru

*** Moscow State University, Moscow, 119899 Russia*

Received April 27, 2001

The thermal conductivity of $(La_{0.25}Pr_{0.75})_{0.7}Ca_{0.3}MnO_3$ manganite has been studied. The isotope substitution of ^{18}O for ^{16}O in this compound leads to a ferromagnetic–antiferromagnetic phase transition at low temperatures. It has been found that the thermal conductivity in the ferromagnetic state is approximately two times higher than in the antiferromagnetic state. It has been shown that the small value of thermal conductivity and its temperature dependence can be due to strong phonon scattering from crystal lattice defects, which are thought of as Jahn–Teller distortions. The parameters of this scattering can be determined within the Debye model of thermal conductivity from a comparison of samples differing in their isotope composition. © *2001 MAIK "Nauka/Interperiodica".*

PACS numbers: 72.15.Eb; 75.30.Kz; 66.70.+f

Perovskite manganites $Ln_{1-y}A_yMnO_3$ (Ln designates a lanthanide; A = Ca, Sr, and others) demonstrate anomalously high sensitivity of physical properties to external factors. This feature of manganites is associated with strong interaction between charge, spin, and orbital degrees of freedom. These compounds exhibit a rich phase diagram with a number of states differing in magnetic and electric properties, which is controlled by the doping level y and by the ratio of ionic radii of the Ln and A cations.

Investigations of the thermal conductivity $\kappa(T)$ of manganites [1–9] revealed the following two general features. Firstly, the thermal conductivity of manganites, both single crystals and ceramics, is very low, $\kappa(300\ \mathrm{K}) \sim 1$–$2\ \mathrm{W\ m^{-1}\ K^{-1}}$ [2], which is close to the minimal theoretical value for the thermal conductivity of solids. Secondly, a transition to the metallic ferromagnetic phase at the temperature T_{FM} is accompanied by an increase in thermal conductivity, and this increase for various compositions may amount to tens and hundreds of percent.

An analysis of experimental data on the thermal conductivity, electrical conductivity, and heat capacity of manganites indicates that phonon thermal conductivity is the dominant mechanism of heat transport. Estimates of the electron [1–6, 7] and magnon [2, 4] thermal conductivity indicate that their contribution is less than 10% of the total value, and hence these mechanisms of heat transport cannot serve as an explanation for the sharp increase in $\kappa(T)$ at $T < T_{FM}$.

The anomalously low thermal conductivity of manganites in a wide temperature range is explained by strong phonon scattering from crystal lattice defects. Along with this scattering, the interaction of phonons with excitations of the spin subsystems can also be observed in the vicinity of T_{FM}. It is known that it can sharply increase in the vicinity of the magnetic phase transition in many magnetic dielectrics, causing a local minimum in the temperature dependence of $\kappa(T)$ near the critical point. A similar behavior of thermal conductivity was observed in some manganites [3, 10, 11]. However, as well as in our case, the dependence $\kappa(T)$ for many manganites exhibits no characteristic dip near T_{FM} [8]. Note that a transition from a paramagnetic phase (PM) to a charge-ordered state (CO), an AFM state, or a dielectric FM state is not accompanied as a rule by considerable changes in $\kappa(T)$. Therefore, we believe that spin–phonon interaction cannot be considered as the main process of phonon relaxation common to all the manganites.

When considering crystal lattice defects as the source of heat resistance, one can distinguish cation disorder in $Ln_{1-y}A_yMnO_3$ solid solutions, grain boundaries (for polycrystalline samples), and also static and dynamic distortions of MnO_6 octahedra due to the Jahn–Teller effect at Mn^{3+} ions. Undoubtedly, cation disorder always makes an additional contribution to phonon scattering, which apparently does not depend on the type of ordering. At the same time, because the thermal conductivity of $LaMnO_3$, which has no cation disorder, is close to the thermal conductivity of doped manganites [2], it may be inferred that this mechanism

is not general and determining. The same can also be said about phonon scattering from grain boundaries with regard to the data obtained with single crystals [1, 2, 6, 7].

Evidently, Jahn–Teller lattice distortions are the defects that determine to a large extent the behavior of the thermal conductivity of manganites over a wide temperature range. It is known that the delocalization of electrons upon transition to a metallic FM state effectively reduces Jahn–Teller distortions, which results in a decrease in the rate of phonon scattering from these defects τ_{JT}^{-1} and can explain the increase in $\kappa(T)$ at $T < T_{FM}$ [1, 2, 4, 5, 7]. In the case of electron-doped manganites, this mechanism must be less effective, because the concentration of Jahn–Teller Mn^{3+} ions is low at low doping levels. Actually, $\kappa(T)$ for $LaMnO_3$ (100% Mn^{3+}) is approximately an order of magnitude smaller than $\kappa(T)$ in $CaMnO_3$ (100% Mn^{4+}), and the thermal conductivity of the latter very strongly decreases upon doping with samarium [7], which increases the concentration of Mn^{3+} ions. In this case, an increase in $\kappa(T)$ of 30% is observed for the $Sm_{0.12}Ca_{0.88}MnO_3$ composition upon transition to the metallic FM state.

In this work, a method is proposed for the quantitative estimation of the intensity of the main process of phonon scattering in manganites. It is based on the giant isotope effect found in the $(La_{0.25}Pr_{0.75})_{0.7}Ca_{0.3}MnO_3$ manganite [12, 13]. The FM transition in this compound at temperatures below 100 K is suppressed if the ^{16}O oxygen isotope is replaced by the heavy ^{18}O isotope. In this case, the temperatures of high-temperature phase transitions $T_{CO} \approx 180$ K and $T_{AFM} \approx 150$ K and the crystal structure parameters found by neutron diffraction [14, 15] change slightly on isotope substitution at $T > T_{FM}$. In addition, according to [14, 15], it is sufficient to enrich a sample with the ^{18}O isotope to 90% in order to decrease the FM phase content of the sample to a level of less than 5%, whereas the FM content of a sample with the natural isotope composition (99.76% ^{16}O, that is, almost the pure ^{16}O isotope) is about 90%. Thus, given two identical samples differing only in isotope composition, one can distinguish and quantitatively investigate the specific process of phonon scattering, which determines the behavior of the thermal conductivity of manganites.

Samples and measurement procedure. In this work, thermal conductivity was measured in ceramic samples of $(La_{0.25}Pr_{0.75})_{0.7}Ca_{0.3}MnO_3$ prepared by solid-phase synthesis. The procedure of preparing samples differing in the oxygen isotope composition and their similar thermal history provided the identity of two samples (hereafter referred to as O16 and O18) in the chemical composition, including the oxygen index, and in the ceramic structure (crystallite size, density, porosity type). The procedure of isotope substitution (isotope exchange of oxygen in the sample with oxygen in the surrounding gas) and the properties of the samples obtained were described in [13, 14]. The ceramics density was about 80% of the theoretical value. The ^{18}O isotope content of the O18 sample was 90 ± 2%. The characteristic dimensions of the samples were $1.5 \times 0.5 \times 0.2$ mm. Such small sizes provide definite advantages in measurements of thermal conductivity, namely, a short thermal relaxation time of the sample and reduced thermal radiation losses at temperatures $T > 100$ K.

Thermal conductivity was measured by the steady-state longitudinal heat flux method. An analysis of measurement errors showed that the relative random error in $\kappa(T)$ was about 3% and the absolute error was 20–30%. The error is due to a large error in determining the geometrical dimensions of the samples and uncertainty in the heat power transfer from the heater to the sample. In order to obtain more accurate data on the absolute value of $\kappa(T)$ for samples differing in isotope composition, we repeated measurements with the same sample before and after isotope exchange, trying to reproduce experimental conditions as accurately as possible. At $T > 120$ K, the values of thermal conductivity for the O16 and O18 samples coincided within 10% of the experimental error, and the normalized values of thermal conductivity $\kappa(T)/\kappa(273\ \mathrm{K})$ differed by less than 2%. In a separate experiment, we determined that the error due to radiation losses was no more than 10% at $T = 273$ K and did not exceed 1% at $T < 100$ K. The absolute value of thermal conductivity $\kappa(273\ \mathrm{K}) \approx 1.7 \pm 0.2\ \mathrm{W\ m^{-1}\ K^{-1}}$.

Results and discussion. Figure 1a shows the temperature dependence of thermal conductivity for the O16 and O18 samples. Throughout the entire temperature range, $\kappa(T)$ was found to be small and close in absolute value to the thermal conductivity of disordered materials. No anomalies were observed in either sample at temperatures of charge T_{CO} and antiferromagnetic T_{AFM} orderings that would be at all significant. The thermal conductivity of the O16 sample sharply increased almost two times upon transition to the ferromagnetic metal state at $T_{FM} \approx 100$ K. In contrast, the temperature dependence $\kappa(T)$ for the O18 sample monotonically increases. The application of a magnetic field of 5 T along the thermal flux direction shifts T_{FM} up by 60 K for the O16 sample, leaving the thermal conductivity unchanged at $T < 50$ K. This behavior indicates that the concentration of the FM phase in the O16 sample is close to saturation. This result agrees with the results of neutron experiments [14, 15].

Estimating the electron thermal conductivity $\kappa_e(T)$ with the use of the Wiedemann–Franz law and experimental data on electric conductivity indicates that $\kappa_e(T) < 0.01\kappa(T)$ in our case; that is, heat transfer by charged carriers is virtually absent. According to [16], the specific heat of manganites with compositions similar to those studied in this work remains almost unchanged

upon transition to the FM state. This indicates that the ferromagnetic ordering of magnetic moments of manganese ions leaves the density of states in the region of thermal energies virtually unchanged and, consequently, renders highly improbable the appearance of heat transport by magnons. In addition, from these data on heat capacity, it also follows that the change in phonon thermal conductivity due to changes in elastic properties and crystal lattice parameters cannot be significant.

The rate of phonon scattering by Jahn–Teller distortions τ_{JT}^{-1} can be estimated using the equation of kinetic theory

$$\kappa = Cv^2\tau/3, \quad (1)$$

where C is the lattice heat capacity, v is the average phonon velocity, $\tau^{-1} = \tau_0^{-1} + \tau_{JT}^{-1}$ is the total rate of phonon relaxation, and τ_0^{-1} is the rate of scattering in all the processes except for the Jahn–Teller ones. Assuming that, at $T < T_{FM}$, $\tau_{JT}^{-1} = 0$ in the O16 sample, we obtain an estimate of the contribution from Jahn–Teller defects (Fig. 1b)

$$\frac{\tau_{JT}^{-1}}{\tau_0^{-1}} = \frac{\kappa_{O18}^{-1}(T)}{\kappa_{O16}^{-1}(T, 5\text{ T})} - 1, \quad (2)$$

and also the temperature dependence $\tau_{JT}^{-1}(T)$ (Fig. 1c)

$$\tau_{JT}^{-1}(T) = (\kappa_{O18}^{-1}(T) - \kappa_{O16}^{-1}(T, 5\text{ T}))Cv^2/3. \quad (3)$$

Here, $\kappa_{O16}(T, 5\text{ T})$ is the thermal conductivity of the O16 sample in a magnetic field of 5 T. The heat capacity $C(T)$ was approximated by a Debye function with the Debye temperature $T_D = 500$ K that was determined from high-temperature data on the heat capacity of manganites of the series $(La_{1-y}Pr_y)_{0.7}Ca_{0.3}MnO_3$ [17]. The velocity $v = 5.0 \times 10^5$ cm s^{-1} was estimated from the value of T_D in agreement with the data given in [18]. Figure 1b makes it evident that the rate of relaxation τ_{JT}^{-1} is effective over a wide temperature range, that is, comprises more than half τ^{-1} in magnitude and weakly depends on the frequency, whereas the phonon mean free path $l_{JT} = \tau_{JT}v$ is close in magnitude to several lattice parameters at $T \approx 100$ K and grows as T^{-2} (Fig. 1c).

We also calculated the temperature dependence of phonon thermal conductivity in the simple Debye approximation

$$\kappa(T) = \frac{k_B}{2\pi^2 v}\left(\frac{k_B}{\hbar}\right)^3 T^3 \int_0^{T_D/T} \frac{x^4 e^x \tau(x, T)}{(e^x - 1)^2} dx, \quad (4)$$

where $x = \hbar\omega/k_BT$, and ω is the phonon frequency. It was found that a good agreement with the experiment can be reached only with the use of three independent

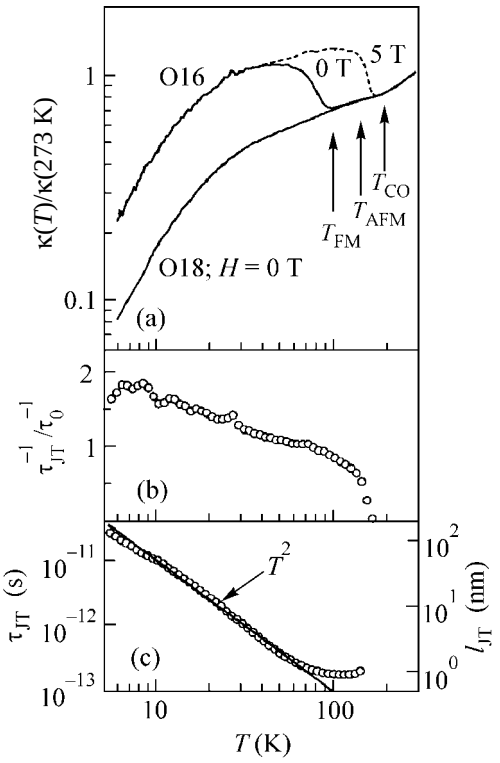

Fig. 1. (a) Normalized thermal conductivity of $(La_{0.25}Pr_{0.75})_{0.7}Ca_{0.3}MnO_3$ with various isotope compositions, (b) ratio of the rate of phonon scattering by Jahn–Teller distortions to the total rate of scattering from all other processes, and (c) $\tau_{JT}(T)$ and $l_{JT}(T)$ as functions of temperature.

relaxation processes: (1) phonon scattering from crystallite boundaries with the rate $\tau_b^{-1} = v/L$, where L is the characteristic size of a crystallite; (2) scattering from extended defects $\tau_d^{-1} = A_d x T$; and (3) scattering from point defects $\tau_{pd}^{-1} = A_{pd} x^4 T^4$. Then,

$$\tau^{-1}(x, T) = \tau_b^{-1} + \tau_d^{-1} + \tau_{pd}^{-1}. \quad (5)$$

The scattering parameters obtained by fitting the theoretical dependence (Eq. (4)) to experimental data are given in the table. Figure 2 demonstrates how $\kappa(T)$ in the O18 sample can be described with consistent allowance made for these processes. The approximately twofold increase in the thermal conductivity of the FM phase is explained by the approximately fivefold decrease in the rate of phonon scattering by extended defects. On the strength of this result, it may be suggested that the frequency dependence τ_{JT}^{-1} is close to a linear function, and Jahn–Teller distortions interact with phonons as extended crystal structure defects. A minor decrease in the intensity of scattering from point defects is also observed. The addition of other scattering processes, for example, from planar defects

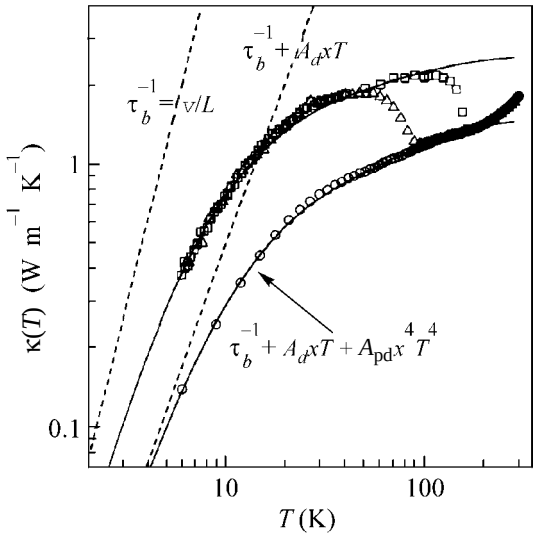

Fig. 2. Temperature dependence of the thermal conductivity of $(La_{0.25}Pr_{0.75})_{0.7}Ca_{0.3}MnO_3$ with various isotope compositions: ○, O18 sample (H = 0 T); △, O16 sample (H = 0 T); and □, O16 sample (H = 5 T). Lines correspond to the results of calculations by the Debye model with the corresponding rates of relaxation.

with rates of the form $\tau_{sf}^{-1} \sim \omega^2$ does not improve the agreement with the experiment, and the process with the scattering rate $\tau_d^{-1} \sim \omega$ remains dominant.

Recently, the thermal conductivity of $La_{1-y}Sr_yMnO_3$ ceramics was studied in [18]. The authors found that the thermal conductivity significantly decreases at $T < T_{AF}$ upon transition from the ferromagnetic conducting composition with $y = 0.48$ ($T_{FM} \approx 290$ K) to the antiferromagnetic insulating composition with $y = 0.50$ ($T_{AF} \approx 160$ K, $T_{FM} \approx 290$ K). An analysis of the data for temperatures from 10 to 90 K carried out within the Debye approximation (Eq. (4)) showed that the feature observed is explained by the 15-fold increase in the rate of scattering $\tau_d^{-1} \sim \omega$. In this case, the other relaxation processes change insignificantly, which is natural with regard to the closeness of the cation composition. These results are close to those obtained in this work under the giant isotope effect conditions. The authors of [18] suggested that the scattering of the form $\tau_d^{-1} \sim \omega$ arises in the AF state mainly because of scattering by tunnel states associated with the motion of oxygen atoms.

Fitting parameters of the phonon scattering rates in the Debye model

Sample	L (μm)	A_d (s^{-1} K^{-1})	A_{pd} (s^{-1} K^{-4})
O16	10	5.0×10^8	3.2×10^3
O18	10	25.0×10^8	4.6×10^3

Phonon scattering by tunneling states determines the behavior of the thermal conductivity of amorphous materials in the low-temperature region ($T \lesssim 1$ K), where $\kappa \sim T^2$, and the rate of resonance scattering takes the following form:

$$\tau_{ts}^{-1} = A_{ts} T x \tanh(x/2), \quad A_{ts} = \frac{k_B}{\hbar} \frac{\pi \tilde{n} \gamma^2}{\rho v^2}, \qquad (6)$$

where $\tilde{n}$ is the subset of tunneling states strongly coupled with phonons, and γ is the average deformation potential. The rate of this phonon scattering depends approximately linearly on the frequency under the condition that the density of tunneling states is constant in the range of thermal energies [19]. At relatively high temperatures ($T \gtrsim 10$ K), the scattering by tunneling states makes an insignificant contribution to the total relaxation of phonons in glasses [20]. Using the value of the fitting parameter A_{ts} found in [18] and Eq. (6), we obtain that the parameter of coupling between thermal phonons and tunneling states in $La_{0.50}Sr_{0.50}MnO_3$ is $\tilde{n}\gamma^2 \approx 90 \times 10^8$ erg cm^{-3}, which is approximately two orders of magnitude higher than the characteristic values for a wide range of amorphous materials [21]. On the strength of this result, we believe that the use of scattering by tunneling states as the source of the linear frequency dependence of phonon scattering in manganites is poorly justified.

The linear dependence of the rate of phonon scattering arises apparently from the interaction of phonons with extended lattice defects in manganites. It is possible that there is spatial correlation among local Jahn–Teller distortions of MnO_6 octahedra. This correlation creates extended deformation fields in the lattice similar to deformation fields around dislocation lines. The lengths of such formations must be considerably larger than the wavelength of thermal phonons, and, according to our estimates, some of them can extend over hundreds of unit cells.

Note in conclusion that this work reports the first investigations of the thermal conductivity in the $(La_{0.25}Pr_{0.75})_{0.7}Ca_{0.3}MnO_3$ manganite, which exhibits the giant oxygen isotope effect in the metal–dielectric transition. It is found that the transition to the ferromagnetic metallic state is accompanied by a growth of thermal conductivity. An analysis of experimental data carried out within the simple Debye model leads to the conclusion that the frequency dependence of the leading term in the relaxation rate of thermal phonons in manganites is close to linear. Jahn–Teller distortions of the crystal lattice are apparently the source of this decay.

The authors are grateful to N.A. Babushkina and N.M. Plakida for useful discussions and valuable comments.

This work was partially supported by INTAS, project no. 97-11954; the Netherlands Organization for Scientific Research, NWO project no. 047-008-017;

and the Russian Foundation for Basic Research, project no. 01-02-16240.

REFERENCES

1. D. W. Visser, A. P. Ramirez, and M. A. Subramanian, Phys. Rev. Lett. **78**, 3947 (1997).
2. J. L. Cohn, J. J. Neumeier, C. P. Popoviciu, *et al.*, Phys. Rev. B **56**, R8495 (1997).
3. B. Chen, A. G. Rojo, C. Uher, *et al.*, Phys. Rev. B **55**, 15471 (1997).
4. J. Hejtmánek, Z. Jirák, S. Krupička, *et al.*, J. Appl. Phys. **81**, 4975 (1997).
5. J. Hejtmánek, Z. Jirák, Z. Arnold, *et al.*, J. Appl. Phys. **83**, 7204 (1998).
6. S. Uhlenbruck, B. Büchner, R. Gross, *et al.*, Phys. Rev. B **57**, R5571 (1998).
7. J. Hejtmánek, Z. Jirák, M. Maryško, *et al.*, Phys. Rev. B **60**, 14057 (1999).
8. K. H. Kim, M. Uehara, C. Hess, *et al.*, Phys. Rev. Lett. **84**, 2961 (2000).
9. K. H. Kim, M. Uehara, and S-W. Cheong, Phys. Rev. B **62**, R11945 (2000).
10. M. Ikebe, H. Fujishiro, and Y. Konno, J. Phys. Soc. Jpn. **67**, 1083 (1998).
11. M. Ikebe, H. Fujishiro, and S. Sugawara, Physica B (Amsterdam) **281–282**, 496 (2000).
12. N. A. Babushkina, L. M. Belova, O. Yu. Gorbenko, *et al.*, Nature **391**, 159 (1998).
13. N. A. Babushkina, L. M. Belova, V. I. Ozhogin, *et al.*, J. Appl. Phys. **83**, 7369 (1998).
14. A. M. Balagurov, V. Yu. Pomjakushin, D. V. Sheptyakov, *et al.*, Phys. Rev. B **60**, 383 (1999).
15. A. M. Balagurov, V. Yu. Pomjakushin, D. V. Sheptyakov, *et al.*, Eur. Phys. J. B **19**, 215 (2001).
16. V. Kiryukhin, B. G. Kim, V. Podzorov, *et al.*, Phys. Rev. B **63**, 024420 (2001).
17. S. N. Mudretsova, A. F. Maĭorova, A. A. Bosak, *et al.*, Zh. Fiz. Khim. **74**, 1765 (2000).
18. M. Ikebe, H. Fujishiro, S. Kanoh, and T. Mikami, Phys. Status Solidi B **225**, 135 (2001).
19. *Amorphous Solids: Low-Temperature Properties*, Ed. by W. A. Phillips (Springer-Verlag, Berlin, 1981).
20. D. P. Jones and W. A. Fillips, Phys. Rev. B **27**, 3891 (1983).
21. J. E. Graebner, B. Golding, and L. C. Allen, Phys. Rev. B **34**, 5696 (1986).

Translated by A. Bagatur'yants

JETP Letters, Vol. 73, No. 11, 2001, pp. 614–616. Translated from Pis'ma v Zhurnal Éksperimental'noĭ i Teoreticheskoĭ Fiziki, Vol. 73, No. 11, 2001, pp. 694–697.

Anomalous Behavior of Linear and Nonlinear Longitudinal Susceptibilities below T_c in a Weakly Anisotropic $CdCr_2Se_4$ Ferromagnet

I. D. Luzyanin* and V. P. Khavronin

Konstantinov Institute of Nuclear Physics, Russian Academy of Sciences, Gatchina, Leningrad region, 188300 Russia

**e-mail: luzyanin@mail.pnpi.spb.ru*

Received February 5, 2001; in final form, April 27, 2001

Frequency dependences of the linear and nonlinear longitudinal dynamic susceptibilities of an almost isotropic cubic $CdCr_2Se_4$ ferromagnet were studied experimentally in the ordered phase. It was found that at frequencies above the two-magnon creation threshold the linear susceptibility decreases as $\chi_1 \propto \omega^{-0.28}$ with increasing frequency and the nonlinear susceptibility decreases as $\chi_n \propto \omega^{-0.73}$, irrespective of n, where n is an odd number. The observed susceptibility anomalies are due to the dipolar forces that violate the conservation of total spin.

PACS numbers: 75.30.Cr; 75.40.Gb

It is well known that a uniform alternating magnetic field is not absorbed in a Heisenberg ferromagnet because the operator for the total spin of the system commutes with the exchange Hamiltonian. Weak relativistic interactions (anisotropy, dipolar forces, etc.) violate spin conservation and provide homogeneous relaxation.

The homogeneous longitudinal susceptibility in the presence of dipolar forces was studied theoretically in [1] within the framework of the linear spin-wave theory (LSWT). According to [1], at nonzero temperatures this susceptibility displays zero-field infrared divergence (IRD) of the type $\chi(\omega \longrightarrow 0) \propto iT/\omega$ at frequencies above the threshold that is determined by the internal magnetic field and anisotropy. It should be noted that this problem was explored earlier in [2], where the influence of dipolar forces on the spin-wave spectrum was modeled by introducing a gap. It turned out that $\chi \propto \omega^{-3/2}$. This result is different from the one obtained in [1], where the exact expression was used for the spectrum.

The above-mentioned IRD is due to the specific "weak" violation of spin conservation by the dipolar forces, as a result of which the number of excitations (magnons) can change in the elementary scattering event, although the magnon spectrum remains gapless if the anisotropy and internal magnetic field are ignored.

Notice that the divergence of susceptibility, obtained in [1], would lead to the nonzero absorption coefficient at $\omega = 0$ and, hence, to the heating of the sample in a static external magnetic field, which, clearly, should not be the case.

Another example of a magnetic Bose system with weak law violation—Heisenberg antiferromagnet—was studied theoretically in [3] also within the framework of the LSWT. The total spin is conserved in the antiferromagnet, but the conservation law is absent in the staggered channel. The corresponding elementary excitation spectrum (antiferromagnons) is also gapless. As was shown in [3], the resulting staggered longitudinal susceptibility also displays an analogous IRD.

Thus, it follows from the cited works that the longitudinal susceptibilities demonstrate anomalous low-frequency behavior in the magnetic Bose systems with weak law violations (nonconservation of the number of excitations in the elementary events in the systems with gapless spectrum of these excitations).

To verify the theoretical predictions for magnetic Bose systems and answer the question of what the consequences are of the IRD for the magnetic dynamics of such systems, we earlier undertook experimental investigation of the homogeneous longitudinal susceptibility of an almost isotropic cubic $CdCr_2Se_4$ ferromagnet ($T_c \approx 128$ K) in the magnetically ordered phase [4]. Experiments were carried out in weak external fields (no higher than 100 mOe) in the low-frequency range ($\omega/2\pi = f \sim 10^2$–$10^6$ Hz). To minimize the demagnetization effect, a sample was shaped like a ring with sizes $\varnothing 5.4 \times \varnothing 2.0 \times 2.1$ mm. The ring plane coincided with the crystal [111] plane. The axially symmetric static (H) and alternating ($h_0 \cos 2\pi f_0 t$) fields were applied in the ring plane so that the field lines were closed and the

field was almost completely concentrated inside the sample. This strongly suppressed the domain formation and allowed us to observe an exceedingly narrow hysteresis with the coercive force $H_c \approx 5$ mOe. To avoid the influence of domains, the experiments were conducted under condition $H, h_0 > H_c$.

The main result of that work consisted in the qualitative confirmation of the theoretical predictions about the anomalous longitudinal dynamics due to the dipolar forces in isotropic Heisenberg ferromagnets. At frequencies above the frequency $\omega_{cr} \approx 2g\mu_B H$ (μ_B is the Bohr magneton, and g is the g factor) corresponding to the creation of two magnons, the longitudinal susceptibility was found to be a less singular function of frequency than in [1] but still divergent in the low-frequency limit, $\chi(\omega \longrightarrow 0) \propto (i/\omega)^{\rho}$. Specifically, $\mathrm{Re}\chi \equiv \chi' \propto |\omega|^{-\rho}\cos(\pi\rho/2)$ and $\mathrm{Im}\chi \equiv \chi'' \propto |\omega|^{-\rho}\sin(\pi\rho/2)$; the ratio $\mathrm{Im}\chi/\mathrm{Re}\chi = \tan(\pi\rho/2)$ was independent of frequency and $\rho \approx 0.28$. The power law dependence of χ on ω was observed in the temperature range from 80 to 120 K, where the exponent ρ changed by no more than 10% (above 120 K, the frequency behavior of the susceptibility was influenced by critical fluctuations). It is noteworthy that in the frequency range studied the imaginary part of susceptibility is on the order of its real part, and this is a nontrivial fact. One can see in Fig. 1, taken from [4], that such a behavior of susceptibility takes place over a wide frequency range. This result gives evidence that the strong interaction of spin waves screens the infrared divergence of the i/ω type obtained in [1]. The departure from this law at $\omega < \omega_{cr}$ (decrease in χ'' and a very weak increase in χ' at $\omega \longrightarrow 0$) is due to the magnetic anisotropy, which is very small in our case.

Every strongly interacting system should be nonlinear. This consideration has stimulated our experimental studies of higher harmonics. It is natural to assume that the power law frequency behavior will be observed for the higher order susceptibilities as well, at least at frequencies above the energy threshold for the creation of two magnons. To verify this assumption, the corresponding experiments were performed with the same single-crystal sample of $CdCr_2Se_4$ as in [4].

The frequency f_0 of an alternating field was varied from 1 to 200 kHz. The harmonics were measured by a serial spectrum analyzer in the range 1–600 kHz. The amplitudes $A_n \propto nf_0(\chi_n'^2 + \chi_n''^2)^{1/2} \propto |\chi_n|$ ($n = 1, 3, 5, \ldots$) of higher harmonics were measured relative to the amplitude of the first harmonic measured at the fundamental frequency f_0, $A_1 \propto f_0(\chi'^2 + \chi''^2)^{1/2} \propto |\chi_1|$, where χ_n' and χ_n'' are, respectively, the real and the imaginary parts of the nth-order susceptibility. The observation of harmonics was mainly limited, apart from the instrumental sensitivity, owing to the following reasons. It will be seen below that the amplitudes of higher harmonics decrease at $\omega_0 \gtrsim 2g\mu_B h_0$ rather rapidly with increasing harmonic number; to take this into account, small amplitudes of the alternating field $h_0 < 40$ mOe should be used in the range of frequencies f_0 chosen. For this reason, the results of this work are mainly related to the third and fifth harmonics. Measurements were made at $T = 82$ K. The results presented below were obtained in zero static magnetic field, $H = 0$ (evidently, only odd harmonics occur in this case), and in the frequency range where the linear longitudinal susceptibility [$\chi'(f_0)$ and $\chi''(f_0)$] displayed power law behavior in [4], i.e., under the condition $\omega_0 \gtrsim 2g\mu_B h_0$.

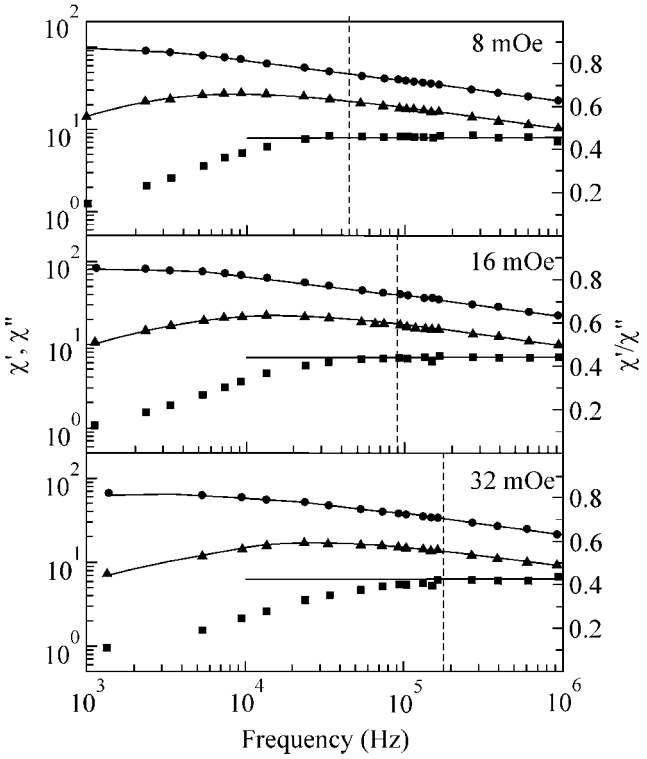

Fig. 1. Frequency dependence of (circles) real and (triangles) imaginary parts of linear longitudinal susceptibility and (squares) of their ratio at different values of the applied static magnetic field. The vertical dashed lines correspond to the two-magnon threshold $2g\mu_B H/h$, $h_0 = 12$ mOe, $T = 82$ K.

It follows from the results obtained that, if this condition is met, then, at a fixed frequency f_0 of the alternating field, the ratio $R_n = |\chi_n|/|\chi_1|$ shows power law dependence on the harmonic frequency nf_0 (or, what is the same, on the harmonic number n), $R_n \propto (nf_0)^{-r} \propto n^{-r}$. Some of these dependences are presented in Fig. 2 for $n = 3$, 5, and 7 by the solid lines. It follows from the analysis of the R_n vs. n curves that the exponent r is, generally, a linear function of frequency and can approximately be represented as $r \approx 5.50(\pm 0.05) + 0.004f_0$ (kHz). The constant term is obtained by the extrapolation of $r(f_0)$ to $f_0 = 0$. Note that at lower frequencies ($\omega_0 < 2g\mu_B h_0$) the R_n dependence on n did not

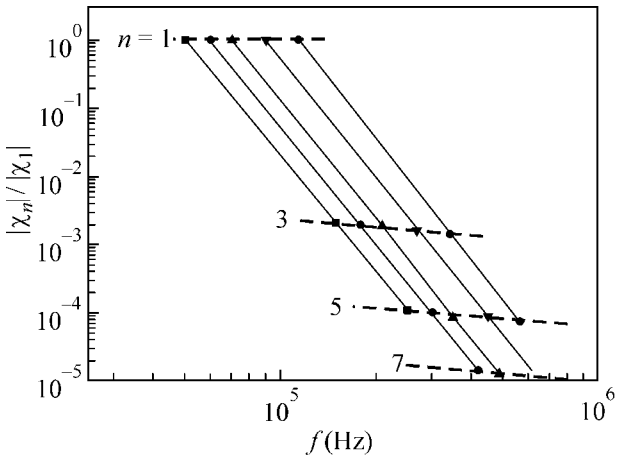

Fig. 2. Plots of $R_n = |\chi_n|/|\chi_1|$ dependences (solid lines) on frequency nf_0 for different frequencies f_0 of the alternating field. The dashed lines connecting R_n values at fixed n demonstrate power law dependence of the harmonic amplitudes on the frequency of the alternating field. For the methodological reasons indicated in the text, the data for $n = 7$ are obtained only at frequencies 60 and 70 kHz; $h_0 = 8$ mOe.

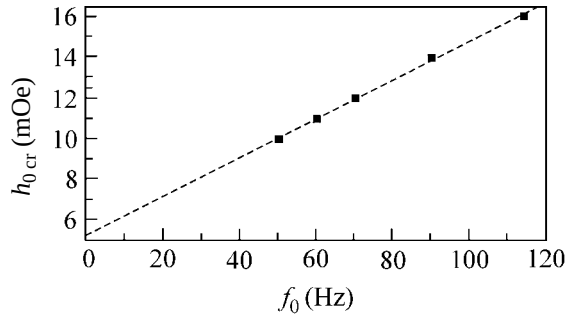

Fig. 3. Frequency dependence of the threshold amplitude h_{0cr} of the alternating field above which the power law is no longer valid for the decrease of higher harmonic amplitudes with increasing harmonic number.

fit a power law, but the behavior of higher harmonics was not examined in detail in this work.

As to the dependence of R_n on f_0 at fixed values n = 3 and 5 (dashed lines in Fig. 2), one can easily see that both harmonics also show power law dependence: $R_n \propto (nf_0)^{-0.45 \pm 0.03} \propto f_0^{-0.45 \pm 0.03}$. The data obtained for $n = 7$ at two frequencies and presented in Fig. 2, generally, do not contradict this dependence. One can suppose that the power law dependence of R_n on f_0 will hold for the higher harmonics as well. On the other hand, it was found from the linear response measurements that $\chi_1 \propto f_0^{-0.28}$. It follows herefrom that at $\omega_0 \gtrsim 2g\mu_B h_0$ the higher order susceptibilities $\chi_n \propto \chi_1^{-\rho} f_0^{-0.45} \propto f_0^{-0.73}$, regardless of n. This result was also obtained in independent measurements of only the third harmonic amplitude as a function of alternating field in the range $50 \le f_0 \le 200$ kHz.

It was pointed out above that $|\chi_n|/|\chi_1|$ shows a power law dependence on n at $\omega_0 \gtrsim 2g\mu_B h_0$. Evidently, this condition breaks at field amplitudes $h_0 > h_{0cr} = \omega_0/2g\mu_B$, and, hence, the indicated dependence may differ from a power law. To determine the value of h_{0cr}, $|\chi_n|/|\chi_1|$ was measured as a function of n by changing field amplitude h_0 at a fixed frequency. Indeed, it turned out that the power law dependence of $|\chi_n|/|\chi_1|$ on n disappeared at a fixed value of h_0. This amplitude of the alternating field was taken as h_{0cr}. The resulting $h_{0cr}(f_0)$ dependence is shown in Fig. 3, from which it follows that, as in the case of linear susceptibility, h_{0cr} corresponds to the two-magnon threshold; i.e., $2g\mu_B h_{0cr} = \omega_0$. The extrapolation of h_{0cr} to $f_0 = 0$ gives a value of approximately 5 mOe for h_{0cr}, which corresponds to the coercive force found in [4] from the hysteresis curves for both $\chi(H)$ and $A_2(H)$.

The experimentally observed scaling behavior of the linear and nonlinear longitudinal susceptibilities gives evidence for the presence of the developed dynamical fluctuations in the system and indicates that it is close to the instability outside the critical region below T_c. This leads to the following important statement: the dipolar forces in an ideal infinite isotropic ferromagnet without anisotropy make the magnetically ordered ground state unstable in zero field because of the increasing homogeneous dynamical fluctuations of longitudinal susceptibility. The long-range magnetic order in such a system is stabilized only by the finite-size and anisotropy effects and also by the external field.

We thank S.V. Maleyev and A.G. Yashenkin for assistance in setting up the problem and for the discussion of experimental results and to Ya.V. Greshneva for taking part in the experiment and data processing. This work was supported by the Russian Foundation for Basic Research (project no. 00-02-16729) and the State Program "Physics of Quantum and Wave Processes," subprogram "Statistical Physics" (project no. VIII-3).

REFERENCES

1. B. P. Toperverg and A. G. Yashenkin, Phys. Rev. B **48**, 16505 (1993).
2. M. I. Kaganov and V. M. Tsukernik, Zh. Éksp. Teor. Fiz. **37**, 823 (1959) [Sov. Phys. JETP **10**, 587 (1959)].
3. S. Braune and S. V. Maleyev, Z. Phys. B **81**, 69 (1990).
4. I. D. Luzyanin, A. G. Yashenkin, S. V. Maleyev, *et al.*, Phys. Rev. B **60**, R734 (1999).

Translated by V. Sakun

JETP Letters, Vol. 73, No. 11, 2001, pp. 617–620. Translated from Pis'ma v Zhurnal Éksperimental'noĭ i Teoreticheskoĭ Fiziki, Vol. 73, No. 11, 2001, pp. 698–701.

Effects of Virtual Transitions in a High-Frequency Field on Electron Transport in Triple-Barrier Structures

A. B. Pashkovskiĭ

State Research and Production Enterprise Istok, Fryazino, Moscow region, 141120 Russia

Received March 26, 2001; in final form, May 4, 2001

High-frequency conductivity has been calculated for triple-barrier nanostructures at resonance diagonal transitions. It is shown that the neglect of transitions to side nonresonance quasi-levels in a high-frequency electric field leads in some cases to an overestimation of the maximum conductivity by 60%, an increase in the line width of more than 40%, and an increase in the integral conductivity by a factor of almost 2.5. In these cases, the transmission coefficient calculated with allowance made for side satellites is approximately 0.6 rather than 1.

PACS numbers: 72.10.-d; 73.22.-f

Theoretical studies of electron transport through resonance levels of a triple-barrier structure in a high-frequency electric field commonly employ a two-level approximation, that is, the representation of the electron wave function in the form $\psi(x, t) = b_K(t)\psi_K(x)e^{-i\omega_K t} + b_L(t)\psi_L(x)e^{-i\omega_L t}$, where L and K are the numbers of the energy levels between which the transitions take place. The wave function components with frequencies that fall outside the vicinity of ω_L and ω_K are rejected as "nonresonance" ones. In the case of diagonal transitions, this approximation is substantiated (from somewhat abstract assumptions) by the fact (see, for example, [1, 2]) that, firstly, transitions to the energy regions $\hbar\omega_K + n\hbar\omega$ and $\hbar\omega_L - n\hbar\omega$ (where $\omega = \omega_K - \omega_L$ is the frequency of the perturbing field and n are natural numbers; see Fig. 1) are nonresonance ones and, hence, weak; and, secondly, the escape of electrons from the structure via these quasi-levels is small.

A question arises of whether radiationless (in fact) transitions (because virtually no electrons leave the structure via the $\hbar\omega_K + n\hbar\omega$ and $\hbar\omega_L - n\hbar\omega$ quasi-levels, each upward transition corresponds to a downward transition, and, in principle, one may speak about virtual transitions) inside a structure can affect observable properties of the structure such as the transmission coefficient, the high-frequency conductivity, or the width of the interaction line. This question is of principal physical and, possibly, essential practical interest. If they can, prospects are opened up for studying (and, possibly, using) a number of analogous phenomena such as states dynamically coupled in a high-frequency field [3]. If not, the description of diagonal transitions is significantly simplified, because the two-level approximation appears to be sufficient in the majority of cases. The aim of this work is to answer this question.

It seems necessary to make two general comments. First, the use of the resonance two-level approximation in a structure with impenetrable outer barriers is well substantiated [4, 5], naturally, until the perturbing field frequency is sufficiently close to the separation between levels. However, the energy spectrum of a structure with a finite penetrability of the barriers becomes continuous, and the electron wave function under steady-state conditions (on a time scale larger than the tunneling electron lifetime in the structure) may significantly differ from the electron wave function in a closed structure and contain components with frequencies $\omega_K + n\omega$ and $\omega_L - n\omega$. It will be shown below that, in contrast to the case of a closed structure, transitions between these components and the levels with energies of $\hbar\omega_K$ and $\hbar\omega_L$ can be comparable with transitions between the resonance components $\hbar\omega_K$ and $\hbar\omega_L$.

Results of numerical calculations. Consider a simplest asymmetric triple-barrier structure with thin (δ-shaped) barriers. Let a uniform high-frequency (HF) electric field is applied across the structure, and let this field varies with time according to the equation $F\cos\omega t = E(e^{i\omega t} + e^{-i\omega t})$, $F = 2E$. Assume for definiteness sake that a monoenergetic electron stream is incident from the left on the resonance level with the number K of the first double-barrier structure, and that the frequency of the HF field corresponds to transitions to the level L of the second double-barrier structure (see Fig. 1). Then, the nonstationary Schrödinger equation takes the form

$$i\hbar\frac{\partial\psi}{\partial t} = -\frac{\hbar^2}{2m^*}\frac{\partial^2\psi}{\partial x^2} + H(x)\psi + H(x, t)\psi,$$

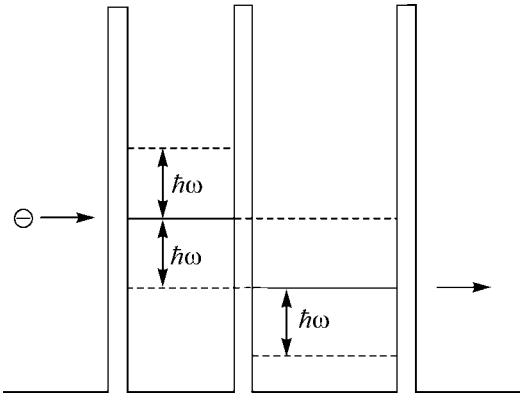

Fig. 1. Schematic representation of a band diagram for a triple-barrier structure.

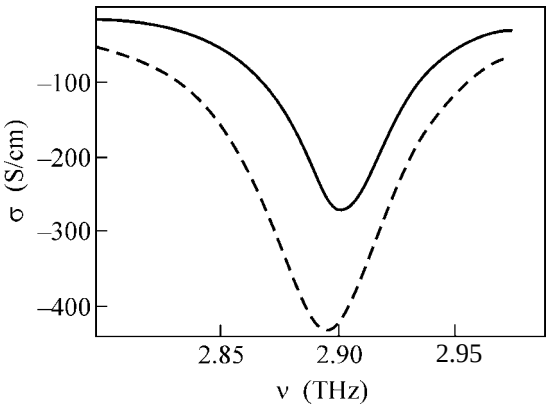

Fig. 2. Frequency dependence of the active conductivity for an InAs triple-barrier structure: the solid and dashed lines correspond to calculations in the four-level and two-level approximations, respectively; the width of the first well is 150 Å, the width of the second well is 165 Å, the height of the barriers is 2 eV, and the thickness of the barriers is 33 Å.

$$H(x) = \alpha\delta(x) + \alpha\rho\delta(x-a) + \alpha\gamma\delta(x-a-l),$$
$$H(x,t) = -qE[x(\theta(x) - \theta(x-a-l)) + (a+l)\theta(x-a-l)](e^{i\omega t} + e^{-i\omega t}). \quad (1)$$

Here, q and m^* are the electron charge and mass, $\alpha = \varphi_b b$ is the power of the first barrier, φ_b and b are its height and width, $\theta(x)$ is the unit function, γ and ρ are numerical coefficients, and a and l are the distances between the barriers.

In order to obtain a partial answer to the question of the effect of virtual transitions on the observable properties of triple-barrier structures, let us solve Eq. (1) numerically by the procedure described in detail in [3, 6] within the two-level and four-level approximation (estimates similar to those given in [6] and below indicate that taking into account four levels is quite sufficient for describing the properties of the system in the most interesting case when the transmission coefficient for the structure in Fig. 1 is a maximum). The calculations show that the effect of side satellites strongly depends on the structure parameters and the HF field amplitude (usually, the greater the ω/ω_0 ratio and the smaller the amplitude, the smaller this effect). Consider a rather typical example when the effect of radiationless transitions can be significant. Figure 2 demonstrates the dependence of the high-frequency conductivity of a triple-barrier InAs structure on the electric field frequency. It is evident that the neglect of transitions to side satellites leads to an overestimation of the maximum conductivity by 60% and an increase in the line width of more than 40%. In this case, the integral conductivity is overestimated by a factor of almost 2.5, and, in addition, the maximal transmission coefficient calculated with allowance made for side satellites is approximately 0.6 rather than 1 (see Fig. 3). It should be noted that escape via side satellites (which, though being small, always takes place in structures with a finite barrier width) is more than an order of magnitude smaller than the escape of electrons from the main resonance levels. Thus, a conclusion can be made that virtual transitions can notably affect observable properties of quantum nanostructures.

Qualitative estimates. The results obtained can be qualitatively explained using the second-order perturbation correction to the ground-state wave function. For the given structure, the unperturbed wave function of electrons ψ_0 with a plane wave of a unit amplitude incident from the left takes the form

$$\psi_0(x) = \begin{cases} \exp(ikx) + D_0\exp(-ikx), & x < 0 \\ A_0\sin(kx) + B_0\cos(kx), & 0 < x < a \\ Z_0\sin(k(x-a)) + W_0\cos(k(x-a)), & a < x < a+l \\ C_0\exp(ik(x-a-l)), & x > a+l, \end{cases} \quad (2)$$

where ε is the energy of electrons incident on the structure, and $k = (2m^*\varepsilon/\hbar^2)^{1/2}$ is the wave vector of electrons.

The resonance parameter in the problems on structures with thin barriers is represented by the quantity [7]

$$y = 2m^*\alpha/\hbar^2, \quad (3)$$

which has the dimensionality of the wave vector. For sufficiently powerful barriers ($y \gg k$; only in this case is it meaningful to speak about a two-level system at all),

$$D_0 = 1, \quad B_0 = 2, \quad A_0 = \frac{2y}{k},$$
$$W_0 = \frac{2}{\rho}, \quad Z_0 = \frac{2\cot(kl)}{\rho}, \quad C_0 = \frac{2k}{\gamma\rho y\sin kl}. \quad (4)$$

Within the small-signal approximation, the first-order correction ψ_1 to the ground-state wave function has the

following time dependence [3]: $\psi_1 = \psi_+(x)e^{-i(\omega_0+\omega)t} + \psi_-(x)e^{-i(\omega_0-\omega)t}$, which corresponds to the emission and absorption of a photon with the energy $\hbar\omega$. In the specific case of a triple-barrier structure, $\psi_\pm$ can be presented in the form

$$\psi_\pm(x) = \begin{cases} D_\pm \exp(-ik_\pm x), & x < 0 \\ A_\pm \sin(k_\pm x) + B_\pm \cos(k_\pm x) + \varphi_\pm(x), & 0 < x < a \\ Z_\pm \sin(k_\pm(x-a)) + W_\pm \cos(k_\pm(x-a)) + \chi_\pm(x), & a < x < a+l \\ C_\pm \exp(ik_\pm(x-a-l)) + P_\pm \exp(ik(x-a-l)), & x > a+l, \end{cases} \quad (5)$$

where

$$k_\pm = (2m^*(\varepsilon \pm \hbar m)/\hbar^2)^{1/2}, \quad P_\pm = \mp\frac{qEa}{\hbar\omega}C_0,$$

and

$$\varphi_\pm, \chi_\pm = \mp\frac{qEa}{\hbar\omega}\psi_0(x) + \frac{qE}{m^*\omega^2}\psi_0'(x)$$

are particular solutions of the equations for $\psi_\pm$ (see [3, 8]). Solving the corresponding system of equations for determining the unknown coefficients, which follows from the continuity conditions, gives

$$A_- \sim B_- \sim W_- \sim C_- \sim y, \quad Z_- \sim y^2, \quad D_- \sim y^0. \quad (6)$$

For nonresonance transitions (in the given case, to an upper nonresonance quasi-level),

$$A_+ \sim B_+ \sim y, \quad D_+ \sim W_+ \sim Z_+ \sim y^0, \quad C_+ \sim y^{-1}. \quad (7)$$

It is evident that it is sufficient to take into account only two resonance levels in the first and second wells in calculations of the small-signal conductivity of the system ($C_- \sim y$, and D_+ does not contain the large parameter y). However, it is necessary to note immediately an important detail: the coefficients A_- and B_-, which correspond to resonance transitions, are of the same order of smallness with respect to the large parameter y as the coefficients A_+ and B_+ of the first-order correction to the wave function corresponding to nonresonance transitions. From here, it follows that the second-order correction to the ground-state wave function due to transitions to the resonance level and back (denote this correction as ψ_{2-}) will have the same order of smallness as the second-order correction due to transitions to a nonresonance quasi-level (denote this correction as ψ_{2+}). Actually, it can be shown that the second-order corrections to the resonance coefficient A in the first well (in fact, it is this coefficient that determines the solution of the problem) take the form

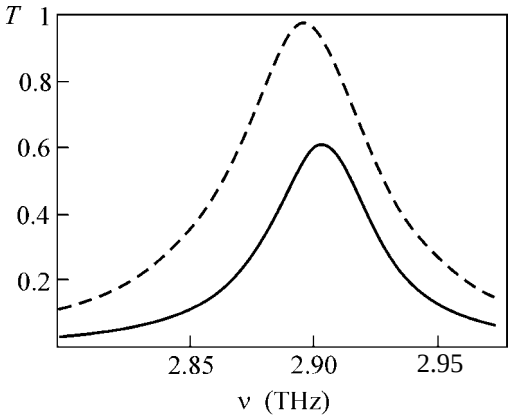

Fig. 3. Frequency dependence of the transmission coefficient of electrons through an InAs triple-barrier structure: the solid and dashed lines correspond to calculations in the four-level and two-level approximations, respectively; the parameters of the structure are the same as in Fig. 2.

$$A_{2+} = \left(\frac{qE}{m^*\omega^2}\right)^2 y^3 f_+(a, \omega, \omega_0),$$
$$A_{2-} = \left(\frac{qE}{m^*\omega^2}\right)^2 y^3 f_-(a, l, \rho, \gamma, \omega, \omega_0), \quad (8)$$

where $f_+(a, \omega, \omega_0)$ and $f_-(a, l, \rho, \gamma, \omega, \omega_0)$ are sufficiently simple but rather cumbersome functions of the arguments given in parentheses. It is interesting to note that the second-order correction from upward–downward transitions depends only on the parameters of the first well, whereas the second-order correction from downward–upward transitions depends on all the parameters of the triple-barrier structure. It is evident that

$$A_{2-} \sim A_{2+} \sim y^3. \quad (9)$$

Analogously, it can also be shown for the resonance level in the second well that the third-order corrections to the resonance coefficient Z from both the resonance level in the first well Z_{3++} and the nonresonance quasi-level in the second well that lies below the resonance one Z_{3--} are of the same order of smallness with respect to the resonance parameter y

$$Z_{3--} \sim Z_{3++} \sim y^5. \quad (10)$$

In this case, it makes absolutely no difference whether this nonresonance quasi-level lies above or below the conduction-band bottom [3].

It is natural that this regularity is also generalized to the corrections of higher orders. The calculations performed allows one to imagine the following qualitative pattern of diagonal transitions in triple-barrier structures. An electron does not pass directly from the resonance level of the first well to the resonance level of the

second well but initially makes a transition to the nonresonance quasi-level of the first well (or from the nonresonance level to the resonance level of the second well). Then, the electron passes to the resonance level of the second well and escapes from the structure via this level. In other words, the transition matrix element consists of a sum of products of the resonance part of the wave function of one level into the nonresonance part of the other one related to the same well. It can be said that the transitions in the first well are made from the resonance level to the nonresonance region of the continuous spectrum. Therefore, the components of the electron wave function that correspond to this region are comparable with those corresponding to the upper level (A_- and B_- are of the same order of smallness as A_+ and B_+). It is clear that the number of electrons tunneling from the lower quasi-level of the first well through the resonance level of the second well is much greater than the number of electrons directly tunneling from the upper quasi-level ($|C_-| \gg |D_+|$). However, the transitions to the lower or upper nonresonance quasi-level make a comparable contribution to the redistribution of electrons over the levels. Analogous arguments are also applicable to the resonance level of the second well.

In other words, when an electron lands on a level in the first well, it has three possibilities. It can emit or absorb a photon and pass onto the lower quasi-level (with the energy of the resonance level in the second well), or pass onto the quasi-level above the resonance level, or simply pass nonradiatively to the second well. An electron that passed onto the upper quasi-level (or another electron from this level) must absorb a photon and pass back onto the resonance level in the first well (there is no escape from the well from this level). An electron that passed onto the lower quasi-level can either absorb a photon and return to the previous state or pass onto the resonance level in the second well. In this case, for an electron that returned from above to the resonance level, the probability that it will pass down rather than escape back from the structure may well be quite different (which is confirmed by the calculation) from the similar probability for an electron that simply came onto the level from the outside. Thus, it is shown that the distribution of electrons over the levels in a HF electric field of a finite amplitude in triple-barrier structures and hence, in general, in multiple-barrier structures with barriers of finite thickness and electron pumping qualitatively differs at $t \longrightarrow \infty$ from the case of closed structures and depends essentially on quasi-energetic satellites. From this main result, it follows, in particular, that the two-level representation of diagonal transitions is applicable only within the small-signal approximation. At the same time, this representation is also widely used in the case of finite amplitude, which turns out to be incorrect. In order that the distribution of electrons over the two levels of a triple-barrier structure be correctly determined, it is necessary to take into account two more satellites separated by $\hbar\omega$ from the resonance levels of the structure.

This work was supported by the Russian Foundation for Basic Research, project no. 00-02-17119, and by the Scientific Council on the Program "Physics of Solid-State Nanostructures," project no. 97-1094.

REFERENCES

1. V. F. Elesin, V. V. Kapaev, Yu. V. Kopaev, and A. V. Tsukanov, Pis'ma Zh. Éksp. Teor. Fiz. **66**, 709 (1997) [JETP Lett. **66**, 742 (1997)].
2. M. Yu. Sumetskiĭ and M. L. Fel'tshin, Pis'ma Zh. Éksp. Teor. Fiz. **53**, 24 (1991) [JETP Lett. **53**, 24 (1991)].
3. A. B. Pashkovskiĭ, Zh. Éksp. Teor. Fiz. **109**, 1779 (1996) [JETP **82**, 959 (1996)].
4. N. B. Delone and V. P. Kraĭnov, in *Atom in a Strong Light Field* (Énergoatomizdat, Moscow, 1984), p. 48.
5. L. D. Landau and E. M. Lifshitz, *Course of Theoretical Physics*, Vol. 3: *Quantum Mechanics: Non-Relativistic Theory* (Nauka, Moscow, 1989, 4th ed.; Pergamon, New York, 1977, 3rd ed.).
6. E. I. Golant and A. B. Pashkovskiĭ, Teor. Mat. Fiz. **120**, 332 (1999).
7. V. M. Galitskiĭ, B. M. Karnakov, and V. I. Kogan, in *Problems on Quantum Mechanics* (Nauka, Moscow, 1981), p. 172.
8. E. I. Golant and A. B. Pashkovskiĭ, Pis'ma Zh. Éksp. Teor. Fiz. **67**, 372 (1998) [JETP Lett. **67**, 394 (1998)].

Translated by A. Bagatur'yants

JETP Letters, Vol. 73, No. 11, 2001, pp. 621–625. Translated from Pis'ma v Zhurnal Éksperimental'noĭ i Teoreticheskoĭ Fiziki, Vol. 73, No. 11, 2001, pp. 702–707.

Electrical Conductivity and Magnetic Susceptibility of Titanium Monoxide

A. A. Valeeva*, A. A. Rempel', and A. I. Gusev

Institute of Solid-State Chemistry, Ural Division, Russian Academy of Sciences, ul. Pervomaĭskaya 91, Yekaterinburg, 620219 Russia

** e-mail: gusev@ihim.uran.ru and/or valeeva@ihim.uran.ru*

Received May 7, 2001

Conductivity and magnetic susceptibility of disordered cubic titanium monoxide TiO_y ($0.920 \le y \le 1.262$) are studied. Temperature dependences of the conductivity of TiO_y monoxides with $y \le 1.069$ are described by the Bloch–Grüneisen function with Debye temperature 400–480 K, and temperature dependences of the susceptibility include Pauli paramagnetism of conduction electrons. The behavior of conductivity and susceptibility of TiO_y with $y \ge 1.087$ is typical of semiconductors with nondegenerate charge carriers obeying Boltzmann statistics. The band gap ΔE between the valence and conduction bands of TiO_y ($y \ge 1.087$) is 0.06–0.17 eV, and effective mass of charge carriers is equal to 7–14 electron masses. © *2001 MAIK "Nauka/Interperiodica".*

PACS numbers: 72.80.Ga; 75.20.-g

Titanium monoxide TiO_y with the cubic ($B1$-type) basis structure is a unique compound having no analogies. TiO_y monoxide has a broad homogeneity region from $TiO_{0.70}$ to $TiO_{1.25}$ and simultaneously contains 10–15 at. % structural vacancies in both titanium and oxygen sublattices. The real structure of titanium monoxide can be represented if its composition is written with allowance made for the contents of structural vacancies in each of the sublattices, i.e., as $Ti_xO_z \equiv TiO_y$ or $Ti_x\blacksquare_{1-x}O_z\square_{1-z} \equiv TiO_y$, where $y = z/x$ and $\square$ and $\blacksquare$ are the structural vacancies in the oxygen and titanium sublattices, respectively. Even the $TiO_{1.00}$ monoxide with formal stoichiometric composition contains 16.7 at. % vacancies in the titanium and oxygen sublattices, so that its real composition is $\sim Ti_{0.833}O_{0.833}$.

The properties of TiO_y are rather poorly known. The reasons are as follows. TiO_y monoxide is hard to synthesize because its composition is unstable even at 700–800 K and it can undergo disproportionation into Ti_2O ($TiO_{0.50}$) or Ti_3O_2 ($TiO_{0.67}$) and cubic oxide or into cubic oxide and Ti_2O_3 ($TiO_{1.50}$) or other phases of the homologous series Ti_nO_{2n-1} (n is an integer from 2 to 10) even under controlled partial oxygen pressure. At temperatures of ~700, ~1000, and ~1100 K, TiO_y undergoes phase transitions accompanied by the formation of various superstructures. Only four of them are well documented [1, 2]. The type and symmetry of superstructures depend on the real starting composition of titanium monoxide. When synthesized by the usual methods, TiO_y samples almost always have two-phase composition and contain a disordered and ordered phase simultaneously. To synthesize a single-phase disordered samples, one should use a special quenching procedure. Temperature measurements of the kinetic and magnetic properties of TiO_y, made in 1960–1970s, showed that the chemical and phase compositions of the samples changed in the course of measurement. This caused a contradiction between the results of different authors. For example, the temperature coefficient $d\rho/dT$ of resistivity ρ of a disordered TiO_y monoxide with $y \approx 1$ was positive in [3–5] and negative in [6]. Among the results coinciding in the cited studies is the negative sign of the thermal electromotive force and the Hall coefficient of TiO_y monoxides with $y > 0.85$ [3–6].

The unreliability and contradictory character of the experimental data have motivated numerous studies devoted to calculating the electronic structure of TiO_y. However, the results of calculations, including the *ab initio* ones, are also contradictory. According to [7–11], there is a wide gap (of several eV) between the O($2p$) and Ti($3d$) bands in the electronic spectrum of cubic titanium monoxide. The authors of [11] suggest that vacancies give rise to the local electron-density peaks (vacancy peaks) in the p–d gap; this is in agreement with the results of calculations [12, 13] suggesting that the vacancy states occur in the energy gaps lying lower than the Fermi level of TiO_y. The presence of a ~2-eV gap in a hypothetical defectless $TiO_{1.0}$ monoxide was confirmed by the authors of [14], although, according to their calculations, the vacancy states are situated only near the bottom of the conduction band and do not eliminate the p–d gap. According to calculations [15], the O($2p$) and Ti($3d$) bands in a defectless TiO monoxide are separated by a gap of width of about 1.8 eV, whereas in the ordered monoclinic Ti_5O_5 monoxide the band gap is equal to 1.2 eV. The presence of

an energy gap was confirmed by the experimental studies of X-ray emission spectra [14, 16], bremsstrahlung and UV emission spectra [14], and optical conductivity [17] of a disordered TiO_y monoxide.

According to the results of another series of computational studies [18–20], the *p–d* gap is absent in the electronic spectrum of TiO_y. The theoretical conclusions about the absence of the *p–d* gap were confirmed by the experimental studies of X-ray emission spectra of TiO_y monoxide with different oxygen content [21] and by the results of studying the X-ray photoelectron and emission spectra [22] of a monoclinic ordered Ti_5O_5 monoxide and a defectless cubic $TiO_{1.0}$ monoxide obtained under high pressure.

Therefore, the available experimental and theoretical data are contradictory, and it is still unclear whether the titanium monoxide is a metal or a semiconductor.

This work reports the experimental results on electrical conductivity (resistivity) and magnetic susceptibility of TiO_y monoxide in the whole homogeneity region of cubic phase.

Samples of nonstoichiometric cubic titanium monoxide TiO_y with different oxygen content ($0.920 \le y \le 1.262$) were synthesized by solid-state sintering of powder mixtures of metallic titanium Ti and titanium dioxide TiO_2 in a vacuum of 0.0013 Pa at a temperature of 1770 K for 70 h with intermediate grinding of the sintering products every 20 h. The diffraction studies were carried out with a Cu$K\alpha_{1,2}$ radiation on a Siemens D-500 or STADI-P (STOE) autodiffractometer. To achieve a disordered state, the synthesized samples were annealed for 3 h at a temperature of 1330 K in quartz ampules evacuated to a residual pressure of 0.0001 Pa; then, the ampules with samples were thrown in water; the quenching rate was ~200 K s^{-1}. The X-ray patterns of quenched samples showed reflections corresponding only to the cubic disordered phase of TiO_y with the *B*1 structure (samples with $y \ge 1.112$) or to the monoclinic ordered Ti_5O_5 [23] phase (samples with $y \le 1.087$). The oxygen content in the quenched TiO_y samples proved to be larger than expected based on the composition of starting mixture. This indicated that the samples were partially depleted of titanium and enriched with oxygen in the course of synthesis and annealing.

The resistivity ρ was measured by a four-probe method in the range 77–300 K. The resistivities of $TiO_{1.262}$, $TiO_{1.087}$, and $TiO_{0.920}$ were also measured at 4.2 K. To provide close electrical contact, an In–Ga paste was applied to the contact area of the samples.

The magnetic susceptibility χ of TiO_y ($0.920 \le y \le 1.262$) was measured over the temperature range from 4 to 400 K in magnetic fields of 8.8, 25, 30, and 50 kOe on an MPMS-XL-5 (SQUID) magnetometer. The susceptibilities of $TiO_{0.946}$, $TiO_{1.069}$, $TiO_{1.087}$, and $TiO_{1.262}$ were additionally measured at temperatures from 300 K to the temperature of onset of the disorder $\longleftrightarrow$ order transition (about 1000 K) by the Faraday method on a pendulum magnetic balance of the Domenicali type.

The chemical and phase compositions of the samples were controlled before and after the measurements.

The magnetization measurements in fields up to 50 kOe at temperatures of 4, 130, and 300 K showed that the TiO_y samples did not have residual magnetization and did not contain any ferromagnetic impurities.

The temperature dependences of resistivity $\rho(T)$ are shown in Fig. 1 for TiO_y of different compositions. In the temperature range studied, the resistivity ρ increases on going from $TiO_{0.920}$ to $TiO_{1.262}$.

The resistivities of $TiO_{1.069}$, $TiO_{0.985}$, $TiO_{0.946}$, and $TiO_{0.920}$ oxides increase with temperature, but the temperature coefficients of resistivity are small. In materials with electronic conduction, the temperature dependence of mean free time $\bar{\tau}$ due to scattering by phonons is described well at $T < 300$ K by the semiempirical Bloch–Grüneisen function

$$\frac{1}{\bar{\tau}} = \frac{4\pi\lambda k_B\theta_D}{\hbar}\left(\frac{2T}{\theta_D}\right)^5 \int_0^{\theta_D/2T} \frac{x^5 dx}{\sinh^2 x}, \qquad (1)$$

where λ is the electron–phonon coupling constant and θ_D is the Debye temperature. Since the resistivity is $\rho = m/ne^2\bar{\tau}$, its temperature dependence can be represented as

$$\rho(T) = \rho(0) + \frac{4\pi m\lambda k_B\theta_D}{ne^2\hbar}\left(\frac{2T}{\theta_D}\right)^5 \int_0^{\theta_D/2T} \frac{x^5 dx}{\sinh^2 x}$$

$$\equiv \rho(0) + \frac{4\pi m\lambda k_B\theta_D}{ne^2\hbar}\left(\frac{2T}{\theta_D}\right)^5 \qquad (2)$$

$$\times\left[-\left(\frac{\theta_D}{2T}\right)^5 \coth\left(\frac{\theta_D}{2T}\right) + 5\int_0^{\theta_D/2T} x^4 \coth x\, dx\right],$$

where $\rho(0)$ is the residual resistivity. In different temperature ranges, the integral in Eq. (2) has different forms. For $T < 80$ K and $\theta_D \sim 400$–500 K, $\theta_D/2T > 3.14$; in this case, the integral $\int_0^{\theta_D/2T}(x^5/\sinh^2 x)dx$ is evaluated as

$$\int_0^{\theta_D/2T} \frac{x^5 dx}{\sinh^2 x} = x^5(1-\coth x)\Big|_0^{\theta_D/2T}$$

$$+ 10\int_0^{\theta_D/2T} x^4[\exp(-2x) + \exp(-4x)$$

$$+ \ldots + \exp(-2nx)]dx.$$

At $T > 80$ K and $\theta_D \sim 400$–500 K, $\theta_D/2T < 3.14$, and the integral $\int_0^{\theta_D/2T} x^4 \coth x dx$ is evaluated as

$$\int_0^{\theta_D/2T} x^4 \coth x dx = \sum_{k=0}^{\infty} 2^{2k} B_{2k} x^{4+2k}/[(4+2k)(2k)!],$$

where B_{2k} are Bernoulli numbers.

The experimental dependences $\rho(T)$ of the $TiO_{1.069}$, $TiO_{0.985}$, $TiO_{0.946}$, and $TiO_{0.920}$ oxides (Fig. 1) are well approximated by function (2) with the θ_D value equal to 480, 400, 470, and 470 K, respectively. According to the data in [4], θ_D varies from 350 to 410 K for equiatomic $TiO_{1.00}$ monoxide and increases with decreasing annealing temperature. In the ordered monoclinic Ti_5O_5 monoxide, $\theta_D = 500$ K [15].

The resistivity of TiO_y monoxides with $y \geq 1.087$ rapidly decreases with rising temperature from 4.2 to 300 K. Although a low resistivity ($\sim 10^{-6}$ Ω m) of all titanium monoxides is typical for metals, the negative temperature coefficient $d\rho/dT$ of the TiO_y monoxides with $y \geq 1.087$ is one of the main attributes of insulators. Due to this effect, the resistivity change $\Delta\rho$ in the range 4.2–300 K is as high as 20–50%, which does not allow $\Delta\rho$ to be treated as a small correction in the relaxation time approximation.

The conductivity σ is proportional to the product of carrier concentration n by carrier mobility u; i.e.,

$$\sigma(T) = en_{e,h}(u_e + u_h). \quad (3)$$

If carriers obey the Boltzmann statistics and the energy bands are parabolic, as is practically always true near the band edges [24], the carrier concentration is

$$n_e = 2(m^*)^{3/2}(k_B T/2\pi\hbar^2)^{3/2}\exp(-\Delta E/2k_B T), \quad (4)$$

where m^* is the effective mass of charge carriers, and ΔE is the energy parameter having a meaning of activation energy and equal to the band gap E_g between the valence and conduction bands in the case of intrinsic conductivity. For the Boltzmann distribution, the mobility of charge carriers is inversely proportional to temperature:

$$u \sim AT^{-p}. \quad (5)$$

Since the residual resistivity of all samples studied is nonzero, the conductivity of TiO_y oxides ($y \geq 1.087$) can be represented, using Eqs. (4) and (5), as

$$\sigma(T) = \sigma(0) + 2(k_B m/2\pi\hbar^2)^{3/2} T^{(3/2-p)}\exp(-\Delta E/2k_B T). \quad (6)$$

The constant $\sigma(0)$ has a meaning of "nonintrinsic" conductivity of the system and indicates that the conductivity is nonzero at $T = 0$.

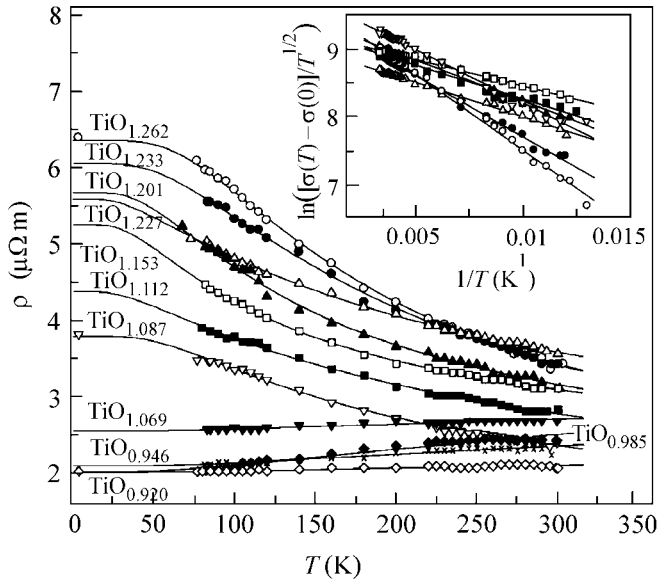

Fig. 1. Temperature dependences of resistivity ρ for disordered cubic titanium monoxides TiO_y with different oxygen content. The approximation of the experimental results by function (2) for TiO_y with $y \leq 1.069$ and by function (7) for TiO_y with $y \geq 1.087$ is shown by solid lines. Inset: temperature dependences of conductivity for $TiO_{1.262}$ – $TiO_{1.087}$ in $\ln\{[\sigma(T) - \sigma(0)]/T^{1/2}\} - 1/T$ coordinates.

Numerical analysis of the experimental dependences $\sigma(T)$ showed that they are well described by function (6) with $p \approx 1$; i.e.,

$$\sigma(T) = \sigma(0) + BT^{1/2}\exp(-\Delta E/2k_B T). \quad (7)$$

The parameter $p = 1$ is typical of many-atomic semiconductors in which the charge carriers are scattered not only by acoustic but also by optical phonons.

After representing the temperature-dependent part of conductivity (7) for TiO_y monoxides ($y \geq 1.087$) in the coordinates $\ln\{[\sigma(T) - \sigma(0)]/T^{1/2}\} - 1/T$ (inset in Fig. 1), one finds that a linear dependence exists over the entire temperature range studied. The activation energy ΔE is low for monoxides from $TiO_{1.087}$ to $TiO_{1.233}$; it is equal to 0.015–0.030 eV, and only $TiO_{1.262}$ has 0.043 eV. If the intrinsic conductivity arises near 300 K and above, one cannot confidently conclude whether the observed ΔE energy is the band gap or it is the activation energy for the impurity level. This question can be clarified through the analysis of magnetic susceptibility.

Measurements of magnetic susceptibility χ showed that one can distinguish two portions in the temperature curves $\chi(T)$ for all TiO_y samples (Figs. 2, 3), where χ changes with temperature in different ways. A decrease in the susceptibility at low temperatures ($T < 150$–200 K) is typical of a paramagnetic component described by the modified Curie law $\chi(T) = \chi(0) + C/(T + \Delta)$ with temperature-independent paramagnetic contribution

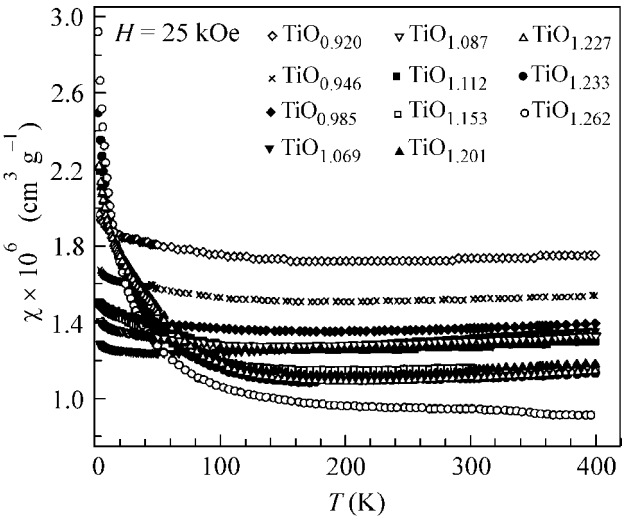

Fig. 2. Magnetic susceptibility χ of disordered cubic titanium monoxides TiO_y with different oxygen content in the temperature range from 4.2 to 400 K (measurements were made in a field H = 25 kOe).

$\chi(0)$ and $\Delta > 0$. At temperatures above 150–200 K, the susceptibility $\chi(T)$ includes, apart from $\chi(0) + C/(T + \Delta)$, a quadratic or more complicated function of temperature.

The Curie paramagnetism of the unit volume of a substance is $\chi_V = Nn\mu_{\text{eff}}^2/3k_BT$, where N is the number of atoms in unit volume, n is the relative concentration of magnetic atoms, $\mu_{\text{eff}} = p\mu_B$ is the effective magnetic moment, and μ_B is the Bohr magneton. Because $N = N_Ad/M$ (N_A is Avogadro's number, d is density, and M is molar weight), the measured magnetic susceptibility of unit weight is $\chi = \chi_V/d = (nN_A/M)(p\mu_B)^2/3k_BT \equiv C/T$, from which $p^2 = (CM/n)(3k_B/N_A\mu_B^2)$ or, after substituting the values of N_A, μ_B, and k_B, $p \approx \sqrt{8CM/n}$, where the Curie-law constant C has $\text{cm}^3\,\text{K}\,\text{g}^{-1}$ dimensionality. If the concentration n of atoms having magnetic moment is unknown, the magnetic moment averaged over all atoms is given by $p_{\text{aver}} \approx \sqrt{8CM}$.

The calculation with the resulting constant C showed that the effective magnetic moment μ_{eff} averaged over all atoms comprises 0.015–0.225 Bohr magnetons. The small value of μ_{eff} implies that the Curie contribution to the susceptibility is most likely of impurity nature. It is probable that electrons of the majority of Ti^{2+} ions in TiO_y are paired or cation–cation exchange interaction takes place. We failed to determine the presence of any ions with uncompensated magnetic moment in TiO_y by the EPR method because of a high concentration of delocalized electrons. Inasmuch as the ferromagnetic impurities are absent in the TiO_y samples, the small effective moment may be due to the impurity Ti^{2+} and Ti^{3+} ions. Judging from the p value, the content of such impurity ions varies from 2 to 8 at. %. The Curie paramagnetism is most pronounced in TiO_y with relatively large oxygen content $y > 1.2$ (Fig. 3).

The $\chi(T)$ dependence for TiO_y with $y \le 1.069$ (Fig. 3) is well approximated by the function $\chi(T) = \chi(0) + C/(T + \Delta) + bT^2$ over the entire temperature range studied. The quadratic term bT^2 is characteristic of the Pauli paramagnetism of conduction electrons. This agrees well with the metallic type of conductivity of these monoxides.

The temperature dependences of the susceptibility of TiO_y monoxides with $y \ge 1.087$ are more complicated, especially in a high-temperature range (Fig. 3). If the concentration of charge carriers in TiO_y with $y \ge 1.087$ is described by Eq. (4) at $T > 300$ K, then the temperature-dependent part of magnetic susceptibility, according to the Curie formula $\chi_p(T) = n_e(\mu_B)^2/k_BT$, has the paramagnetic component

$$\chi_p(T) = 2(m^*/2\pi\hbar^2)^{3/2}(k_B)^{1/2}(\mu_B)^2T^{1/2} \times \exp(-\Delta E/2k_BT) \equiv AT^{1/2}\exp(-\Delta E/2k_BT), \quad (8)$$

where $A = 2(m_0/2\pi\hbar^2)^{3/2}(k_B)^{1/2}(\mu_B)^2q^{3/2} = 3.008 \times 10^{-9}q^{3/2}$ [$\text{K}^{-1/2}$]; $q = m^*/m_0$; and m_0 is the electron mass. Note that Eq. (8) describes the dimensionless susceptibility of unit volume. Taking into account the above-mentioned features of the $\chi(T)$ dependences and introducing $A_m = A/d$, the susceptibility of unit weight measured for TiO_y with $y \ge 1.087$ can be approximated over the entire temperature range studied by the function

$$\chi(T) = \chi(0) + A_mT^{1/2} \times \exp(-\Delta E/2k_BT) + C/(T + \Delta), \quad (9)$$

which includes the temperature-independent contribution $\chi(0)$, the Pauli paramagnetism of electronic system with energy gap, and the Curie paramagnetism.

The coefficients A_m in Eq. (9) are equal to 0.012×10^{-6} and 0.034×10^{-6} $\text{cm}^3\,\text{g}^{-1}\,\text{K}^{-1/2}$ for $TiO_{1.087}$ and $TiO_{1.262}$, respectively, and the densities of $TiO_{1.087}$ and $TiO_{1.262}$ are, respectively, 4.97 and 4.82 g cm^{-3}. The effective mass of charge carriers, expressed in m_0, is $m^* = 4.799 \times 10^5(A_md)^{2/3}m_0$. Hence, the effective masses of carriers in $TiO_{1.087}$ and $TiO_{1.262}$ are $\sim 7m_0$ and $\sim 14m_0$, respectively. The fact that the effective mass is rather large lends support to the validity of using the Boltzmann distribution for the description of carrier concentrations in TiO_y monoxides with $y \ge 1.087$.

The ΔE values found for the $TiO_{1.087}$ and $TiO_{1.262}$ monoxides from temperature dependences $\chi(T)$ (9) are equal to 0.061 and 0.173 eV. The ΔE values derived from the temperature dependences of conductivity for the same monoxides are 0.029 and 0.043 eV. One can

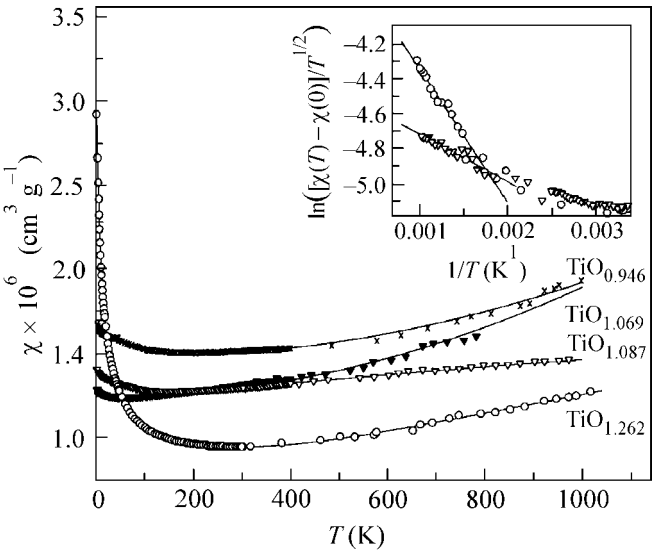

Fig. 3. Magnetic susceptibilities of $TiO_{0.946}$, $TiO_{1.069}$, $TiO_{1.087}$, and $TiO_{1.262}$ in the range from 4.2 K to the temperature of onset of the disorder ⟷ order transition (near 1000 K). The $\chi(T)$ dependences are described by the following functions: $\chi(T) \times 10^6 = 1.410 + 22.9/(T + 88.6) + 4.930 \times 10^{-7}T^2$ for $TiO_{0.946}$; $\chi(T) \times 10^6 = 1.237 + 0.54/(T + 8.5) + 6.591 \times 10^{-7}T^2$ for $TiO_{1.069}$; $\chi(T) \times 10^6 = 1.196 + 0.012T^{1/2}\exp(-353/T) + 14.9/(T + 71.8)$ and $\Delta E = 0.061$ eV for $TiO_{1.087}$; and $\chi(T) \times 10^6 = 0.847 + 0.034T^{1/2}\exp(-1004/T) + 24.1/(T + 7.8)$ and $\Delta E = 0.173$ eV for $TiO_{1.262}$. Inset: high-temperature susceptibility of $TiO_{1.087}$ and $TiO_{1.262}$ in the $\ln\{[\chi(T) - \chi(0)]/T^{1/2}\} - 1/T$ coordinates.

assume that the ΔE values derived from the low-temperature conductivities correspond to the activation energy for impurity levels, whereas the ΔE values derived from the magnetic susceptibility in a broader temperature range define the energy gap for the intrinsic conductivity. The fact that the energy gap is small allows one to consider titanium monoxide TiO_y with $y \geq 1.087$ as a narrow-gap semiconductor.

Thus, the kinetic and magnetic data obtained in this work allow one to assume that a narrow gap between the valence and conduction bands appears in the electronic structure of a disordered cubic titanium monoxide TiO_y upon an increase in the oxygen content. Accordingly, TiO_y can behave as either a *d* metal or a semiconductor depending on the oxygen content.

We are grateful to N.A. Kirsanov, A.V. Korolev, and R. Henes for assistance in the experiment.

REFERENCES

1. A. I. Gusev and A. A. Rempel', *Structural Phase Transitions in Nonstoichiometric Compounds* (Nauka, Moscow, 1988).
2. A. I. Gusev and A. A. Rempel', *Nonstoichiometry, Disorder and Order in Solid* (Ural. Otd. Ross. Akad. Nauk, Yekaterinburg, 2001).
3. A. D. Pearson, J. Phys. Chem. Solids **4**, 316 (1958).
4. S. P. Denker, J. Appl. Phys. **37**, 142 (1966).
5. M. I. Aĭvazov, I. A. Domashnev, A. G. Sarkisyan, and T. V. Rezchikova, Izv. Akad. Nauk SSSR, Neorg. Mater. **6**, 745 (1970).
6. M. D. Banus, T. B. Reed, and A. J. Strauss, Phys. Rev. B **5**, 2775 (1972).
7. M. Schoen and S. P. Denker, Phys. Rev. **184**, 864 (1969).
8. L. F. Mattheis, Phys. Rev. B **5**, 290 (1972).
9. A. Neckel, P. Rastl, R. Eibler, *et al.*, J. Phys. C **9**, 579 (1975).
10. A. Neckel, Int. J. Quantum Chem. **23**, 1317 (1983).
11. L. M. Huisman, A. E. Carlsson, C. D. Gellat, and H. Ehrenreich, Phys. Rev. B **22**, 991 (1980).
12. V. A. Gubanov, A. L. Ivanovsky, G. P. Shvelkin, and D. E. Ellis, J. Phys. Chem. Solids **45**, 719 (1984).
13. A. L. Ivanovsky, V. I. Anisimov, D. L. Novikov, *et al.*, J. Phys. Chem. Solids **49**, 465 (1988).
14. S. R. Barman and D. D. Sarma, Phys. Rev. B **49**, 16141 (1994).
15. C. Leung, M. Weinert, P. B. Allen, and R. M. Wentzcovitch, Phys. Rev. B **54**, 7857 (1996).
16. G. K. Wertheim and D. N. E. Buchanan, Phys. Rev. B **17**, 2780 (1978).
17. S. Gokhale, S. R. Barman, and D. D. Sarma, Phys. Rev. B **52**, 14526 (1995).
18. D. R. Jennison and A. B. Kunz, Phys. Rev. Lett. **39**, 418 (1977).
19. J. K. Burdett and T. Hughbanks, J. Am. Chem. Soc. **106**, 3101 (1984).
20. G. Hobiger, P. Herzig, R. Eibler, *et al.*, J. Phys.: Condens. Matter **2**, 4595 (1990).
21. K. Tsutsumi, O. Aita, and K. Ichikawa, Phys. Rev. B **15**, 4638 (1977).
22. S. Bartkowski, M. Neumann, E. Z. Kurmaev, *et al.*, Phys. Rev. B **56**, 10656 (1997).
23. A. A. Valeeva, A. A. Rempel', and A. I. Gusev, Pis'ma Zh. Éksp. Teor. Fiz. **71**, 675 (2000) [JETP Lett. **71**, 460 (2000)].
24. I. M. Tsidil'kovski, *Zero-gap Semiconductors—New Class of Matters* (Nauka, Moscow, 1986).

Translated by V. Sakun

JETP Letters, Vol. 73, No. 11, 2001, pp. 626–629. Translated from Pis'ma v Zhurnal Éksperimental'noĭ i Teoreticheskoĭ Fiziki, Vol. 73, No. 11, 2001, pp. 708–711.

Low-Temperature Heat Conductivity of ZnSe:Ni Crystals: An Unusually Strong Resonant Change Caused by Phonon Scattering from the Anharmonic Modes Induced by Charged Impurities

V. I. Sokolov* and A. T. Lonchakov

Institute of Metal Physics, Ural Division, Russian Academy of Sciences, ul. S. Kovalevskoĭ 18, Yekaterinburg, 620219 Russia

** e-mail: visokolov@imp.uran.ru*

Received May 8, 2001

An anomalously strong resonancelike change with a sharp minimum at a temperature of 15 ± 1 K was observed for the heat conductivity of ZnSe:Ni crystals for the first time. The heat conductivity of one of the samples decreased by more than 200 times, as compared to its maximal value in pure ZnSe. A new phonon scattering mechanism including the *A* processes is suggested to interpret the unusual temperature dependence of heat conductivity. These are the umklapp processes accompanying the phonon scattering from the anharmonic modes induced by charged nickel impurities. As a result, the efficiency of *A* processes may be very high and comparable at 15 K to the efficiency of the *U* processes in ZnSe at a temperature of approximately 1000 K. © *2001 MAIK "Nauka/Interperiodica".*

PACS numbers: 66.70.+f; 63.20.-e

In recent years, interest has grown in the nonlinear properties of condensed media, including nonlinear lattice vibrations. It was predicted theoretically that the local or resonant modes (breathers) with frequencies depending on the vibrational amplitude may appear in a many-atomic chain with strong quartic anharmonicity (see review [1]). Such vibrations have not been observed experimentally so far. In [2, 3], field exciton–vibrational spectroscopy was used to demonstrate that the light-induced transformation $Ni^{+2}(d^8) \longrightarrow Ni^{+}(d^9)$ of the charge state of nickel impurity can give rise to the dominant and spurious vibrational modes whose interaction in the $Ni^{+}Se_4Zn_{12}$ cluster may be rationalized only in terms of a strong cubic or quartic anharmonicity. In this work, the phonon heat conductivity of ZnSe:Ni samples was studied, because phonon scattering in crystal is highly sensitive to the anharmonicity of lattice vibrations.

The heat conductivity κ was measured in the temperature range 5–80 K by the stationary heat-flow method. The maximal error of measurements at $T <$ 10 K did not exceed 10% and was due to the error of measuring the temperature gradient. The difference in temperatures was measured using two (Au + 0.012%Fe)–Cu thermocouples with a sensitivity of $\approx$10 μV/K. The thermocouple head was brought in contact with the samples using silver paste. The heat conductivity was measured for four ZnSe:Ni samples prepared from a melt under inert gas pressure. Samples 2 and 3 were semi-insulating, and sample 4 was low-ohmic with electronic electrical conductivity, as was evidenced by the negative sign of its thermal emf. Figure 1 shows the temperature dependence of heat conductivity for our samples and the $\kappa(T)$ function for pure ZnSe [4]. One can see that our data for pure sample 1 are close to the results [4] both in $\kappa(T)$ magnitude and in temperature of its maximum. The heat conductivity of Ni-doped ZnSe crystals decreases appreciably at temperatures 5–60 K. For sample 2, it sharply decreases from 6.7 to 2 W/(cm K) starting at a temperature of 10 K, and then smoothly approaches the heat conductivity of a pure sample as T increases. The minimum in the difference $\Delta\kappa$ between the heat conductivities of sample 2 and pure ZnSe [4] is clearly seen in the inset. For samples 3 and 4, κ decreases, respectively, from 1 to 0.15 and from 0.1 to 0.03 W/(cm K) with an increase in T starting at the lowest measured temperatures (5–6 K). The lowest heat conductivity is observed at $T_{min} = (15 \pm 1)$ K. Compared to the maximal heat conductivity $\approx$6.5 W/(cm K) of pure ZnSe, its value for samples 3 and 4 is, respectively, $\approx$40 and more than 200 times smaller. At temperatures $T > T_{min}$, $\kappa(T)$ sharply increases and tends to values that are characteristic of pure ZnSe. So far, the pronounced resonant character of temperature dependence of heat conductivity, with a very steep drop to the left and a distinct increase to the right of T_{min}, has been observed neither in semiconductors nor in insulators. Thus, the temperature dependences of heat conductivity for samples 2–4 show the following common features: the presence of a minimum for κ or the difference $\Delta\kappa$ at temperature T_{min} =

(15 ± 1) K and a steep drop in heat conductivity at $T < T_{min}$ in the range 5–15 K for samples 3 and 4 and at 10–16 K for sample 2. However, the comparison of these dependences is hampered because the heat conductivities of these samples change within the range of κ values differing by an order of magnitude for samples 2, 3 and 3, 4, respectively. For this reason, the $\kappa(T)$ curves for these samples are represented in Fig. 2 as plots of fractional heat conductivity $\kappa(T)/\kappa_{min}$ vs. fractional temperature T/T_{min}. One can see that at $T < T_{min}$ the curves in Fig. 2 differ for samples 2–4 by a factor of two at most. They are described by the common empirical formula

$$\log(\kappa(T)/\kappa_{min}) = B\{\log(T/T_{min})\}^n. \qquad (1)$$

The fact that the fractional heat conductivities of the above three samples are close to each other at $T < T_{min}$ suggests that there is a common phonon scattering mechanism of a new type providing very strong temperature dependence in these samples, stronger than the T^3 dependence caused by the lattice specific heat. It is most convenient to derive the parameters of temperature dependence (1) from the curves at $T < T_{min}$, because the phonon scattering from the sample boundaries is independent of T in this temperature range, while the other known scattering mechanisms are inoperative at $T < T_{min}$. An analysis of the experimental data yields $B \approx 2.5$–3.0 and $n \approx 2$. The heat conductivity of sample 2 decreases at $T > T_{min}$. This is due to the additional phonon scattering via the U processes that represent the most efficient phonon scattering mechanism at high temperatures. The heat conductivities of samples 3 and 4 increase, and, hence, the scattering of a new type is dominant, whereas the phonon scattering through the U processes only depresses this dominant process.

The resonancelike character of phonon scattering in the presence of impurities can be caused by the coincidence of the phonon frequency either with the energy gap between the electronic states of impurity center [4] or with the frequency of impurity-induced lattice mode [5]. The first variant was invoked to interpret the temperature-dependent heat conductivities of CdTe:Fe and ZnS:Fe, in which the electronic states of the Fe^{2+} ion (d^6 configuration) are separated by approximately 2–2.5 meV, so that the scattering of acoustic phonons may induce transitions between these states [4]. For the Ni^{2+} ion (d^8 configuration), the splitting of the ground state $^3T_1$ is almost an order of magnitude larger than the splitting in the Fe^{2+} ion. For this reason, the phonon energy at a temperature of 15 K is too small to induce the electronic transitions in the impurity center, so that this mechanism cannot be responsible for the resonant change in the heat conductivity of the ZnSe:Ni samples. Since the Ni^{2+} ion is lighter than the Zn^{2+} ion, one should not expect the appearance of a low-frequency resonant mode in ZnSe:Ni, as usually occurs when the mass of an impurity atom is greater than the mass of the substituted host atom, e.g., as in KI:Ag [5].

The presence of electronic thermal emf in low-ohmic sample 4 is helpful in the interpretation of our

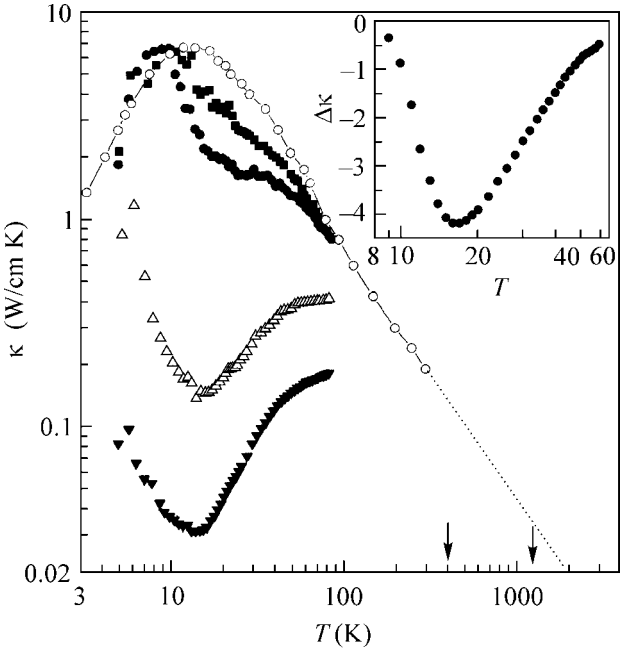

Fig. 1. Temperature dependences of the heat conductivity of zinc selenide crystals. (○) Pure ZnSe [4]; (■) sample 1 (pure ZnSe). ZnSe:Ni samples with Ni concentration: (●) 4.3×10^{17} cm^{-3} (sample 2); (△) 3.6×10^{19} cm^{-3} (sample 3); (▼) 1×10^{20} cm^{-3} (sample 4). Arrows indicate temperatures at which the heat conductivity of pure crystal is approximately equal to the minimal heat conductivity of samples 3 and 4, respectively. Inset: difference in the heat conductivities of sample 2 and pure ZnSe [4].

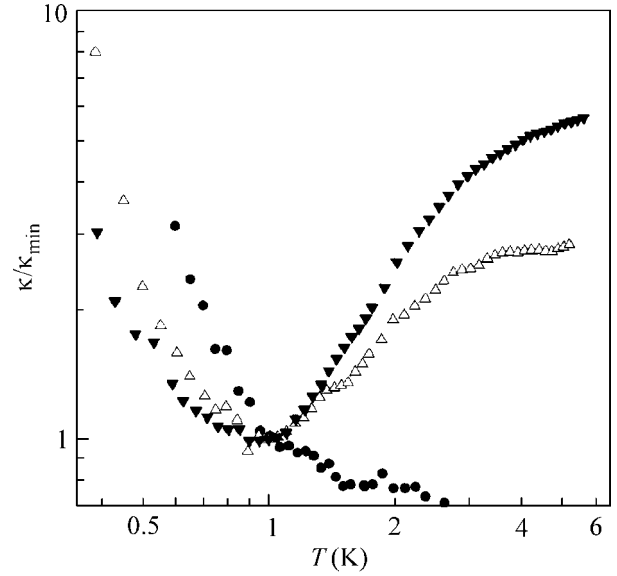

Fig. 2. Fractional heat conductivity κ/κ_{min} as a function of fractional temperature T/T_{min} for samples 2–4 (notation as in Fig. 1).

results. This fact gives evidence for the presence of shallow donors in the sample. The donor electrons transfer to the nickel ions, whose acceptor level (0/–) lies approximately amid the energy gap of ZnSe. This gives rise to the $Ni^+(d^9)$ ions negatively charged relative to the lattice. The excess electron of the negative $Ni^+(d^9)$ ion occupies its 3*d* shell. It was shown for ZnSe:Ni that the Coulomb field of the negative $Ni^+(d^9)$ ion shifts the Se^{2-} and Zn^{2+} ions to new equilibrium positions. The $Ni^+ \longrightarrow Se^{2-}$ and $Ni^+ \longrightarrow Zn^{2+}$ distances change, respectively, by 10 and 1% of their values in a crystal with neutral Ni^{2+} impurity [3, 6]. Note for comparison that the crystal melting upon heating occurs when the bonds are elongated by approximately 3%. This gives grounds to assume that the lattice is heavily distorted upon changing charge of the impurity center and the vibrational modes of a $Ni^+Se_4Zn_{12}$ cluster appear. According to the results of field exciton–vibrational spectroscopic studies, these modes strongly interact with each other due to their high anharmonicity [2, 3].

Taking this into account, we suggest the following qualitative explanation of the experimentally observed strong resonancelike change in the heat conductivity $\kappa(T)$ of the ZnSe:Ni samples. Apart from the nickel impurities, our samples also contain shallow donor-type impurity centers. Because of this, both neutral impurity centers $Ni^{2+}(d^8)$ and negatively charged $Ni^+(d^9)$ centers coexist in the samples. Although the concentration of the $Ni^+(d^9)$ ions was not measured in an independent way, we assume, based on the total concentration of nickel, that the concentration of the $Ni^+(d^9)$ ions is the lowest in sample 2 and the highest in sample 4. The negatively charged $Ni^+(d^9)$ ions distort the lattice and give rise to the resonant anharmonic modes. These modes strongly scatter phonons; we will call this scattering the *A* process in order to emphasize that the high anharmonicity of these vibrational modes is the key element of the mechanism proposed. One can tentatively compare the intensity of the *A* process at a temperature of 15 K with the phonon scattering via the umklapp processes (*U* processes) in pure crystal at high temperatures. The heat conductivity of sample 2 decreases by 4 W/(cm K) with increasing *T* in the range 10–16 K, whereas in pure ZnSe crystal a decrease by ≈4 W/(cm K) occurs in the range of approximately 16–50 K. A sharp change $\Delta\kappa$ in heat conductivity of sample 3 from 1.2 to 0.14 W/(cm K) in the temperature range 6–15 K is equivalent to a change in heat conductivity of pure ZnSe in the temperature range of approximately 100–400 K, and a change $\Delta\kappa$ from 0.1 to 0.03 W/(cm K) for sample 4 corresponds to a change in heat conductivity of ZnSe in the temperature range of approximately 500–1200 K. A high efficiency of the *A* processes at low temperatures (7–15 K) can be understood at a qualitative level as follows. The anharmonic vibrations involve the motion of ions in the first and the second coordination spheres. This crystal region is comparable in size with the unit cell, and, hence, the quasimomentum corresponding to the anharmonic mode is comparable with the reciprocal lattice vector. For this reason, the quasimomentum of a long-wavelength acoustic phonon scattered from this mode may become equal to the reciprocal lattice vector, as occurs with the *U* processes. Hence, the *A* processes are the umklapp processes occurring in the scattering of acoustic phonons from the anharmonic vibrational modes induced by the charged nickel impurities. This renders the *A* processes as efficient at low temperatures as the *U* processes are at high temperatures in pure crystal.

The resonant temperature dependence of *A* processes may be caused by the potential energy of an oscillator as a sum of the third and fourth powers of displacement from equilibrium position:

$$U(x) = U_0 + K_2x^2 + K_3x^3 + K_4x^4. \qquad (2)$$

If the anharmonicity constants K_3 and K_4 are large enough, the potential becomes double-well. At low temperature, the oscillator occurs in the lower minimum and is harmonic. As the temperature increases, the oscillator interacts with phonons and undergoes transition to higher energies where the role of anharmonic term K_4x^4 is appreciable and the frequency depends on the oscillation amplitude. The form of this dependence is unknown for the $Ni^+Se_4Zn_{12}$ cluster modes, but it must satisfy the condition for the formation of the anharmonic resonant mode, much as the anharmonic resonant modes are formed in a linear monatomic chain with "soft" anharmonicity [7]. Because of this, only those phonons can scatter by such an oscillator whose energies fit the amplitude-dependent oscillator frequency. However, only part of these phonons have quasimomenta corresponding to the umklapp processes. If the phonons corresponding to the maximum of phonon distribution meet these two conditions at a given temperature *T*, the dissipation of heat flow will be maximal. At low temperature *T*, the maximum in the frequency distribution of acoustic phonons occurs at the frequency $h\nu \approx 1.6\,kT$. In our case, the phonon flow is minimal at a temperature of 15 K, which corresponds to the frequency of acoustic phonons $\nu \approx 0.5$ THz.

Thus, a strong resonancelike change in the phonon heat conductivity has been observed experimentally for the ZnSe:Ni crystal. To explain this finding, we assume that the mechanism of phonon scattering from the anharmonic modes of the $Ni^+Se_4Zn_{12}$ cluster (*A* process) includes the umklapp processes accompanying the phonon scattering from the impurity anharmonic modes. As a result, the efficiency of *A* processes at a temperature of 15 K is comparable with the efficiency of phonon scattering via the *U* processes at temperatures of 100–1200 K. The fact that the efficiencies of the *A* and *U* processes are almost the same throws more light on the role of high anharmonicity of the vibrational modes of the $Ni^+Se_4Zn_{12}$ cluster than do the

results of field exciton–vibrational spectroscopic studies [2, 3]. The interpretation suggested for the observed anomalously strong phonon scattering from the impurity anharmonic mode is tentative. The new phonon scattering mechanism calls for further experimental study and comprehensive theoretical analysis.

We are grateful to N.B. Gruzdev for assistance in preparing samples and to V.V. Fedorenko for measuring the concentration of Ni impurities in the ZnSe:Ni samples on an X-ray microanalyzer. This work was supported in part by the Russian Foundation for Basic Research, project no. 00-02-16299.

REFERENCES

1. S. Flach and C. R. Willis, Phys. Rep. **295**, 181 (1998).
2. V. I. Sokolov, E. A. Shirokov, A. N. Kislov, and V. G. Mazurenko, Phys. Rev. Status Solid B **221**, 553 (2000).
3. V. I. Sokolov, E. A. Shirokov, A. N. Kislov, and V. G. Mazurenko, J. Cryst. Growth **214/215**, 304 (2000).
4. G. A. Slack, Phys. Rev. B **6**, 3791 (1972).
5. A. Maradudin, Solid State Phys. **18**, 273 (1966); **19**, 1 (1966).
6. A. N. Kislov, V. G. Mazurenko, V. I. Sokolov, and A. N. Varaksin, Fiz. Tverd. Tela (St. Petersburg) **39**, 2147 (1997) [Phys. Solid State **39**, 1921 (1997)].
7. S. Takeno and A. J. Sievers, Solid State Commun. **67**, 1023 (1988).

Translated by V. Sakun

JETP Letters, Vol. 73, No. 11, 2001, pp. 630–632. Translated from Pis'ma v Zhurnal Éksperimental'noĭ i Teoreticheskoĭ Fiziki, Vol. 73, No. 11, 2001, pp. 712–714.

Spin-Reorientation Transition at Isoelectronic Substitution in Double-Layer Manganites $(La_{1-z}Pr_z)_{1.2}Sr_{1.8}Mn_2O_7$

A. Vasil'ev[1], T. Voloshok[1], M. Apostu[2], R. Suryanarayanan[2], and A. Revcolevschi[2]

[1] *Moscow State University, Moscow, 119899 Russia*

[2] *Universite Paris-Sud, 91405 Orsay, France*

Received May 11, 2001

The transport, magnetic, and thermal properties of single crystal double-layer manganites of the Ruddlesden–Popper series $(La_{1-z}Pr_z)_{1.2}Sr_{1.8}Mn_2O_7$ ($z = 0.1$ or 0.4) were studied. The compounds exhibit the colossal negative magnetoresistance effect in the region of a transition into a ferromagnetic state. Upon the isoelectronic substitution of Pr^{3+} for La^{3+}, the Curie temperature decreases, while the easy magnetization axis rotates from the *ab* plane to the *c* axis. The observed effect is related to a change in the occupancy of $d_{x^2-y^2}$ and $d_{3z^2-r^2}$ orbitals as a result of stretching of the MnO_6 octahedra. © *2001 MAIK "Nauka/Interperiodica".*

PACS numbers: 75.30.Vn; 75.40.Cx

In the Ruddlesden–Popper series of metal oxide compounds [1] with the general formula $[(RE,AE)MnO_3]_n(RE,AE)O$ (where RE stands for rare-earth ions and AE, for alkaline-earth ions), the effect of colossal negative magnetoresistance was studied for the most part in three-dimensional perovskites of the $(RE,AE)MnO_3$ type ($n = \infty$) [2, 3]. The discovery of the colossal negative magnetoresistance in $[La_xSr_{1-x}MnO_3]_2(La_xSr_{1-x}O)$ with $x = 0.4$ [4] has drawn the attention of researchers to the Ruddlesden–Popper compounds with $n = 2$.

In the crystal structure of these compounds, the double perovskite layers $[(La,Sr)MnO_3]_2$ in the *ab* plane are separated by the (La,Sr)O layers in the *c* direction. The ratio of the rare-earth (La^{3+}) and alkaline-earth (Sr^{2+}) ions determines the content of trivalent (Mn^{3+}) and tetravalent (Mn^{4+}) manganese ions. With decreasing temperature, $[La_xSr_{1-x}MnO_3]_2(La_xSr_{1-x}O)$ compounds exhibit magnetic ordering the type of which depends on the *x* value [5]. In the same layer of MnO_6 octahedra, the interaction is always ferromagnetic, but the ordering of layers within one bilayer may vary including antiferromagnetic, canted antiferromagnetic, and ferromagnetic types.

The compound $La_{1.2}Sr_{1.8}Mn_2O_7$ (corresponding to $x = 0.4$) exhibits the transition into a ferromagnetic state of the easy plane type at $T_C \sim 120$ K [6]. The low (in comparison with the three-dimensional perovskites) value of the Curie temperature in the two-layer manganites is due to a lower dimensionality of the magnetic subsystem. The colossal negative magnetoresistance observed in the vicinity of T_C is characterized by a considerable anisotropy: the electron transport is effective in the *ab* plane and is hindered along the *c* axis.

At a fixed ratio of the La^{3+} and Sr^{2+} ions, a significant effect on the transport and magnetic properties of layered manganites is produced by isoelectronic substitutions at the positions of both RE and AE ions. This is explained by a difference in atomic radii of the corresponding ions that leads to a change in the (La,Sr)O layer thickness and to distortion of the manganese–oxygen octahedra. For example, the compound $La_{1.2}(Sr_{1-y}Ca_y)_{1.8}Mn_2O_7$ exhibits a change in the ordering type from ferromagnetic to antiferromagnetic when Ca^{2+} ions (with an atomic radius of 1.06 Å) are substituted for Sr^{2+} (1.27 Å), so that the *y* value increases [7].

The aim of our experiments was to study the effect of isoelectron substitution at the rare-earth ion position on the properties of $(La_{1-z}Pr_z)_{1.2}Sr_{1.8}Mn_2O_7$. For this purpose, the La^{3+} ions (with an atomic radius of 1.22 Å) were replaced by Pr^{3+} (1.06 Å). It was established that this substitution significantly affects the transport, magnetic, and thermal properties of $(La_{1-z}Pr_z)_{1.2}Sr_{1.8}Mn_2O_7$ single crystals. The single crystals with $z = 0.1$ and 0.4 were grown by the floating zone technique. These crystals possess a body-centered tetragonal structure belonging to the space symmetry group *I*4/*mmm*. The electric resistance was measured by a standard four-point-probe method, and the magnetic properties were studied using a SQUID magnetometer, and the specific

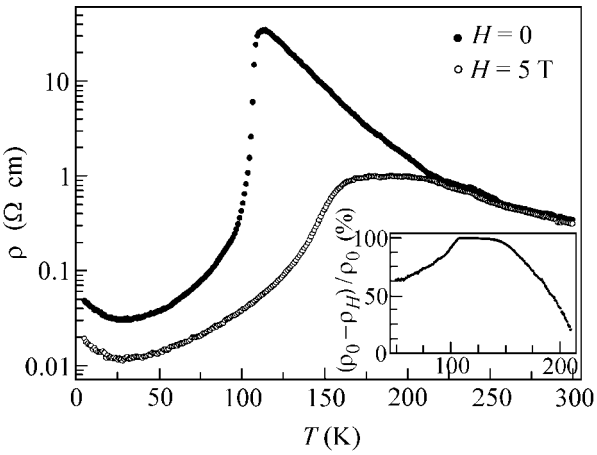

Fig. 1. The temperature dependence of the electric resistance ρ of a $(La_{1-z}Pr_z)_{1.2}Sr_{1.8}Mn_2O_7$ single crystal with $z = 0.1$ measured in the *ab* plane with and without an applied magnetic field *H*. The inset shows the temperature variation of the negative magnetoresistance $(\rho_0 - \rho_H)/\rho_0$.

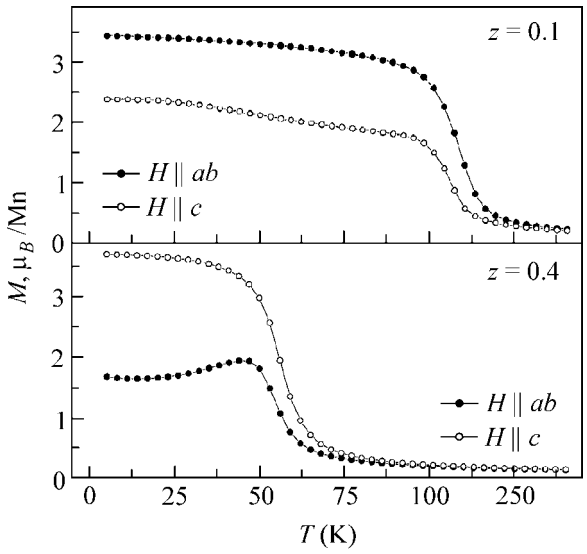

Fig. 2. The temperature dependence of the magnetization *M* of the $(La_{1-z}Pr_z)_{1.2}Sr_{1.8}Mn_2O_7$ single crystals with $z = 0.1$ and 0.4 measured with the magnetic field ($H = 0.5$ T) applied in the *ab* plane and along the *c* axis.

heat was measured with a quasiadiabatic microcalorimeter. All these physical characteristics were measured in the temperature range from 4 to 300 K.

Figure 1 shows the temperature dependence of the resistance ρ of a $(La_{0.9}Pr_{0.1})_{1.2}Sr_{1.8}Mn_2O_7$ single crystal ($z = 0.1$) measured in the *a* direction without an applied magnetic field and in a field of 5 T. In the absence of the magnetic field, the initial semiconductor-like variation of the resistance changes for a decrease at $T_C = 107$ K. Some increase in the sample resistance at low temperatures ($T < 25$ K) can be related to the scattering on magnetic impurities. When the magnetic field is applied, a

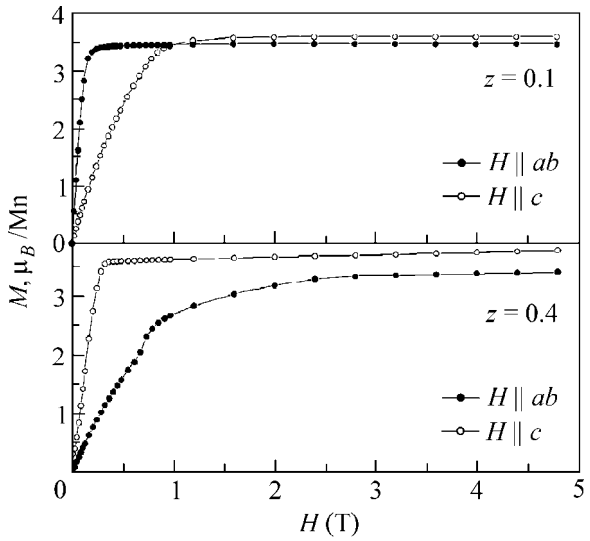

Fig. 3. The field dependence of the magnetization *M* of the $(La_{1-z}Pr_z)_{1.2}Sr_{1.8}Mn_2O_7$ single crystals with $z = 0.1$ and 0.4 measured at $T = 5$ K with the magnetic field ($H = 0.5$ T) applied in the *ab* plane and along the *c* axis.

maximum in the temperature dependence of the sample resistance shifts toward higher temperatures, the negative magnetoresistance $(\rho_0 - \rho_H)/\rho_0$ in the phase transition region reaching almost 100%.

Figure 2 shows the temperature dependence of the magnetization *M* of the $(La_{0.9}Pr_{0.1})_{1.2}Sr_{1.8}Mn_2O_7$ ($z = 0.1$) and $(La_{0.6}Pr_{0.4})_{1.2}Sr_{1.8}Mn_2O_7$ ($z = 0.4$) single crystals measured for a magnetic field of 0.5 T applied in the *ab* plane and along the *c* axis. A sharp increase in the magnetization, typical of the transition into a ferromagnetic state, is observed on decreasing the temperature to $T \sim 107$ K ($z = 0.1$) and $T \sim 65$ K ($z = 0.4$). Note that, in the sample with $z = 0.1$, the magnetization along the *a* axis exceeds that in the *c* direction, whereas a reverse situation is observed in the sample with $z = 0.4$.

The experimental curves of $M(T)$ are consistent with the field dependence of magnetization measured at $T = 5$ K (Fig. 3). As is seen, the sample with $z = 0.1$ occurs in a ferromagnetic state of the easy plane type, while the sample with $z = 0.4$ exhibits the easy axis state. The saturation of magnetization in both cases is attained at a field strength of about 1 T, whereby the magnetization reaches a level of $\sim 3.6\mu_B$.

Figure 4 shows the plots of the specific heat versus temperature for the $(La_{0.9}Pr_{0.1})_{1.2}Sr_{1.8}Mn_2O_7$ and $(La_{0.6}Pr_{0.4})_{1.2}Sr_{1.8}Mn_2O_7$ single crystals, which confirm the presence of a phase transition at $T_C = 107$ K ($z = 0.1$) and $T_C = 65$ K ($z = 0.4$). At low temperatures, the specific heat of the samples studied contains linear and cubic components with respect to the temperature: $C = \gamma T + \beta T^3$. A linear contribution to the specific heat can be related both to the conduction electrons and the ferromagnetic magnons in the two-dimensional magnetic

Characteristics of $(La_{1-z}Pr_z)_{1.2}Sr_{1.8}Mn_2O_7$ manganites with $z = 0.1$ and 0.4

	T_C, K	γ, mJ/(mol K^2)	β, mJ/(mol K^2)	Θ, K	ΔS_{magn}, mJ/(mol K^2)
$(La_{0.9}Pr_{0.1})_{1.2}Sr_{1.8}Mn_2O_7$	107	50	0.344	409	1
$(La_{0.6}Pr_{0.4})_{1.2}Sr_{1.8}Mn_2O_7$	65	56	0.449	385	0.9

subsystem of $(La_{1-z}Pr_z)_{1.2}Sr_{1.8}Mn_2O_7$ [8], while the cubic term is due to phonons. The γ and β coefficients for the samples with $z = 0.1$ and 0.4 are given in the table. The table also presents the values of the Debye temperature Θ_D determined using the relationship $\beta = 12\pi^4 R\nu/5\Theta_D^3$, where R is the universal gas constant and $\nu = 12$ is the number of atoms per formula unit. In a broad range of temperature, except the phase transition region, the phonon contribution to the heat capacity is described by three Einstein modes. This circumstance allows a part of the entropy ΔS_{magn} related to the magnetic system ordering to be separated. The corresponding values are also indicated in the table.

The experimental data presented above indicate that an increase in the Pr content is accompanied by a decrease in the temperature of ferromagnetic ordering, while the magnetization vector exhibits reorientation from the *ab* plane to the *c* axis. This behavior is related to the fact that the isoelectronic substitution of Pr^{3+} for La^{3+} decreases the (La–Pr,Sr)O layer thickness and increases the distance from Mn^{3+}/Mn^{4+} ions to the apical O^{2-} ions. Stretching of the MnO_6 octahedra in the *c* direction leads to a change in the order of the partly filled e_g orbitals. In $La_{1.2}Sr_{1.8}Mn_2O_7$, the $3d_{x^2-y^2}$ orbital lies below the $3d_{3z^2-r^2}$ orbital [5]; apparently, the same situation takes place in $(La_{0.9}Pr_{0.1})_{1.2}Sr_{1.8}Mn_2O_7$. Predominant filling of the $3d_{x^2-y^2}$ orbital favors the electron transport in the *ab* plane and accounts for a rather high temperature of the ferromagnetic ordering due to the exchange involving the conduction electrons. For $z = 0.4$, the stretching of the MnO_6 octahedra in the *c* direction favors predominant filling of the $3d_{3z^2-r^2}$ orbital. In this case, the electron transport in the *ab* plane is hindered. This, together with the absence of electron transport along the *c* axis, leads to a decrease in contribution of the conduction electrons to the exchange and, hence, to the corresponding decrease in the temperature of ferromagnetic ordering.

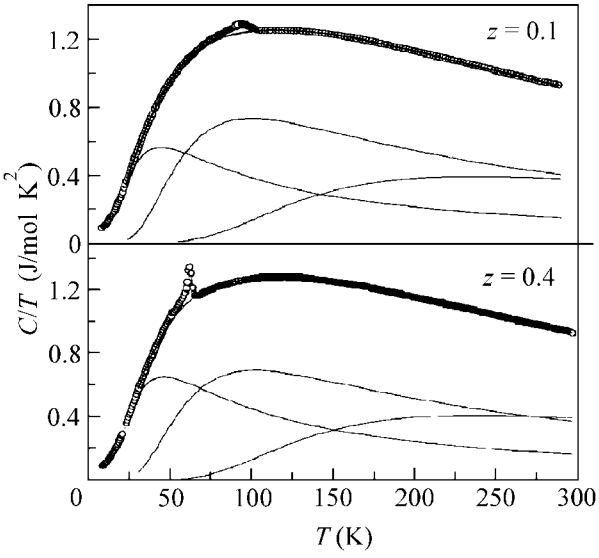

Fig. 4. The temperature dependence of the specific heat of the $(La_{1-z}Pr_z)_{1.2}Sr_{1.8}Mn_2O_7$ single crystals with $z = 0.1$ and 0.4. Thin solid curves show the three Einstein modes approximating the phonon contribution.

The authors are grateful to D.I. Khomskiĭ for fruitful discussions. This study was supported by the Russian Foundation for Basic Research (project no. 99-02-17828), INTAS (grant no. 99-0155), and NWO (grant no. 047-008-012).

REFERENCES

1. S. N. Ruddlesden and P. Popper, Acta Crystallogr. **11**, 54 (1958).
2. D. I. Khomskii and G. A. Sawadzky, Solid State Commun. **102**, 87 (1997).
3. *Colossal Magnetoresistance, Charge Ordering and Related Properties in Manganese Oxides*, Ed. by C. N. R. Rao and B. Raveau (World Scientific, Singapore, 1998).
4. Y. Moritomo, A. Asamitsu, H. Kuwahara, and Y. Tokura, Nature **380**, 141 (1996).
5. T. Kimura, Y. Tomioka, A. Asamitsu, and Y. Tokura, Phys. Rev. Lett. **81**, 5920 (1998).
6. H. Ogasawara, M. Matsukawa, S. Hatakeyama, *et al.*, J. Phys. Soc. Jpn. **69**, 1274 (2000).
7. T. Akimoto, Y. Moritomo, K. Ohoyama, *et al.*, Phys. Rev. B **59**, 14153 (1999).
8. B. Bernua and G. Misguich, Phys. Rev. B **63**, 134409 (2001).

Translated by P. Pozdeev

JETP Letters, Vol. 73, No. 11, 2001, pp. 633–636. Translated from Pis'ma v Zhurnal Éksperimental'noĭ i Teoreticheskoĭ Fiziki, Vol. 73, No. 11, 2001, pp. 715–718.

Thermal Conductivity and Specific Heat of $SrCu_2(BO_3)_2$: A Quasi-Two-Dimensional Metal Oxide Compound with a Spin Gap

A. N. Vasil'ev[1,*], M. M. Markina[1], A. V. Inyushkin[2], and H. Kageyama[3]

[1] *Moscow State University, Moscow, 119899 Russia*

* *e-mail: vasil@lt.phys.msu.su*

[2] *Institute of Molecular Physics, Russian Research Centre Kurchatov Institute, Moscow, 123182 Russia*

[3] *Institute for Solid State Physics, University of Tokyo, Kashiwa, Chiba, 277-8581 Japan*

Received May 11, 2001

The thermal conductivity and specific heat of $SrCu_2(BO_3)_2$, a quasi-two-dimensional metal oxide compound with a spin gap, were studied at low temperatures. In the temperature interval $0.4 < T < 3.2$ K, the thermal conductivity of a single crystal sample in the *ab* plane varies according to the power law $\kappa \propto T^{2.73}$. As the temperature increases further, a deep minimum is observed in the region of $T_{min} \approx 9.8$ K. This behavior is explained by the scattering of phonons—the major heat carriers—on the fluctuations of the spin subsystem. © *2001 MAIK "Nauka/Interperiodica".*

PACS numbers: 66.70.+f; 65.80.+n; 75.40.Cx

In the past decade, a number of low-dimensional quantum-mechanical systems were discovered which, when cooled down to low temperatures, exhibit the appearance of a spin gap separating the nonmagnetic ground state from the spectrum of spin excitations. The formation of a spin gap in such concentrated magnetic systems is manifested by their unusual low-temperature magnetic properties, whereby the samples behave as nonmagnetic substances rather than exhibiting ferro- or antiferromagnetic ordering. The ground state of these compounds is a spin singlet representing an isolated configuration of spins in which the projection of their total magnetic moment onto any direction is zero. Whether a given system reaches a ground state with or without the spin gap depends on the mutual arrangement and magnitude of the spin magnetic moments, as well as on the magnitudes and hierarchy of the exchange interaction constants.

Recently, the group of substances with a spin gap, containing compounds such as spin-Peierls $CuGeO_3$ [1], spin ladder $SrCu_2O_3$ [2], plaquette-type system CaV_4O_9 [3], and charge-ordered system NaV_2O_5 [4], expanded to include a low-dimensional magnetic compound $SrCu_2(BO_3)_2$ [5]. The new member is close to high-temperature superconductors of the cuprate group: $SrCu_2(BO_3)_2$ possesses a layer structure, exhibits a pseudo-spin-gap behavior, and shows the ability to antiferromagnetic ordering upon a small change in the parameters.

$SrCu_2(BO_3)_2$ has a tetragonal unit cell with the room-temperature lattice constants $a = b = 8.995$ Å, $c = 6.649$ Å. The structure of this compound comprises slightly corrugated *ab* planes formed by $CuBO_3$, which are separated by layers of nonmagnetic Sr^{2+} ions along the *c* axis. As is seen in Fig. 1, the *ab* plane contains rectangular planar CuO_4 complexes linked by triangular BO_3 groups. All Cu^{2+} ions possess the spin 1/2 and occupy crystallographically equivalent positions. The nearest-neighbor Cu^{2+} ions form magnetic dimers, while triangular BO_3 complexes link these dimers so as to form an orthogonal network.

At present, $SrCu_2(BO_3)_2$ is the only known substance to which the quantum-mechanical Shastry–Sutherland model [6] can be applied. This theory allows the ground state of an orthogonal dimer network to be exactly calculated. Depending on the ratio of exchange integrals in (J) and between (J') dimers, a system occurs either in the antiferromagnetic ground state (for $J'/J > 0.70$) or in the state with localized magnetic dimers (for $J'/J < 0.70$). At $J'/J = 0.70$, the ground state of an orthogonal dimer network is the spin fluid. According to [7], the exchange integrals in $SrCu_2(BO_3)_2$ are $J' = 68$ K and $J = 100$ K, which corre-

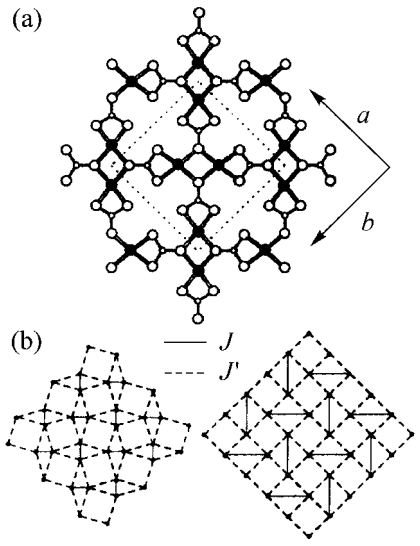

Fig. 1. Schematic diagrams showing the (a) crystal and (b) magnetic structures of $SrCu_2(BO_3)_2$ in the *ab* plane: (●) Cu^{2+} ions; (○) B^{3+} ions; (○) O^{2-} ions.

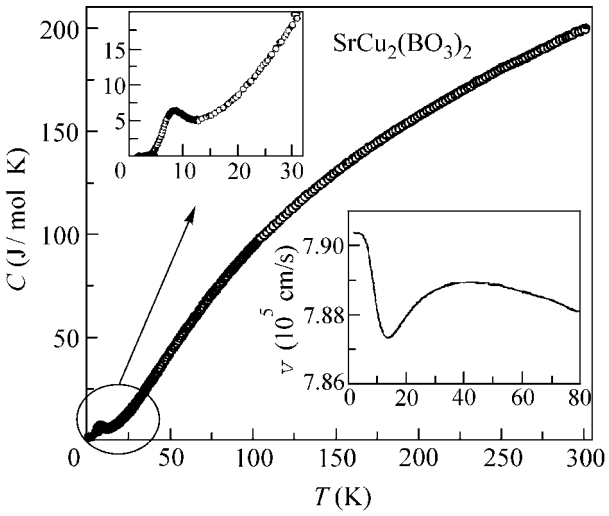

Fig. 2. The temperature dependence of specific heat in $SrCu_2(BO_3)_2$. The bottom inset shows the temperature dependence of the longitudinal sound velocity in the [100] direction (data from [13]).

sponds to the case of localized dimers in the ground state at an exchange integral ratio $J'/J = 0.68$ close to the critical value. The spin gap width $\hbar\omega_0/k_B$ in $SrCu_2(BO_3)_2$ amounts to 34 K [5, 7–9].

A sample of $SrCu_2(BO_3)_2$ studied in our experiments was cut to size $6 \times 1.6 \times 0.4$ mm from a single crystal ingot grown by the floating zone technique [10]. The thermal conductivity $\kappa(T)$ of the single crystal sample was studied in a broad range of temperatures from 0.4 to 300 K by the method of stationary thermal flux in the [100] direction (in the *ab* plane). The specific heat $C(T)$ of pressed powder samples was studied in the range from 1.6 to 300 K with the aid of a quasi-adiabatic microcalorimeter. The errors of determination of the κ and C values at low temperatures were about 10%.

Figure 2 shows the temperature dependence of the specific heat of $SrCu_2(BO_3)_2$. Against a monotonic buildup of the specific heat with increasing temperature, the curve exhibits a clearly pronounced maximum at $T \approx 8.3$ K related to the formation of a spin excitation spectrum [11, 12]. The inset in Fig. 2 shows a temperature dependence of the longitudinal sound velocity v in the [100] direction (reproduced from [13]). As is seen, there is a minimum at $T \approx 13.3$ K on the background of $v(T)$ decreasing with the increase in the sample temperature.

Figure 3 shows the temperature variation of the thermal conductivity of $SrCu_2(BO_3)_2$. At the lowest temperatures, the curve obeys the power law $\kappa(T) \propto T^{2.73}$; as the temperature grows, the κ value passes through a maximum at $T \approx 3.7$ K, then drops to show a minimum at $T \approx 9.8$ K, and increases again with a maximum at $T \approx 47$ K. A maximum value of the thermal conductivity of $SrCu_2(BO_3)_2$ at $T \approx 3.7$ K amounts to $\kappa = 28$ W/(m K). A difference in the temperatures at which the features were observed in the curves of $\kappa(T)$, $C(T)$, and $v(T)$ can be related to the fact that the ground state in $SrCu_2(BO_3)_2$ is attained without a clearly pronounced phase transition at a certain temperature.

The involved temperature variation of the thermal conductivity exhibiting the alternation of maxima and minima is probably a general characteristic of the systems with spin gaps. The $\kappa(T)$ curves with two peaks were previously reported for many low-dimensional compounds, although different interpretations were given in various particular cases. In $CuGeO_3$, the high-temperature peak in the thermal conductivity was explained by the magnon mechanism, and the low-temperature peak, by the phonon mechanism of the heat transfer [14]. The double peak observed in the thermal conductivity of $Sr_{14-x}Ca_xCu_{24}O_{41}$ was interpreted in terms of the magnon propagation over spin chains and ladders [15]. In NaV_2O_5, both peaks in $\kappa(T)$ were attributed to the phonon heat transfer [16].

In our opinion, a more justified interpretation of the $\kappa(T)$ behavior in the case of $SrCu_2(BO_3)_2$ is based on the phonon heat transfer mechanism. According to the neutron scattering data [9], the spin excitations hardly spread over the lattice and, hence, cannot participate in the heat transfer. The minimum of $\kappa(T)$ at $T_{min} \approx 9.8$ K is probably indicative of a strong phonon coupling to the spin subsystem.

We have analyzed the temperature variation of the thermal conductivity within the framework of a simple

Debye lattice thermal conductivity model [17], in which

$$\kappa(T) = \frac{k_B}{2\pi^2 v_s}\left(\frac{k_B}{\hbar}\right)^3 T^3 \int_0^{T_D/T} \frac{x^4 e^x \tau(x,T)}{(e^x-1)^2} dx.$$

Here, $x = \hbar\omega/k_BT$, ω is the phonon frequency, $\tau^{-1} = \sum_i \tau_i^{-1}$ is the total phonon relaxation rate in various scattering processes, $T_D \approx 450$ K is the Debye temperature [13], and v_s is the polarization-averaged sound velocity ($v_s \approx 4.5 \times 10^5$ cm/s [13]).

A satisfactory description of the low-temperature thermal conductivity is obtained with an allowance for the phonon scattering at the sample boundaries ($\tau_b^{-1} = v_s/l_C$), dislocations ($\tau_d^{-1} = A_d\omega$), and point defects ($\tau_{pd}^{-1} = A_{pd}\omega^4$) in the three-phonon processes ($\tau_{3ph}^{-1} = A_{3ph}\omega^2T^3$) and on the spin subsystem fluctuations ($\tau_{\text{flu}}^{-1} = A_{\text{flu}}\omega^4T^2C_s$) [18, 19]. The Casimir length $l_C = 1.12S^{1/2}$ (S is the sample cross section area) determined from the sample geometry was 0.84 mm. In the above relaxation terms, A_i are the fitting parameters and C_s is the heat capacity of the spin subsystem determined by subtracting the phonon contribution from the experimental profile (see the inset in Fig. 3).

The parameters of scattering on dislocations and point defects were determined from a power-law approximation of the low-temperature ($0.4 < T < 3.2$ K) branch of the thermal conductivity, where $\kappa \propto T^{2.73}$. Deviation of the $\kappa(T)$ value from the cubic law expected in the boundary scattering regime can be related to a significant phonon scattering on dislocations. Since the thermal conductivity at high temperatures is determined by the phonon scattering on the spin density fluctuations, which hinders reliable estimation of the parameters of the three-phonon scattering process, our selection for A_{3ph} is rather arbitrary.

The solid curve in Fig. 3 shows the approximation of the temperature dependence of the thermal conductivity in $SrCu_2(BO_3)_2$ calculated with an allowance of all the aforementioned scattering processes. The dashed curve represents the $\kappa(T)$ variation determined with neglect of the phonon scattering on the spin subsystem fluctuations. As is seen, the phonon scattering on the spin density fluctuations decreases the thermal conductivity by almost two orders of magnitude at a temperature in the region of the minimum in the $\kappa(T)$ curve. Such a large depression of the phonon thermal conductivity probably indicates that the entire spectrum of thermal phonons is involved in interaction with the spin subsystem. This conclusion is confirmed by the results of ultrasonic measurements showing that the low-frequency acoustic phonons actually participate in the interaction [13].

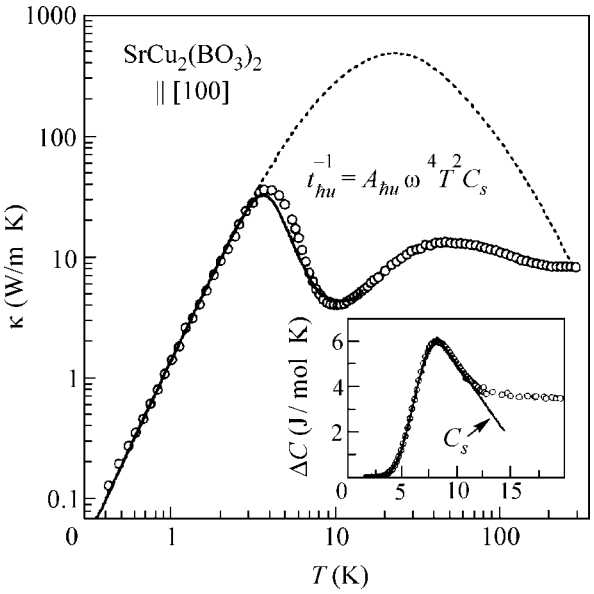

Fig. 3. The temperature dependence of the specific heat of a $SrCu_2(BO_3)_2$ single crystal in the [100] direction. Open circles represent the experimental data, solid curve shows the results of calculations with an allowance of the phonon scattering on the spin subsystem fluctuations, and dashed curve corresponds to the calculation ignoring the spin–phonon interaction. The inset illustrates determination of the heat capacity C_s of the spin subsystem (see the text).

Recently, the minimum observed in the temperature dependence of the thermal conductivity in $SrCu_2(BO_3)_2$ was given an alternative interpretation based on the resonance scattering of phonons in a two-level system of magnetic excitations [12]. In our opinion, this explanation should be taken with care since the resonance scattering can be effective only within a certain narrow part of the phonon spectrum.

The authors are grateful to S. Zherlitsin for kindly providing the results of ultrasonic measurements. This study was supported by the Russian Foundation for Basic Research (project nos. 02-99-17828 and 00-02-16255), INTAS (grant no. 99-0155), and NWO (grant no. 047-008-012).

REFERENCES

1. M. Hase, I. Terasaki, and K. Uchinokura, Phys. Rev. Lett. **70**, 3651 (1993).
2. M. Azuma, Z. Hiroi, M. Takano, *et al.*, Phys. Rev. Lett. **73**, 3463 (1994).
3. S. Taniguchi, T. Nishikawa, Y. Yasui, *et al.*, J. Phys. Soc. Jpn. **64**, 2758 (1995).
4. M. Isobe and Y. Ueda, J. Phys. Soc. Jpn. **65**, 1178 (1996).
5. H. Kageyama, K. Yoshimura, R. Stern, *et al.*, Phys. Rev. Lett. **82**, 3168 (1999).

6. B. S. Shastry and B. Sutherland, Physica B (Amsterdam) **108**, 1069 (1981).
7. S. Miyahara and K. Ueda, Phys. Rev. Lett. **82**, 3701 (1999).
8. H. Kageyama, J. Phys. Soc. Jpn. **68**, 1821 (1999).
9. H. Kageyama, M. Nishi, N. Aso, *et al.*, Phys. Rev. Lett. **84**, 5876 (2000).
10. H. Kageyama, K. Onizuka, Y. Ueda, *et al.*, J. Cryst. Growth **206**, 65 (1999).
11. H. Kageyama, K. Onizuka, Y. Ueda, *et al.*, Zh. Éksp. Teor. Fiz. **117**, 145 (2000) [JETP **90**, 129 (2000)].
12. M. Hofmann, H. Kierspel, T. Lorenz, *et al.*, cond-mat/0103012 (2001).
13. S. Zherlitsyn, S. Schmidt, B. Wolf, *et al.*, Phys. Rev. B **62**, R6097 (2000).
14. Y. Ando, J. Takeya, D. L. Sisson, *et al.*, Phys. Rev. B **58**, R2913 (1998).
15. A. V. Sologubenko, K. Gianno, H. R. Ott, *et al.*, Phys. Rev. Lett. **84**, 2714 (2000).
16. A. N. Vasil'ev, V. V. Pryadun, D. I. Khomskii, *et al.*, Phys. Rev. Lett. **81**, 1949 (1998).
17. R. Berman, *Thermal Conduction in Solids* (Clarendon Press, Oxford, 1976; Mir, Moscow, 1979).
18. K. Kawasaki, Prog. Theor. Phys. **29**, 801 (1963).
19. H. Stern, J. Phys. Chem. Solids **26**, 153 (1965).

Translated by P. Pozdeev